Advanced Techniques for Squeezed-Light-Enhanced Gravitational-Wave Detection

Von der Fakultät für Mathematik und Physik
der Gottfried Wilhelm Leibniz Universität Hannover

zur Erlangung des Grades

Doktor der Naturwissenschaften
– Dr. rer. nat. –

genehmigte Dissertation
von

M.Sc. Jan Gniesmer

2019

Referentinnen und Referenten

Referent:	Prof. Dr. Michael Oestreich
Korreferent:	Prof. Dr. Roman Schnabel
Korreferentin:	Prof. Dr. Michèle Heurs

Prüfungskommission

Vorsitz:	Prof. Dr. Uwe Morgner
Prüfer:	Prof. Dr. Michael Oestreich
Prüfer:	Prof. Dr. Roman Schnabel

Tag der Disputation: 10.05.2019

Abstract

Quantum noise is one of the limiting factors in laser-interferometric gravitational-wave (GW) detectors. The application of squeezed states in these interferometers allows the reduction of quantum noise in one quadrature. Due to opto-mechanical coupling in a GW detector the squeezed quadrature needs to be rotated within the spectrum to achieve a broadband noise reduction. So far, the implementation of additional filter cavities is considered that allow for the optimal, frequency-dependent rotation of the squeezed quadrature. However, these cavities need to have low loss, a length in the order of 100 m and must be situated in the vacuum system, making them cost-intensive.

In 2017, Ma and coworkers proposed a scheme for the broadband quantum-noise reduction without the need of additional filter cavities. It was shown by Brown et al. that a similar scheme can be used to broadband-enhance interferometers with a detuned signal-recycling cavity.

Here, we performed a proof-of-principle experiment of the proposal on a table-top-scale. Squeezed states were produced detuned to the carrier field of a 2.5 m-linear cavity and read out in a bichromatic homodyne detection. The frequencies of the lower and upper local oscillator were at entangled sidebands of the squeezed field. Depending on the relations between the involved frequencies, we can address both variants of the proposal. We show, that the frequency-dependences of the resulting noise spectra fit to a theoretical model we derived from the theory used by Ma et al. With this work we set the path towards an implementation of these schemes in a GW-detector prototype, where the compatibility of the approach with a low-frequency suspended interferometer can be tested.

Moreover, we used the same setup to show nonclassical interferometer enhancement at low frequencies by high-frequency squeezed states. Here, a heterodyne readout scheme was implemented to avoid limiting noises at low frequencies. The application of squeezed states centered around the local oscillator frequency yielded an improvement in signal-to-noise ratio of $3.4\,\mathrm{dB} \pm 0.3\,\mathrm{dB}$.

Additionally, I designed, built and characterized a compact source of squeezed vacuum-states at 1064 nm with a footprint of just $0.8\,\mathrm{m}^2$. I show measurements of squeezed states from this source with a reduction of quantum noise of $10.7\,\mathrm{dB} \pm 0.2\,\mathrm{dB}$ below the vacuum noise and present a noise reduction in the frequency range from 70 kHz to 65 MHz.

Keywords: Gravitational-wave detection, frequency-dependent squeezed light, entanglement, bichromatic homodyne detection

Kurzfassung

Quantenrauschen ist einer der limitierenden Faktoren laserinterferometrischer Gravitationswellen(GW)-Detektion. Die Anwendung von gequetschtem Licht erlaubt die Reduktion von Quantenrauschen. Durch optomechanische Kopplung in GW-Detektoren muss die gequetschte Quadratur frequenzabhängig rotiert werden, um eine breitbandige Rauschreduktion zu erhalten. Bisher wurde der Einsatz zusätzlicher Filterresonatoren erwogen, die eine optimale Rotation der gequetschten Quadratur erlauben. Jedoch müssen diese wenig Verlust, eine Länge von etwa 100 m haben und im Vakuumsystem sein, was sie kostenintensiv macht.

2017 haben Ma et al. ein Schema für eine breitbandige Quantenrausch-Reduktion ohne zusätzliche Filterresonatoren vorgeschlagen. Brown et al. haben gezeigt, dass ein ähnliches Schema für eine breitbandige Verbesserung von verstimmten Signal-recycleten Interferometern benutzt werden kann.

Wir haben zum Beweis der Idee ein Experiment auf Labortisch-Größe durchgeführt. Gequetschte Zustände wurden verstimmt zum Trägerfeld eines 2.5 m linearen Resonators erzeugt und in einer zweifarbigen Homodyndetektion ausgelesen. Die Frequenzen der beiden Lokaloszillatoren stimmten mit verschränkten Seitenbändern des gequetschten Feldes überein. Abhängig von der Relation der beteiligten Frequenzen können wir beide Vorschläge adressieren. Wir zeigen, dass die Frequenzabhängigkeiten der Rauschspektren zu einem theoretischen Modell passen, dass wir auf Basis der Vorschläge entwickelt haben. Durch diese Arbeit bereiten wir die Implementierung der Technik in Prototypen eines GW-Detektors vor, um die Kompatibilität mit aufgehängten Interferometern zu testen.

Wir haben denselben Aufbau benutzt, um die nichtklassische Verbesserung eines Interferometers bei tiefen Frequenzen durch gequetschte Zustände bei hohen Frequenzen zu zeigen. Hierbei wurde ein Heterodyn-Ausleseverfahren implementiert um limitierendes Rauschen bei niedrigen Frequenzen zu vermeiden. Die Anwendung von gequetschten Zuständen zentriert um die Lokaloszillator-Frequenz brachte eine Verbesserung des Signal-zu-Rausch-Verhältnisses von $3.4\,\mathrm{dB} \pm 0.3\,\mathrm{dB}$.

Zusätzlich habe ich eine kompakte Quetschlichtquelle bei 1064 nm mit einer Grundfläche von nur $0.8\,\mathrm{m}^2$ entworfen, aufgebaut und charakterisiert. Ich zeige Messungen von gequetschten Zuständen, mit einer Reduktion des Quantenrauschens von $10.7\,\mathrm{dB} \pm 0.2\,\mathrm{dB}$ unter dem Vakuumrauschen und präsentiere eine Rauschreduktion in einem Frequenzbereich von 70 kHz und 65 MHz.

Schlüsselwörter: Gravitationswellendetektion, frequenzabhängiges gequetschtes Licht, Verschränkung, zweifarbige Homodyndetektion

Contents

List of Figures

List of Tables

CHAPTER 1

Introduction

The recent detections of gravitational waves by the LIGO and Virgo laser interferometers [Ab16a, Ab16b, Ab17a, Ab17b, Ab17c, Ab17d] opened a new window for observations of our universe, the gravitational-wave astronomy [Pr72]. The first detections of binary black-hole mergers already proved the existence of binary stellar-mass black-hole systems and their gravitational-wave emission when inspiraling [Ab16a], allowed constraints on the population of binary black holes [Ab16b] and their formation channels [Ab16b, Ab17a, Ab17b] and provided new tests for general relativity [Ab16a, Ab16b, Ab17a, Ab17b]. The first detection of a gravitational-wave signal from an inspiraling binary neutron-star system [Ab17c] enabled multi-messenger observations together with measurements in the electromagnetic spectrum extending the capabilities of gravitational-wave astronomy. Even black-hole mergers [Ab17d] allow multi-messenger observations, e.g. to measure the Hubble constant, a cosmological property [So19]. Space-based laser interferometers, like the Laser Interferometer Space Antenna [Am12], are aiming to extend the observable spectrum of gravitational-waves to a range from 0.1 mHz to 1 Hz. Pulsar timing arrays are already searching for gravitational waves in the Nanohertz regime [De13], but without any detection yet. The audio-band is covered by ground-based detectors. So far, eleven highly significant detections of gravitational waves from ten binary black-hole mergers and one binary neutron-star merger were recorded accompanied by some less significant event candidates [Ab18a]. Future observation runs, including the KAGRA detector [So12], will extend this list by tens of binary events [Ab18b], providing a higher knowledge about the universe. Nevertheless, these observations with second-generation gravitational-wave detectors are only the beginning of gravitational-wave astronomy. Not yet observed, but expected to be seen in the future, are

gravitational waves from core-collapse supernovae [Ot09], continuous-wave sources like rotating neutron stars [Ab17f] and even a stochastic gravitational-wave background [Re17]. Upcoming third-generation ground-based detectors, like the Einstein Telescope [Pu10a] and the Cosmic Explorer [Ab17e], will have an improved performance to allow farther observation distances and to detect more and different events. Within several fields strong effort has started targeting many limiting noise contributions. Ideas for improved sensitivity include heavier mirror masses, different mirror materials [Pu10b] and coatings [St18], larger laser spots [Dw15], underground locations and sophisticated mirror-suspension systems [Pu10b]. For gravitational-wave detectors, quantum noise, being composed of shot noise and radiation-pressure noise [Ca81, Sc10], is among the highest limiting factors already in current systems [Aa15]. The application of squeezed states of light [Sc17] allows reducing quantum noise in one quadrature while increasing the noise in the orthogonal quadrature. The capability of squeezed light application reducing the shot-noise of gravitational-wave detectors was successfully demonstrated in the GEO600 detector [Gr13]. However, due to opto-mechanical coupling, at lower detection frequencies the light's radiation-pressure noise is the limiting factor, requiring a frequency-dependent rotation of the squeeze angle [Un83, JR90]. With parametric down-conversion, the state-of-the-art technique for producing strongly squeezed states [Sc18b,Va16], only frequency-independently a fixed quadrature can be squeezed [Sc17]. The optimal rotation of the squeeze angle can be achieved by reflecting the squeezed states off filter cavities before injecting them into the interferometer [Ki01]. To reduce intra-cavity losses these filter cavities need to be of the length of hundreds of meters [Ca16, LIGO18]. In 2017, Ma et al. proposed a scheme to use the signal-recycling cavity of the interferometer together with the Einstein-Podolsky-Rosen(EPR) entanglement [EPR35] of the squeezed states [Ha10] to achieve a broadband reduction of quantum noise. This idea avoids the cost-intensive filter cavities [Ma17]. This scheme implies a constraint of 3 dB on the improvement compared to the conventional injection of squeezed states. As proposed in [Br17], a similar scheme can be applied to broadband-enhance gravitational-wave detectors operating a detuned signal-recycling cavity.

This work was dedicated to an experimental realization of the schemes proposed in [Ma17] and [Br17] in a table-top experiment. For this purpose, we set up a 2.5 m-linear cavity emulating the signal-recycling cavity of a gravitational-wave detector. In contrast to the conventional schemes of squeezed-light enhanced gravitational-wave detectors, the squeezed states were produced detuned to the carrier light of the cavity. This field was reflected off the cavity and acquired a frequency-dependent phase shift. It was analyzed on one detector with two local oscillators at a lower and an upper sideband, exploiting the EPR-entanglement of the squeezed field. By adjustments on the relations between the center-frequency of the squeezed field and the frequencies of the local oscillators both proposals [Ma17] and [Br17] were addressed. We derived a theoretical model based on

the assumptions in [Ma17] and showed conditional measurements on squeezed states for different relations of the involved frequencies. The measurements and the theoretical model are in good accordance. This work provides the foundations for further investigations of the proposals on a gravitational-wave-detectors prototype scale.

The structure of this thesis is as follows:

- In chapter 2, the theoretical foundations to describe squeezed and entangled states of light are presented. It includes an introduction to non-linear optics to understand the parametric down-conversion process generating squeezed states.

- Chapter 3 is dedicated to the description of amplitude and phase modulation in a phasor picture. This is then extended to quantum noise and squeezed states. With this picture phase rotations of sidebands can explain the change of the squeeze angle forming the basis of later experiments.

- Laser-interferometric gravitational-wave detection and its current limits are the focus of chapter 4. Here, the impact of quantum noise on the detectors is explained and the proposals of [Ma17] and [Br17] for a broadband squeezed-light enhancement are presented.

- Chapter 5 explains the most important experimental methods used in this thesis like cavity-enhanced squeezed-vacuum generation and monochromatic and bichromatic homodyne detection of squeezed states.

- In chapter 6, a setup of a source of squeezed states at 1064 nm with a small footprint I designed, assembled and characterized is described.

- In chapter 7, we show the enhancement of measurements at low frequencies from higher-frequency squeezed states by using a heterodyne readout and a 2.5 m-linear cavity.

- Chapter 8 demonstrates the experimental realization of the schemes from [Ma17] and [Br17] in a table-top experiment. A theoretical model for our setup based on the work in [Ma17] is presented and compared to the experimental results.

- In chapter 9, all results are summarized and an outlook is given.

CHAPTER 2

Quantum-mechanical description of light

The full nature of light cannot be described within classical physics. Properties as *squeezing* or *entanglement*, being topics in this thesis, cannot even be explained semi-classically. They require a quantum mechanical approach. As a consequence, the amplitude and phase quadrature show uncertainties called *quantum noise*. This chapter is mainly based on the textbook [GK05] and the review article [Sc17].

2.1 The quantum-mechanical harmonic oscillator

A harmonic oscillator can be described quantum-mechanically by its Hamiltonian

$$\hat{H} = \frac{1}{2}\left(\hat{p}^2 + \omega^2 \hat{q}^2\right) , \tag{2.1}$$

where $\hat{p}$ and $\hat{q}$ are the canonical position and momentum operators and ω the angular frequency. $\hat{p}$ and $\hat{q}$ obey the commutation relation $[\hat{q},\hat{p}] = \mathrm{i}\hbar$. They can be replaced by the annihilation and creation operators defined by

$$\hat{a} = \frac{1}{\sqrt{2\hbar\omega}}\left(\omega\hat{q} + \mathrm{i}\hat{p}\right) , \tag{2.2}$$

$$\hat{a}^\dagger = \frac{1}{\sqrt{2\hbar\omega}}\left(\omega\hat{q} - \mathrm{i}\hat{p}\right) , \tag{2.3}$$

where $\hbar$ is the reduced Planck constant. They fulfill the commutation relation $\left[\hat{a},\hat{a}^\dagger\right] = 1$. The annihilation and creation operators are non-Hermitian and hence not observable. They can be used to express the amplitude- and phase-quadrature

operators

$$\hat{X} = \hat{a}^\dagger + \hat{a}\,, \tag{2.4}$$

$$\hat{Y} = \mathrm{i}\left(\hat{a}^\dagger - \hat{a}\right)\,. \tag{2.5}$$

These are dimensionless, Hermitian and proportional to the electric fields at the field's anti-nodes and nodes. They obey the commutation relation $\left[\hat{X},\hat{P}\right] = 2\mathrm{i}$. The Hamiltonian then reads

$$\hat{H} = \hbar\omega\left(\hat{a}^\dagger\hat{a} + \frac{1}{2}\right) = \hbar\omega\left(\hat{n} + \frac{1}{2}\right) = \hbar\omega\left(\hat{X}^2 + \hat{Y}^2\right)\,, \tag{2.6}$$

with $\hat{n} = \hat{a}^\dagger\hat{a}$ being the number operator, expressing the number of photons in a given state.

The variance of an operator $\hat{X}$, defined as

$$\Delta^2\hat{X} = \langle\hat{X}^2\rangle - \langle\hat{X}\rangle^2\,, \tag{2.7}$$

provides the quantum noise of the observable. For the ground state of the oscillator, where no photons are present ($\langle\hat{n}\rangle = 0$), the quadrature operators have a variance of $\Delta^2\hat{X} = \Delta^2\hat{Y} = 1$. Whereas in a classical picture, the field at a node vanishes, in a quantum-mechanical description it vanishes only on average, but noise is still present as described by the variance of the phase-quadrature operator. As well is the amplitude of a field only defined as the average field in its anti-nodes, but shows noise as described by the variance of the amplitude-quadrature operator. This noise is referred to as quantum noise and especially for the ground state of $\langle\hat{n}\rangle = 0$ as vacuum noise. The generalized quadrature operator can be introduced with an arbitrary angle between the amplitude and phase quadrature by applying a rotation

$$\hat{X}_\theta = \hat{X}\cos\theta + \hat{Y}\sin\theta \tag{2.8}$$

$$= \hat{a}\mathrm{e}^{-\mathrm{i}\theta} + \hat{a}^\dagger\mathrm{e}^{\mathrm{i}\theta} \tag{2.9}$$

The variance of the generalized quadrature operator for the ground state is $\Delta^2\hat{X}_\theta = 1$ for any angle θ.

2.2 Fock states

The photon number operator $\hat{n} = \hat{a}^\dagger\hat{a}$ given in equation (2.6) has eigenstates that are called *Fock states* $|n\rangle$. It has discrete eigenvalues n that give the deterministic number of photons in $|n\rangle$ so that

$$\hat{n}\,|n\rangle = n\,|n\rangle\,. \tag{2.10}$$

If no photons are present ($n = 0$) the state is called vacuum state $|0\rangle$. This is the ground state of the harmonic oscillator and therefore the state with the lowest energy. As equation (2.6) shows, the zero-point energy of the ground state $|0\rangle$ reads

$$\langle 0|\,\hat{H}\,|0\rangle = \hbar\omega\,\langle 0|\left(\hat{n}+\frac{1}{2}\right)|0\rangle = \frac{\hbar\omega}{2}\,. \tag{2.11}$$

It is remarkable that the energy is not vanishing even for the ground state in contrast to classical physics. Quantum noise results from this zero-point energy. The creation and annihilation operators raise or lower the number of the Fock state by one

$$\hat{a}^\dagger\,|n\rangle = \sqrt{n+1}\,|n+1\rangle\,, \tag{2.12}$$

$$\hat{a}\,|n\rangle = \sqrt{n}\,|n-1\rangle\ . \tag{2.13}$$

Any Fock state can mathematically be created out of the vacuum state by applying the creation operator n times,

$$|n\rangle = \frac{\left(\hat{a}^\dagger\right)^n}{\sqrt{n!}}\,|0\rangle\ . \tag{2.14}$$

2.3 Coherent states

Laser light can be described by coherent states $|\alpha\rangle$. In contrast to Fock states coherent states do not have a precise photon number but a Poissonian distribution with an average photon number of $\bar{n} = |\alpha|^2$, where α is a complex number, and a variance of the same value $V = |\alpha|^2$. Coherent states are defined as eigenstates of the annihilation and creation operators

$$\hat{\alpha}\,|\alpha\rangle = \alpha\,|\alpha\rangle\ , \tag{2.15}$$

$$\langle\alpha|\,\hat{\alpha}^\dagger = \langle\alpha|\,\alpha^*\,, \tag{2.16}$$

with complex eigenvalues α, α^* respectively. Coherent states can be expressed by a superposition of Fock states $|n\rangle$ as

$$|\alpha\rangle = \mathrm{e}^{-\frac{1}{2}|\alpha|^2}\sum_{n=0}^{\infty}\frac{\alpha^n}{\sqrt{n!}}\,|n\rangle\ . \tag{2.17}$$

They can be described mathematically by applying the displacement operator $\hat{D}(\alpha) = \mathrm{e}^{\alpha\hat{a}^\dagger - \alpha^*\hat{a}}$ to the Fock state $|0\rangle$

$$|\alpha\rangle = \hat{D}(\alpha)\,|0\rangle\ . \tag{2.18}$$

2.4 Heisenberg's uncertainty principle

Any two Hermitian, non-commuting observables can not be measured at the same time with an arbitrary precision [He27]. It is based on the fact that measuring one observable influences the measured system in the other observable. Hence, the measurement of the other observable is disturbed by the first measurement. Two observables fulfilling the commutation relation [Ro29]

$$\left[\hat{A},\hat{B}\right] = \hat{C} \tag{2.19}$$

obey the uncertainty relation

$$\Delta^2\hat{A} \cdot \Delta^2\hat{B} \geq \frac{1}{4}\left|\left\langle\hat{C}\right\rangle\right|^2 . \tag{2.20}$$

Using $\left[\hat{X},\hat{P}\right] = 2\mathrm{i}$, the uncertainty relation for the amplitude and phase quadrature operators is given by

$$\Delta^2\hat{X} \cdot \Delta^2\hat{Y} \geq 1 . \tag{2.21}$$

The relation is true for all other orthogonal quadrature operators $\hat{X}_\phi$ and $\hat{X}_{\phi+\pi/2}$.

$$\Delta^2\hat{X}_\phi \cdot \Delta^2\hat{X}_{\phi+\pi/2} \geq 1 . \tag{2.22}$$

The vacuum state and coherent states of light minimize the left side of equation (2.22) and are called minimum uncertainty states.

2.5 Squeezed states of light

Every state has to obey Heisenberg's uncertainty principle from equation (2.22). The vacuum state and coherent states of light show equal variances for all quadrature operators $\hat{X}_\theta$. Nevertheless, it is possible to describe (and also create, see chapter 5.4) states that have a variance in one quadrature $\hat{X}_\theta$ below the variance of the ground state

$$\Delta^2\hat{X}_\theta < 1 . \tag{2.23}$$

To fulfill Heisenberg's uncertainty relation, the orthogonal quadrature must show an increased variance

$$\Delta^2\hat{X}_{\theta+\pi/2} \geq \frac{1}{\Delta^2\hat{X}_\theta} > 1 . \tag{2.24}$$

If the equal sign holds for equation (2.24) the state remains a state of minimum uncertainty.

States that show a reduced variance for at least one angle θ are called *squeezed states*. A way to quantify this property is to define the *squeeze angle* Θ and the *squeeze factor* S (or equivalently the *squeeze parameter* r). The squeeze angle is

the angle Θ for which the variance of the respective operator $\Delta^2\hat{X}_\Theta$ is the lowest of all quadratures. The squeeze factor S and squeeze parameter r, being a measure for the factor by which the variance of a squeezed state is below the vacuum variance, are defined by

$$S = \mathrm{e}^{-2r} = \frac{\Delta^2\hat{X}_\Theta}{\Delta^2\hat{X}_{\mathrm{vac}}}\,. \tag{2.25}$$

The squeeze factor S is often referred to on a logarithmic scale and given in decibel (dB)

$$S_{\mathrm{dB}} = -10\cdot\log_{10}\left(\frac{\Delta^2\hat{X}_\Theta}{\Delta^2\hat{X}_{\mathrm{vac}}}\right)\,. \tag{2.26}$$

Mathematically, squeezed vacuum states can be generated by applying the squeeze operator $\hat{S}(\xi)$ to the ground state $|0\rangle$. The operator is defined as

$$\hat{S}(\xi) = \mathrm{e}^{\frac{1}{2}(\xi^*(\hat{a})^2 - \xi(\hat{a}^\dagger)^2)}\,, \tag{2.27}$$

where $\xi = r\mathrm{e}^{\mathrm{i}\theta}$ and r and θ being squeeze parameter and angle. Squeezed coherent states can be generated by applying the displacement operator $\hat{D}(\alpha)$ to the squeezed vacuum

$$|\alpha,\xi\rangle = \hat{D}(\alpha)\hat{S}(\xi)\,|0\rangle\,. \tag{2.28}$$

2.6 Phase space representations

States of light can be visualized in a plane that is spanned by the amplitude and phase quadrature operators $\hat{X}$ and $\hat{Y}$. Their uncertainties have to be taken into account. In figure 2.1 representations of a vacuum state (a) and a coherent state (b) in the phase space are shown. The coherent state has a classical amplitude α in contrast to the vacuum state. The uncertainties are depicted with circles proportional to the variance of the quadrature operators (being equal for all quadratures here). The probability distribution for the quadrature operators is Gaussian and centered around the classical amplitude. Squeezed states of light have a reduced variance below the vacuum variance for at least one angle. Their uncertainties are therefore not equal for all angles. Figure 2.2 shows the representations of a vacuum squeezed (a) and a coherent squeezed state (b) in the phase space, both squeezed in the amplitude quadrature. The uncertainties are now depicted by ellipses. They illustrate a squeezed variance along the amplitude quadrature and anti-squeezed along the phase quadrature. This is the origin of the term *squeezed states*.

The vacuum state has no defined phase and therefore it is only depicted as squeezed in the amplitude quadrature for convenience. In an experimental implementation the quadrature is only defined relative to an auxiliary field (e.g. a control field).

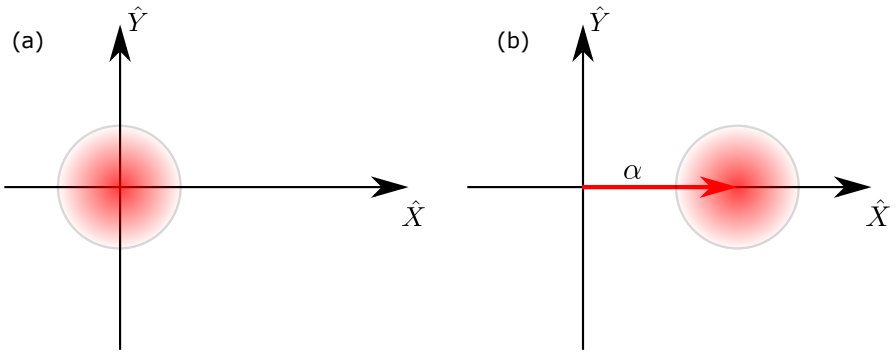

Figure 2.1: Representations of a vacuum state (a) and a coherent state of light (b) in phase space. The coherent state has an amplitude of α. For both states their quantum uncertainty is depicted with a circle around their amplitudes.

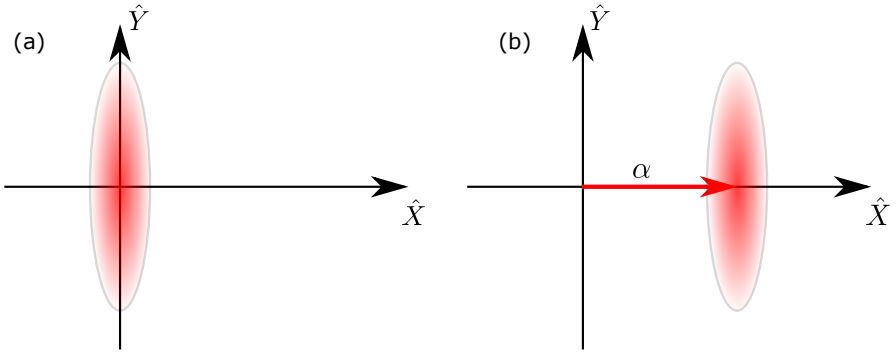

Figure 2.2: Representations of a squeezed vacuum (a) and displaced squeezed state of light (b) in phase space. The amplitude of the displaced state is α. Both states are squeezed along the amplitude quadrature. Their quantum uncertainty is depicted with an ellipse around their amplitudes.

A full representation of a physical state can be given by the Wigner function. It is defined as

$$W(X,Y) = \frac{1}{2\pi\hbar}\int_{-\infty}^{\infty}\left\langle X+\frac{x}{2}\right|\hat{\rho}\left|X-\frac{x}{2}\right\rangle \mathrm{e}^{\frac{\mathrm{i}Yx}{2}}\mathrm{d}x\,, \tag{2.29}$$

where $\hat{\rho}$ is the density operator of the system. The Wigner function is a quasi-probability distribution and can also have negative values.

The Wigner function can be used to calculate the probability distributions for the amplitude or phase quadrature operators by integrating over the orthogonal quadrature operator respectively

$$\mathrm{p}(X) = \int_{-\infty}^{\infty} W(X,Y)\mathrm{d}Y\,, \tag{2.30}$$

$$\mathrm{p}(Y) = \int_{-\infty}^{\infty} W(X,Y)\mathrm{d}X\,. \tag{2.31}$$

Figure 2.3 shows the Wigner function of a vacuum state. It is symmetric around the origin and hence the projections onto the quadrature operators are the same for all directions. They have a variance of $\Delta^2\hat{X}_\theta = 1$ for all angles θ. Figure 2.4 shows a squeezed vacuum state with a squeeze factor of four (= 6 dB). It is squeezed along the amplitude quadrature. A projection onto the amplitude-quadrature operator yields a reduced (squeezed) variance, whereas a projection onto the phase-quadrature operator has an increased (anti-squeezed) variance.

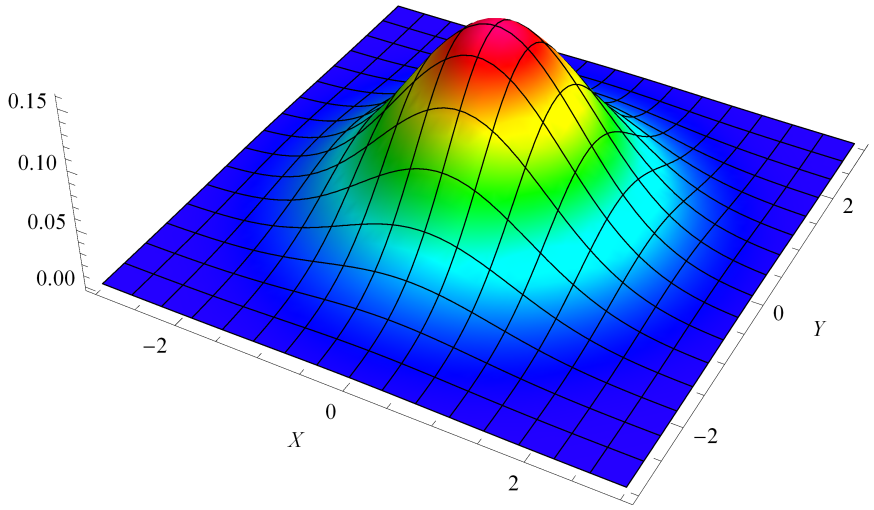

Figure 2.3: Wigner function of a vacuum state of light. The function is rotationally symmetric around the origin. A projection onto the quadrature operators leads to equal variances for all projection angles.

2.7 The influence of losses on squeezed states

In an experimental implementation, light fields experience optical losses. Whereas coherent states only experience a reduction of their amplitude by losses, a squeezed state's squeeze factor is reduced (although it remains squeezed). The influence of losses can be described by superimposing the squeezed state and a vacuum state on a beam splitter as illustrated in figure 2.5. Since the vacuum state has a larger variance than the variance of the squeezed quadrature $\hat{X}_\theta$, the superposition of these two states will have an increased variance in the quadrature $\hat{X}_\theta$ with respect

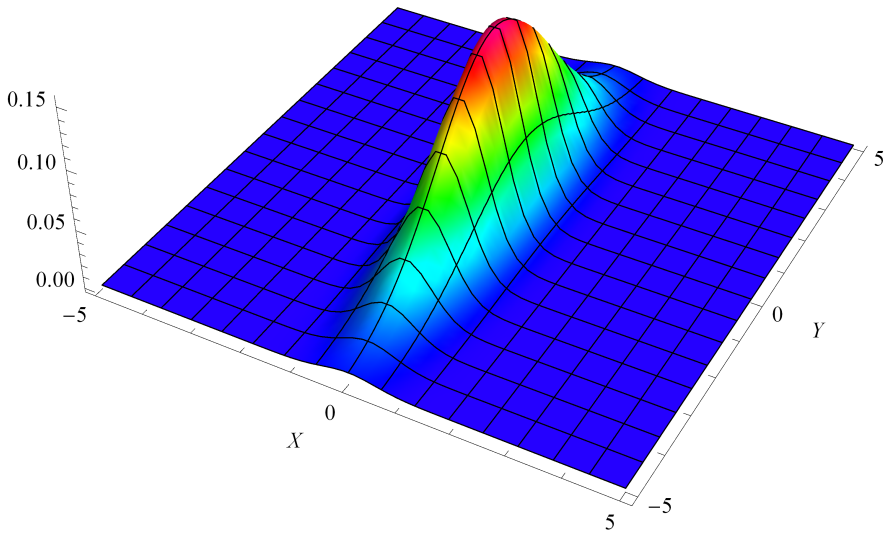

Figure 2.4: Wigner function of a squeezed vacuum state of light. The squeeze factor is four (= 6 dB) and the squeeze angle is chosen along the amplitude quadrature. The function is not rotationally symmetric anymore and projections onto the amplitude (or phase) quadrature lead to variances that are a factor four smaller (or larger) than the variance of a vacuum state.

to the variance of the squeezed state. This can be written as

$$\Delta^2 \hat{X}_{\theta,\text{loss}} = (1 - L) \cdot \Delta^2 \hat{X}_\theta + L \cdot \Delta^2 \hat{X}_{\text{vac}} \,, \tag{2.32}$$

where L is the loss that can be modeled by the power transmittance T of the beam splitter in figure 2.5.

Losses can be caused by non-perfect mirrors (as described in the beam splitter picture), absorption in optical materials, non-perfect mode matchings to resonators or the readout local oscillator and non-perfect quantum efficiencies of the photo diodes.

Figure 2.6 shows the effect of losses on the noise power compared to vacuum noise (given in decibel) for different initial squeeze factors. It is clearly visible that the influence of loss acts stronger on the squeezed than on the anti-squeezed noise power. This cyn be explained by the higher influence of the noise of the vacuum state on the relatively small noise power of the squeezed quadrature in contrast to the small influence on the relatively large noise power in the anti-squeezed quadrature.

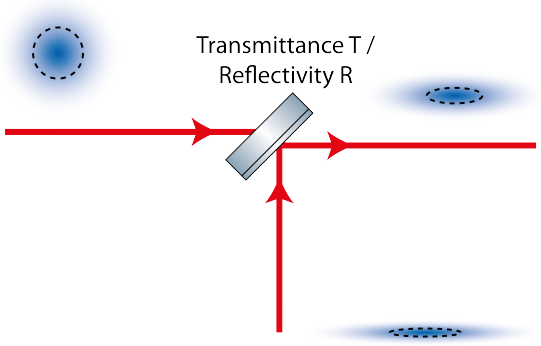

Figure 2.5: The influence of losses on squeezed states modeled with a beam splitter. The effect of losses can be understood by mixing a squeezed state with a vacuum state on a beam splitter. The squeezed state is depicted by the ellipse in phase space coming from below, the vacuum state is depicted by the circle in phase space coming from the left. The beam splitter has a power reflectivity R and power transmittance T. The resulting ellipse on the right of the beam splitter is still squeezed but with a lower squeeze factor. The upper port of the beam splitter can be neglected in this picture.

Out of measured noise powers, here given in decibel relative to vacuum noise, of the squeezed quadrature $\mathrm{Var}(\hat{X})_{\mathrm{dB}}$ and anti-squeezed quadrature $\mathrm{Var}(\hat{Y})_{\mathrm{dB}}$ the total loss L can by determined by

$$L = \frac{1 - 10^{\frac{\mathrm{Var}(\hat{X})_{\mathrm{dB}}}{10}} \cdot 10^{\frac{\mathrm{Var}(\hat{Y})_{\mathrm{dB}}}{10}}}{2 - 10^{\frac{\mathrm{Var}(\hat{X})_{\mathrm{dB}}}{10}} - 10^{\frac{\mathrm{Var}(\hat{Y})_{\mathrm{dB}}}{10}}} . \tag{2.33}$$

2.8 Non-linear optics

To explain the generation of nonclassical states (like squeezed states) higher-order polarization effects in media are needed. An electro-magnetic wave $E(t) = E_0 \cos(\omega_\mathrm{p} t)$ traveling through a medium excites the electrons in the medium to oscillate. These oscillations can be described by the polarization $P(E)$ in dependence of the electro-magnetic field $E(t)$ [Bo08]

$$P(E(t)) = \epsilon_0 \left(\chi^{(1)} E(t) + \chi^{(2)} E(t)^2 + \chi^{(3)} E(t)^3 + ... \right) , \tag{2.34}$$

where $\chi^{(\mathrm{i})}$ is the i-th order susceptibility and a material property. Typically, either the higher order terms of the susceptibility are too small or the amplitude of the electro-magnetic field is too low to observe higher-order effects. Then, the polarization is given by $P(E) = \epsilon_0 \chi^{(1)} E_0 \cos(\omega_\mathrm{p} t)$. The proportionality of the cosine to the frequency ω_p of the electro-magnetic field indicates that the emitted field of the electrons has the same frequency as the incoming field.

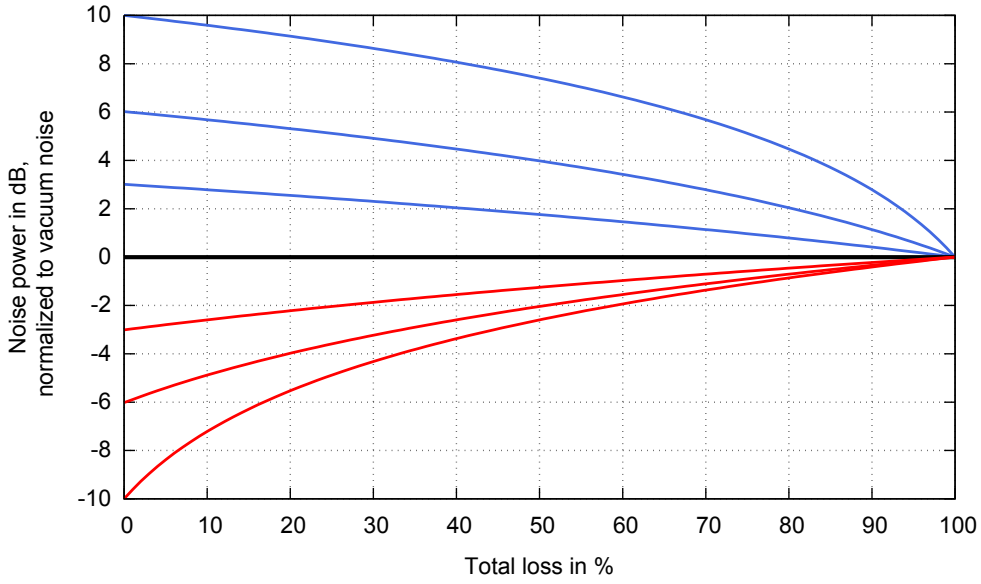

Figure 2.6: The influence of losses on the noise power of squeezed states for initial squeeze factors of 3 dB, 6 dB and 10 dB. The red curves show the noise power of the squeezed quadrature and the blue curves show the noise power of the anti-squeezed quadratures according to (2.33). It is clearly visible that the influence of loss acts stronger on the squeezed then on the anti-squeezed noise power. Even low loss reduces the squeezed properties drastically.

By using special materials with larger higher-order susceptibilities and applying higher optical powers, it is possible to access the quadratic terms of the polarization, which must then be written as $P(E) = \epsilon_0 \left(\chi^{(1)} E + \chi^{(2)} E^2\right)$. The quadratic term of the electro-magnetic field can be expressed as

$$E^2 = \left(E_0 \cos(\omega_\mathrm{p} t)\right)^2 = \frac{E_0^2}{2} \left(1 + \cos(2\omega_\mathrm{p} t)\right) , \tag{2.35}$$

where a proportionality to twice the frequency ω_p is visible. For energy conservation two photons at the frequency ω_p must be involved in this process and one photon at the frequency $2\omega_\mathrm{p}$, since the energy of one photon is proportional to its frequency, $E = \hbar\omega$.

If two photons of the frequency ω_p create one photon at the frequency $2\omega_\mathrm{p}$ the process is called *second-harmonic generation*. Nevertheless, the process can also take place in the reversed order where one photon at the frequency $2\omega_\mathrm{p}$ is used to create two photons at the frequency ω_p. This process is called *down conversion* and is the process that was used here to create squeezed states of light. The down-conversion process will not necessarily produce photons of the same frequency ω_p, but at frequencies $\omega_\mathrm{p} \pm \Delta\omega$. They can be described as sidebands of frequency $\Delta\omega$

with respect to the carrier at frequency ω_p. The photons created in the very same process show quantum correlations of their quadrature operators (see chapter 2.9 and 3.4). Figure 2.7 illustrates both processes in an energy picture.

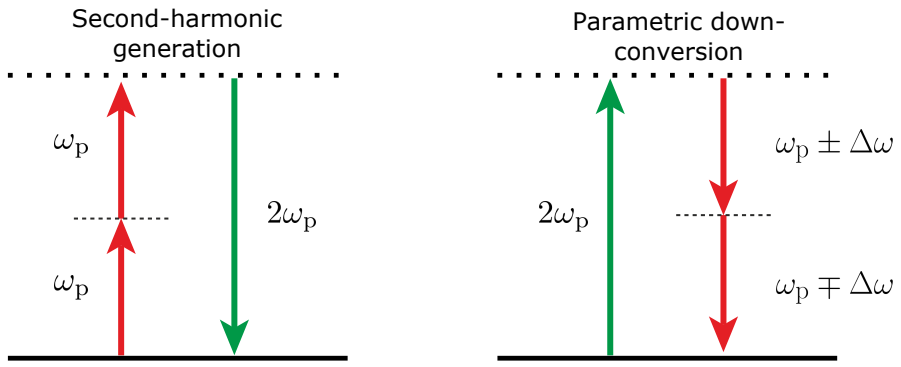

Figure 2.7: Second-harmonic generation and parametric down conversion process in the energy picture. The left panel shows a second-harmonic generation process, where the energy of two photons at the frequency ω_p is taken to create one photon at the frequency $2\omega_p$. The right panel shows a parametric down conversion process, where the energy of one photon at the frequency ω_{2p} is taken to create two photons at the frequencies $\omega_p \pm \Delta\omega$. Since these photons are generated in the very same process, they show quantum correlations in their quadrature operators.

2.9 Entanglement

Entanglement is a property of a physical system consisting of two or more subsystems (modes). This system is described in a Hilbert space $\mathcal{H}_{tot}$ being the tensor product of the Hilbert spaces of the subsystems [We89]

$$\mathcal{H}_{tot} = \mathcal{H}_1 \otimes \mathcal{H}_2 \otimes ... \otimes \mathcal{H}_n \,. \tag{2.36}$$

If such a system is separable, it can be described by the tensor product of the subsystems. If a system can only be described by a single function it is called entangled. In Einstein-Podolsky-Rosen entangled systems [EPR35], it is possible to measure sums and differences of the entangled properties in different subsystems with an arbitrary high precision, contrary to the intuition. In the case of perfect entanglement in the quadrature operators of subsystems A and B, this can be stated as

$$\Delta^2 \left(\hat{X}_A - \hat{X}_B \right) = 0 \,, \tag{2.37}$$

$$\Delta^2 \left(\hat{Y}_A + \hat{Y}_B \right) = 0 \,, \tag{2.38}$$

where the amplitude quadrature operators $\hat{X}_{\mathrm{A,B}}$ are correlated and the phase quadrature operators $\hat{Y}_{\mathrm{A,B}}$ are anti-correlated.

Squeezed states of light can be described by two photons at the upper and lower sideband $\omega_{\mathrm{p}} \pm \Delta\omega$. The quadrature operators of the photons at each sideband for a squeezed state have a variance of

$$\Delta^2\hat{X}(\omega_{\mathrm{p}} + \Delta\omega) = \Delta^2\hat{X}(\omega_{\mathrm{p}} - \Delta\omega) = \frac{\mathrm{e}^{2r} + \mathrm{e}^{-2r}}{2} \geq 1\,, \tag{2.39}$$

$$\Delta^2\hat{Y}(\omega_{\mathrm{p}} + \Delta\omega) = \Delta^2\hat{Y}(\omega_{\mathrm{p}} - \Delta\omega) = \frac{\mathrm{e}^{2r} + \mathrm{e}^{-2r}}{2} \geq 1\,. \tag{2.40}$$

Therefore, the uncertainty of each quadrature of each sideband is larger then the uncertainty of a vacuum state if the state is squeezed ($r > 0$). Squeezed variances of light fields can be explained by the correlations of the quadrature operators analogous to equation (2.37). In the case of an amplitude squeezed state the variances of the sum of the amplitude operators and difference of the phase operators read

$$\Delta^2\left(\hat{X}(\omega_{\mathrm{p}} + \Delta\omega) + \hat{X}(\omega_{\mathrm{p}} - \Delta\omega)\right) = \mathrm{e}^{-2r} \leq 1\,, \tag{2.41}$$

$$\Delta^2\left(\hat{Y}(\omega_{\mathrm{p}} + \Delta\omega) - \hat{Y}(\omega_{\mathrm{p}} - \Delta\omega)\right) = \mathrm{e}^{-2r} \leq 1\,. \tag{2.42}$$

They are below the vacuum variance due to their quantum-correlations.

CHAPTER 3

Light fields in the phasor picture

The phasor picture is a useful tool to visualize effects like amplitude or phase modulation [Ma06]. In addition, also quantum noise and squeezed states of light can be explained as sidebands at $\pm\Omega$ of a carrier ω_0 [Sc17,Ch07]. In an experiment, a measurement is always performed at a certain sideband frequency Ω within a bandwidth $\Delta\Omega$. For visualization this bandwidth is chosen to be infinitely small in this chapter.

3.1 The phasor picture

The electric field of a classical light field can be described by $E(t) = E_0 e^{i\omega_0 t}$, where E_0 is the amplitude and $\omega_0 t$ the phase of the electric field. In the complex plane the electric field is rotating counterclockwise with time t. For illustrations, typically a coordinate system rotating with the same frequency ω_0 is chosen to get a stationary picture, the so-called *rotating frame picture*. If fields at other frequencies e.g. $\Omega \neq \omega_0$ are included in the phasor diagram in a rotating frame, these components rotate with a rate proportional to the difference frequency $\omega_0 - \Omega$ in time. They rotate clockwise if $\omega_0 > \Omega$ and counterclockwise if $\omega_0 < \Omega$. An example for the phasor picture of two fields at frequencies ω_0 and $\Omega < \omega_0$ at different times is illustrated in figure 3.1.

The phasor picture in the rotating frame allows for an easy picture of superpositioning of light fields at different frequencies Ω. The superposition is the addition of all phasors, where each phasor rotates with its own frequency $\omega_0 - \Omega$.

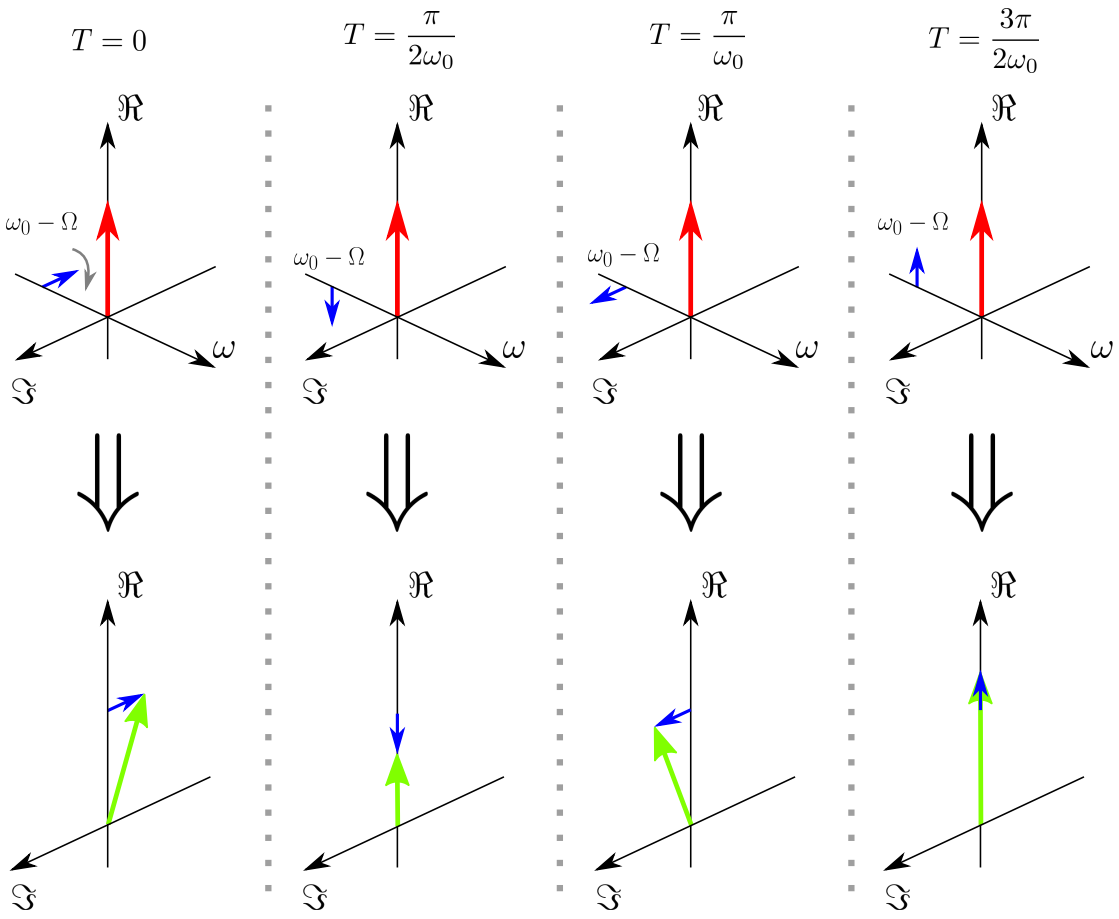

Figure 3.1: Phasor picture for a single sideband in a rotating frame for frequency ω_0. The sideband (blue arrow) has a frequency of $\omega_0 - \Omega$ and rotates clockwise in time whereas the carrier (red arrow) does not rotate. The upper panel shows each sidebands' evolution in time. The lower panel is the superposition and time evolution of the fields. For clarity here only the sideband but not the carrier is shown.

3.2 Amplitude modulation of a classical light field

A modulation of only the amplitude of a light field $E(t) = E_0 \mathrm{e}^{\mathrm{i}\omega_0 t}$ with the modulation frequency Ω and modulation depth m can be written as

$$E_{\mathrm{am}}(t) = E_0 \left(1 + m\cos(\Omega t)\right) \mathrm{e}^{\mathrm{i}\omega_0 t} \tag{3.1}$$

$$= E_0 \left(1 + \frac{m}{2}\left[\mathrm{e}^{\mathrm{i}\Omega t} + \mathrm{e}^{-\mathrm{i}\Omega t}\right]\right) \mathrm{e}^{\mathrm{i}\omega_0 t} \tag{3.2}$$

$$= E_0 \left(\mathrm{e}^{\mathrm{i}\omega_0 t} + \frac{m}{2}\mathrm{e}^{\mathrm{i}(\omega_0+\Omega)t} + \frac{m}{2}\mathrm{e}^{\mathrm{i}(\omega_0-\Omega)t}\right). \tag{3.3}$$

In addition to the carrier light at frequency ω_0, two new terms at the frequencies $\omega_0 \pm \Omega$ with amplitudes $E_0 \frac{m}{2}$ are generated. They are typically called upper and lower sidebands with respect to the carrier light. Figure 3.2 illustrates an amplitude modulation in a phasor diagram in a rotating frame with the frequency of the carrier field for different times. The upper and lower sidebands superimpose with the carrier field such that only the total amplitude (=length of the phasor) changes and the phase remains unchanged.

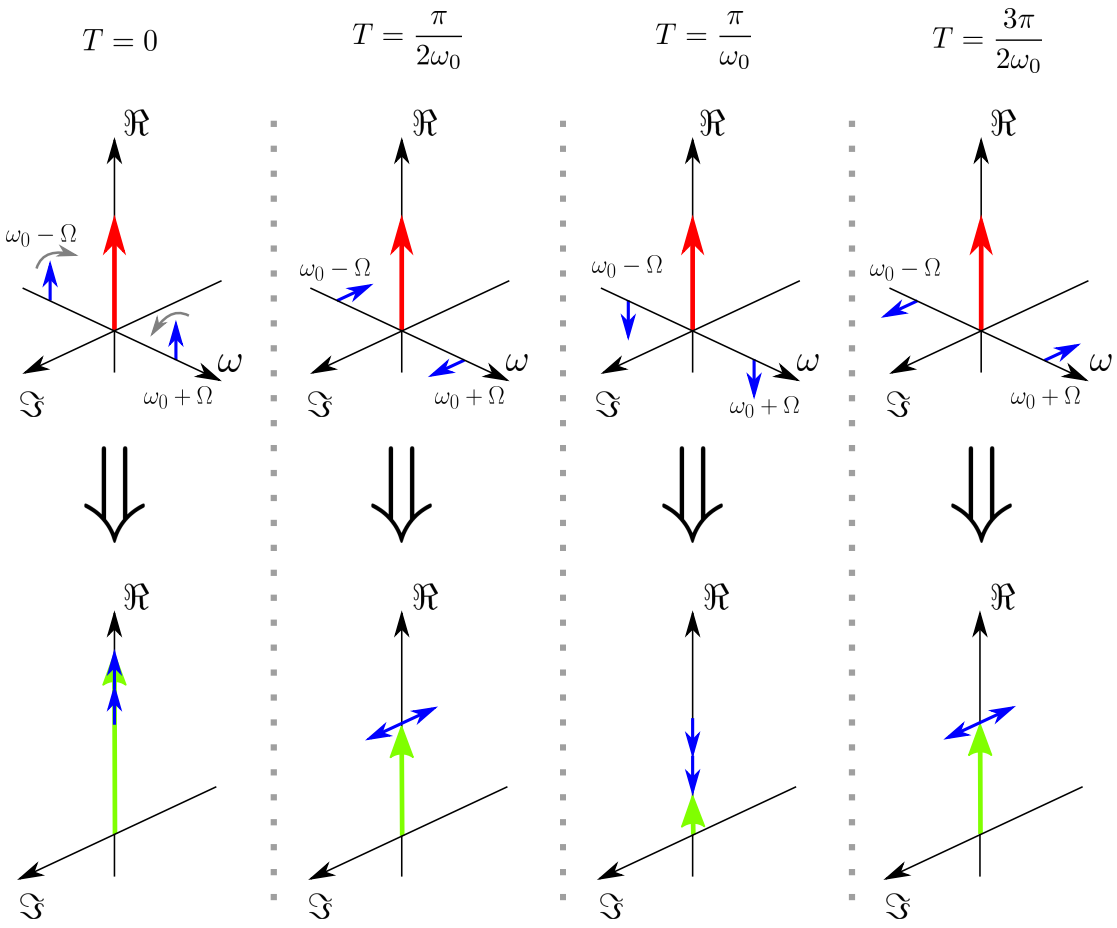

Figure 3.2: Phasor picture for an amplitude modulation in a rotating frame for frequency ω_0. The sidebands (blue arrows) have frequencies of $\omega_0 \pm \Omega$ and rotate clockwise (lower sideband) and counterclockwise respectively (upper sideband) in time whereas the carrier (red arrow) does not rotate. The upper panel shows each sidebands' evolution in time. The lower panel is the superposition and time evolution of the fields (green arrow). For clarity, here only the sidebands but not the carrier are shown. The sidebands interfere in such a way with the carrier that only the amplitude of the resulting field is changed but not its phase.

3.3 Phase modulation of a classical light field

A modulation of the phase of a light field $E(t) = E_0 e^{i\omega_0 t}$ with the modulation frequency Ω and modulation depth m can be written as

$$\begin{aligned} E_{\mathrm{pm}}(t) =& E_0 e^{i(\omega_0 t + m\cos(\Omega t))} && (3.4)\\ \approx& E_0 e^{i\omega_0 t}\left[J_0(m) + iJ_1(m)\left(e^{i\Omega t} + e^{-i\Omega t}\right)\right] && (3.5)\\ =& E_0\left[e^{i\omega_0 t} + i\frac{m}{2}e^{i(\omega_0+\Omega)t} + i\frac{m}{2}e^{i(\omega_0-\Omega)t}\right], && (3.6)\end{aligned}$$

where $J_{\mathrm{j}}(m)$ are the Bessel functions of jth order. The approximation in the second line is only valid for $m \ll 1$. For higher modulation indices, additional sidebands at the frequencies $\pm n\Omega$ are created. Here, two sidebands at frequencies $\omega_0 \pm \Omega$ with amplitudes $E_0\frac{m}{2}$ appear in addition to the carrier field. In contrast to the amplitude modulation they show a phase shift of $\pi/2$ with respect to the carrier. As it can be seen in figure 3.3 this phase shift leads to a superposition of the sidebands with the carrier in a way that the length is constant (for small modulation indices), but only the phase of the carrier is modulated.

3.4 Quantum noise in the phasor picture

For illustrating quantum noise, the axes are changed from the complex plane to the amplitude and phase quadrature operators. Contrary to the classical picture, for every sideband frequency an uncertainty in the quadrature operators with the variance of 1/2 needs to be introduced. This is the quantum noise for every sideband frequency. If no carrier at frequency ω_0 is present this is the vacuum noise. It is important to say, that the noises are initially totally uncorrelated for each sideband frequency. In a measurement at the sideband frequency $\pm\Omega$ around the frequency ω_0 , the noises from the upper and lower sideband are added. Their variances are added up since they are uncorrelated and the total variance is one. Figure 3.4 shows an example of quantum noise for the sidebands $\pm\Omega$.

For squeezed fields two correlated photons at sideband frequencies $\pm\Omega$ are produced as described in chapter 2.8. These sidebands have increased uncertainties compared to the vacuum uncertainties. But these uncertainties show correlations and anti-correlations for the sideband frequencies $\pm\Omega$. Depending on the phase of these correlations with respect to the carrier field the squeeze angle can be chosen. This is analogous to the amplitude and phase modulation in the classical picture. If no carrier is present, a squeezed vacuum field is produced. This has by definition no certain phase and the squeeze angle can therefore only be stated with respect to an auxiliary field. Figure 3.5 illustrates these correlations of the sidebands for an amplitude squeezed field. Correlations in the quantum noise are depicted by the symbols + and ∘, respectively.

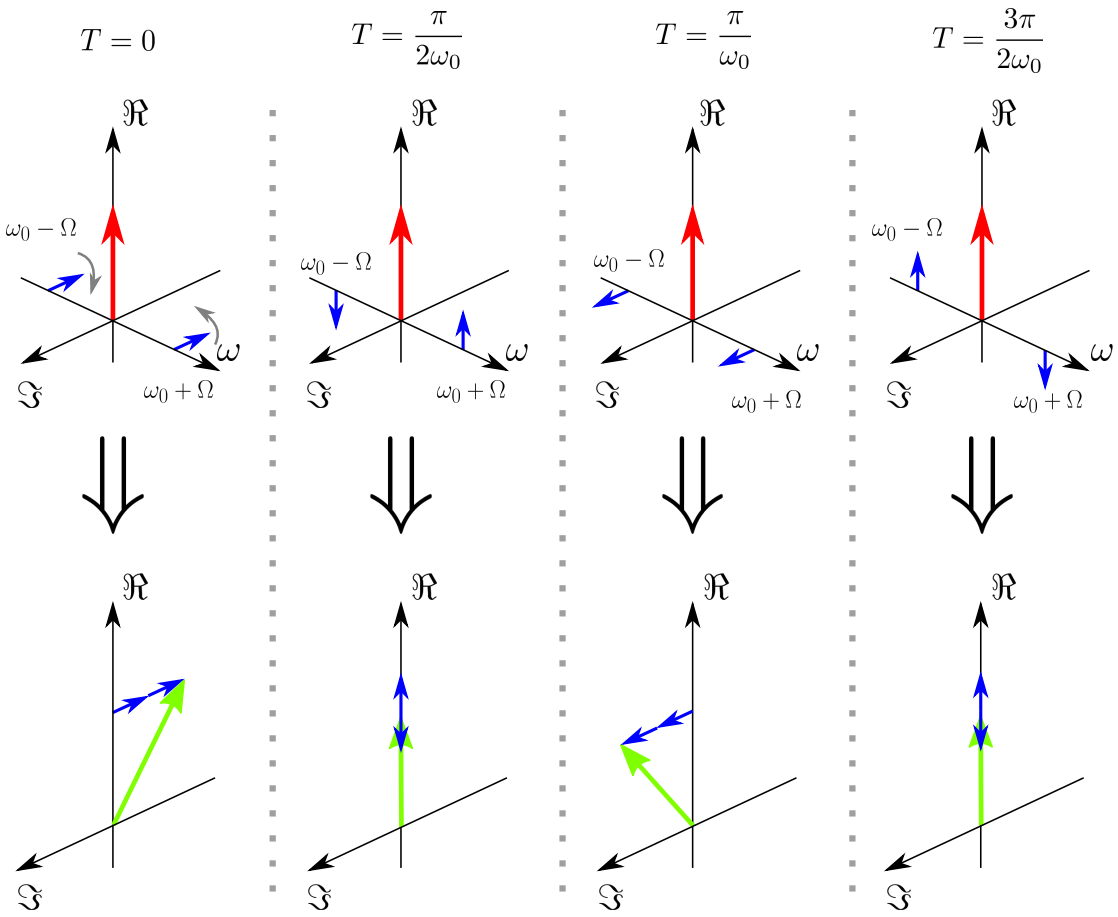

Figure 3.3: Phasor picture for a phase modulation in a rotating frame for frequency ω_0. The sidebands (blue arrows) have frequencies of $\omega_0 \pm \Omega$ and rotate clockwise (lower sideband) and counterclockwise respectively (upper sideband) in time whereas the carrier (red arrow) does not rotate. The upper panel shows each sidebands' evolution in time. The lower panel is the superposition and time evolution of the fields (green arrow). For clarity, here only the sidebands but not the carrier are shown. The sidebands interfere in such a way with the carrier that only the phase of the resulting field is changed but not its amplitude.

Later in this thesis, a rotation in phase of only one side of the spectrum (e.g. the lower sidebands) will be discussed. This does *not* reduce the correlations between upper and lower sidebands but rotates the squeeze angle of the resulting field. If a phase rotation of Θ is applied to one of the sidebands, the resulting squeeze angle is rotated by $\Theta/2$. Figure 3.6 illustrates a phase rotation by $\pi/2$ of the lower sideband of an initially amplitude squeezed state. It shows the resulting field to be squeezed at an angle of $\pi/4$.

The phase shift can be different for each sideband frequency. By applying such a

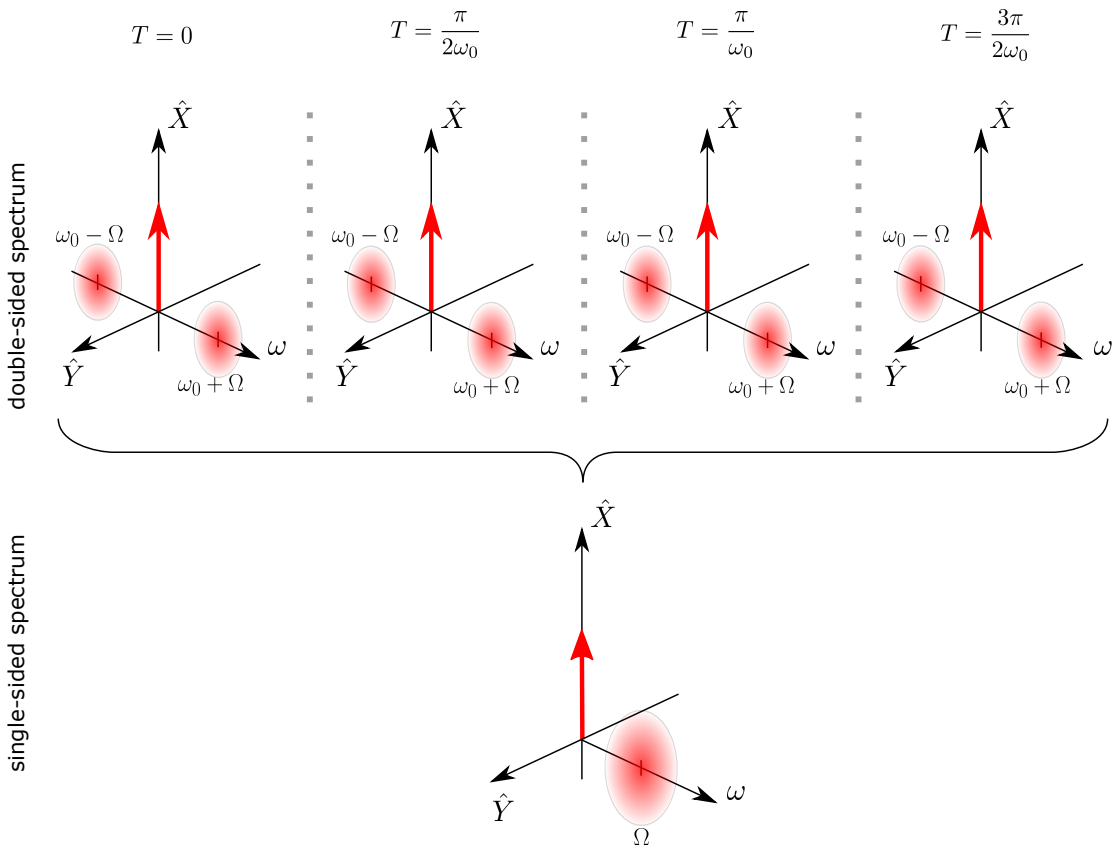

Figure 3.4: Phasor picture for vacuum quantum noise in a rotating frame for frequency ω_0. The quantum noises (red circles) are at frequencies of $\omega_0 \pm \Omega$ and rotate clockwise (lower sideband) and counterclockwise respectively (upper sideband) in time, whereas the carrier (red arrow) does not rotate. The upper panel shows each sidebands' evolution in time in a double-sided spectrum. The variance of each uncertainty is 1/2. The lower panel shows a single-sided spectrum. The variance of the added uncertainty at the sideband frequency Ω is one.

phase transition, a frequency-dependent squeeze angle can be achieved. Figure 3.7 shows squeezed states at the three sideband frequencies Ω, 2Ω and 3Ω. Initially, all states were amplitude squeezed but the lower sidebands acquired a gradient phase transition from 0 (for $-\Omega$) over $\pi/2$ (for -2Ω) to π (for -3Ω). The resulting squeeze angles are rotated from 0 (amplitude squeezed) to $\pi/2$ (phase squeezed).

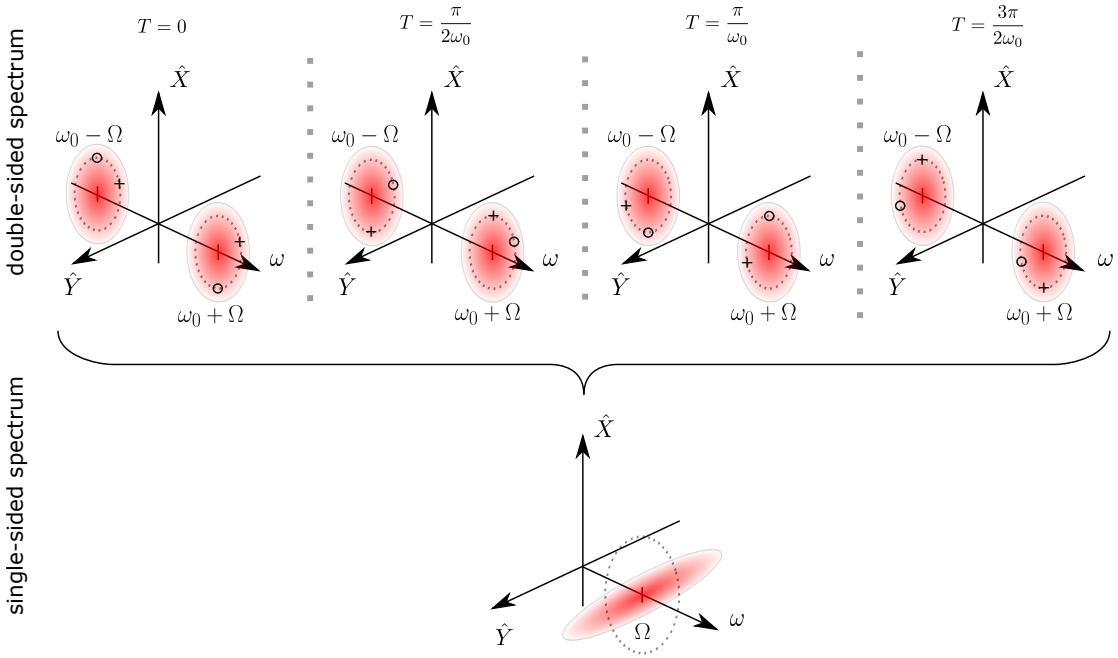

Figure 3.5: Phasor picture for an amplitude squeezed vacuum state in a rotating frame for frequency ω_0. The quantum noises (red circles) are at frequencies of $\omega_0 \pm \Omega$ and rotate clockwise (lower sideband) and counterclockwise respectively (upper sideband) in time. Since it is a vacuum state, no carrier is present. The correlations in the upper and lower sideband that arise from their creation in a down-conversion process are marked with the symbols + and ∘. The upper panel shows each sidebands' evolution in time in a double-sided spectrum. The variance of each uncertainty is larger than for the ground state (grey dashed line). The lower panel shows a single-sided spectrum. Due to the correlations of the sidebands the quantum noise is squeezed in the amplitude quadrature but anti-squeezed in the phase quadrature.

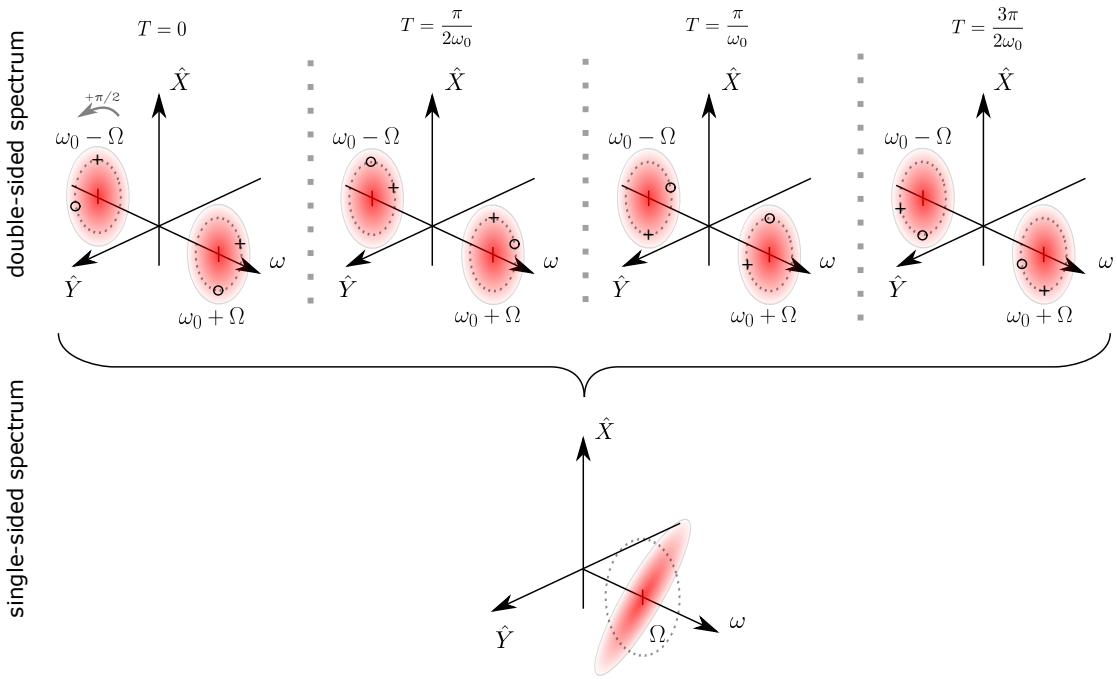

Figure 3.6: Phasor picture for an one-sided phase shift of an initially amplitude squeezed state in a rotating frame for frequency ω_0. The quantum noises (red circles) are at frequencies of $\omega_0 \pm \Omega$ and rotate clockwise (lower sideband) and counterclockwise respectively (upper sideband) in time. Since it is a vacuum state, no carrier is present. The correlations in the upper and lower sideband that arise from their creation in a down-conversion process are marked with the symbols + and ∘. The lower sideband is phase shifted by $\pi/2$ with respect to the initially amplitude-squeezed state. The upper panel shows each sidebands' evolution in time in a double-sided spectrum. The variance of each uncertainty is larger than for the ground state. The lower panel shows a single-sided spectrum. Due to the correlations of the sidebands the quantum noise is squeezed in a rotated quadrature with an angle of $\pi/4$ but anti-squeezed in the quadrature with an angle $-\pi/4$.

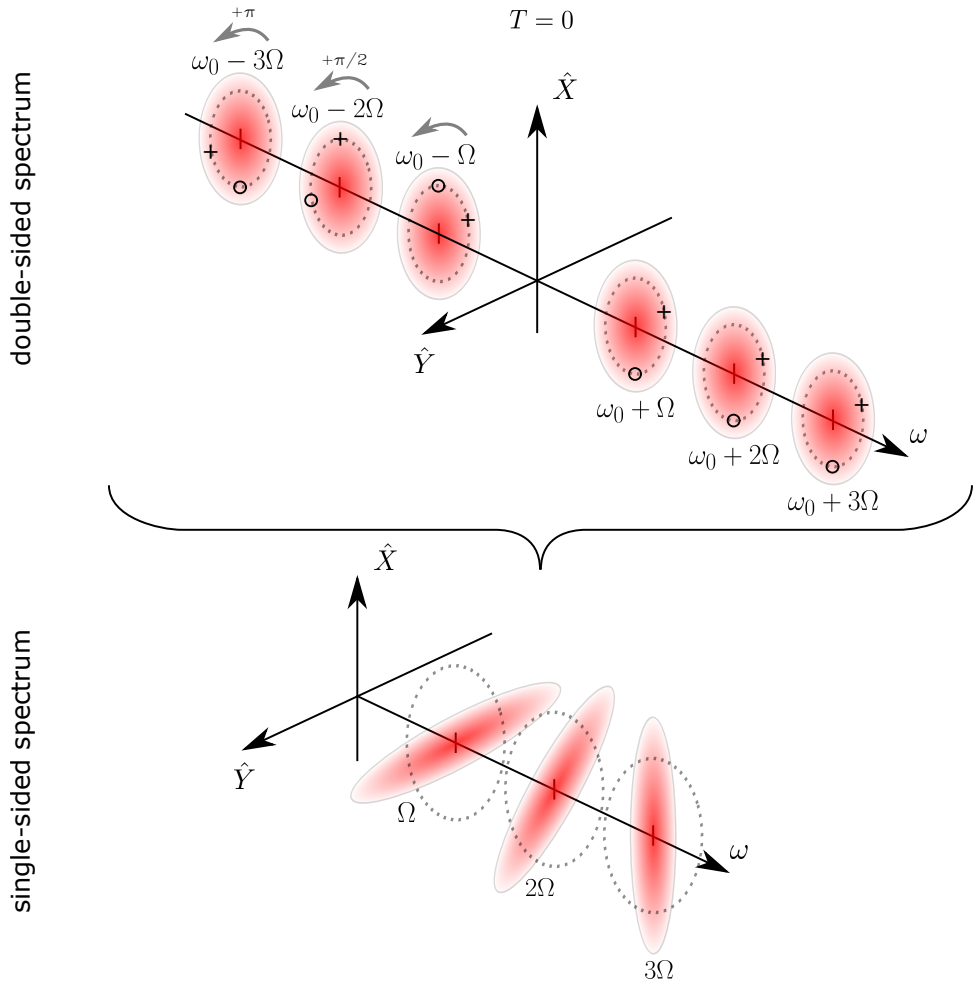

Figure 3.7: Phasor picture for an one-sided phase transition of initially amplitude squeezed states in a rotating frame for frequency ω_0. The quantum noises (red circles) are at frequencies of $\omega_0 \pm \Omega$, $\omega_0 \pm 2\Omega$ and $\omega_0 \pm 3\Omega$ and rotate clockwise (lower sidebands) and counterclockwise respectively (upper sidebands) in time. Since it is a vacuum state, no carrier is present. The correlations in the upper and lower sideband that arise from their creation in a down-conversion process are marked with the symbols + and ∘. The lower sidebands have a phase transition from 0 to π with respect to the initially amplitude squeezed state. The upper panel shows each sideband in a double-sided spectrum. The variance of each uncertainty is larger than for the ground state. The lower panel is the superposition of the field, that is the same for all times. Due to the correlations of the sidebands the quantum noise is squeezed in a rotated quadrature with a transition of the angle from 0 (amplitude squeezed) to $\pi/2$ (phase squeezed).

CHAPTER 4

Detection of gravitational waves

The first detections of gravitational waves by the LIGO and VIRGO detectors opened the era of gravitational-wave astronomy, a new window to our universe. This chapter is dedicated to an overview of laser-interferometric detectors in general and their main limitations by quantum noise. A description of a novel approach for a broadband reduction of the quantum noise in such interferometers is given.

4.1 Gravitational waves

Gravitational waves are perturbations of the spacetime and are described by Einstein's theory of general relativity [Ei16]. They are caused by accelerated masses. Although, in principle any acceleration causes gravitational waves, only astrophysical sources are considered to have masses large enough to cause measurable effects with state-of-the-art or near-future detectors. That involves events like two inspiraling black holes, two inspiraling neutron stars, inspirals of a black hole and a neutron star, super novae, or rotating neutron stars with non-perfect surfaces. Gravitational waves are transversal waves propagating with the speed of light. Their polarizations are called + and ×. These waves cause lengthening and shortening of the spacetime perpendicular to their direction of propagation. This change in length ΔL compared to a reference length L is called *strain* $h = \frac{\Delta L}{L}$ [Sa17]. The effect of these waves on freely falling test masses is shown in figure 4.1 for a gravitational wave of wavelength $\lambda = \frac{2\pi c}{\omega}$ and for the two different polarizations + (upper panel) and × (lower panel). The gravitational wave passes

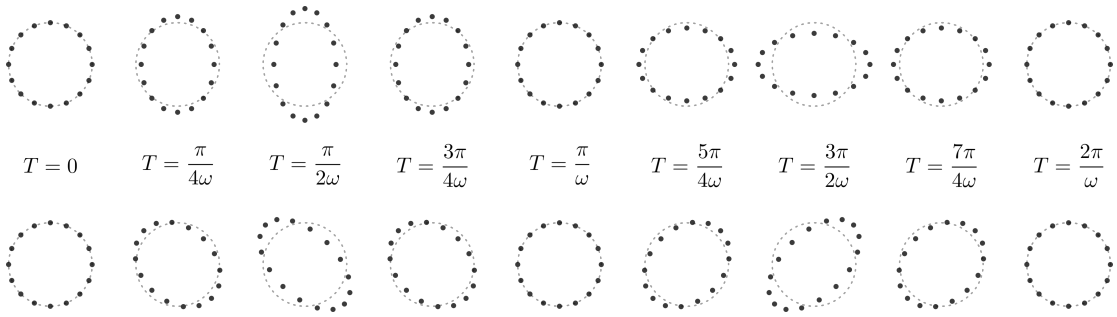

Figure 4.1: Effect of gravitational waves of frequency ω on a ring of test masses for a full oscillation period. The upper panel shows the +-polarization, the lower panel the ×-polarization. The wave passes perpendicular through the plane and causes a strain of $h = 0.33$. After a quarter period, the ring of test masses is maximally stretched along one axis and compressed along the orthogonal axis. After half a period the ring is transformed back to the initial situation. Afterwards, the test masses are stretched and compressed vice versa.

perpendicular through the plane and its strain is with $h = 0.33$ highly exaggerated for illustration compared to real events.

In 1975, Hulse and Taylor discovered the binary pulsar system PSR B1913+16 [HT75] (for which they were awarded with the Nobel prize in physics in 1993). Later studies showed the orbital period of the system to be decreasing [TW82]. This was in perfect agreement with general relativity and its prediction of gravitational waves and hence called the first *indirect* detection. In 2015 the LIGO collaboration reported on the first *direct* detection of a gravitational wave using a Michelson-like laser interferometer [Ab16a].

4.2 Interferometric detection of gravitational waves

Although there were other proposals for detecting gravitational waves (e.g. resonant antennas, called *Weber bars* [We60]), by today only laser-interferometric detection schemes reached a sensitivity that is high enough to get a sufficient signal-to-noise ratio. The most prominent representatives of these detectors are the two Advanced LIGO detectors (situated in Livingston, Louisiana and Hanford, Washington) [Aa15] and the Advanced Virgo detector (situated close to Pisa, Italy) [Ac15]. In its simplest version a Michelson-like laser interferometer consists of a laser and three mirrors, where one mirror is used as a beam splitter and the others as end mirrors of the two arms of the interferometer. Such a design is depicted in figure 4.2. The laser light gets split up by the beam splitter and send along the arms of the interferometer. The end mirrors retro-reflect the light and both beams are overlapped on the beam splitter. The resulting signal at a photo

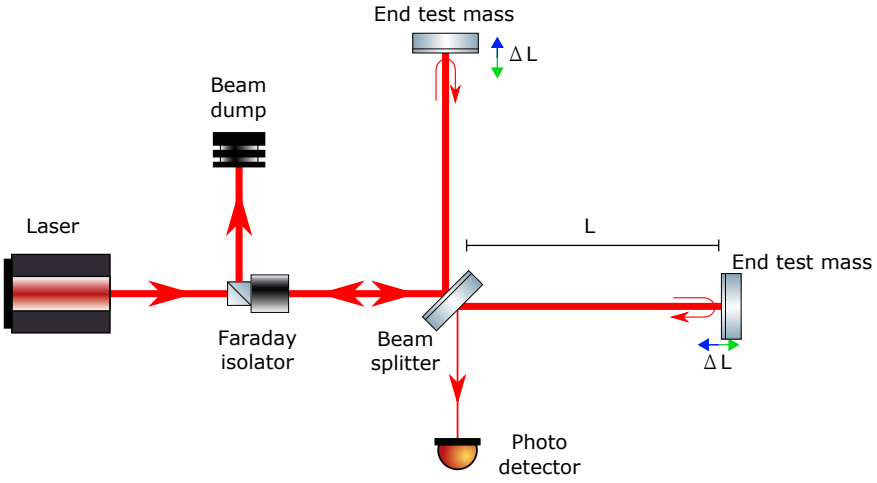

Figure 4.2: Schematic drawing of a Michelson interferometer for gravitational-wave detection. The laser is sent onto a beam splitter, travels along the interferometer arms of length L and is retro-reflected by the end mirrors. Afterwards both beams are recombined on the beam splitter. The length difference of both path are chosen such that almost no light is reflected towards the photo detector. If a differential change of the arm length of ΔL is applied (e.g. by a gravitational wave) the light picks up the phase shift of the change and the interferometer converts it to an amplitude modulation in the output port. Most of the light is reflected back towards the laser. A Faraday isolator protects the laser from this reflection.

detector is (ideally) only depending on the phase difference the light experiences during the path in the arms. A gravitational wave of the right polarization leads to an anti-symmetric change of the arm lengths. The light picks up that resulting phase shift being visible as a signal at the output port. The signal strength for gravitational wave detection is dependent on the laser power inside the interferometer and the arm length. The LIGO detectors work with an arm length of 4 km. Typically, the length difference between the arms is controlled such that there is almost no light impinging on the photo detector, referred to as *dark port condition*.

To increase the signal strength further, new techniques are needed. A *power-recycling* mirror (with reflectivity $R = 97\,\%$ in the case of Advanced LIGO) can be placed between laser and the interferometer and form a cavity with the end mirrors. Thereby, a significant increase of circulating light power can be achieved without the need for lasers of the same power. The arms can be artificially lengthened by inserting *arm cavities*. Here, a second mirror in each arm (with reflectivity $R = 98.6\,\%$ in the case of Advanced LIGO) is inserted close to the beam splitter. Together with the end mirrors, they build a cavity for each arm. This increases the time the light field can interact with a passing gravitational wave and thereby

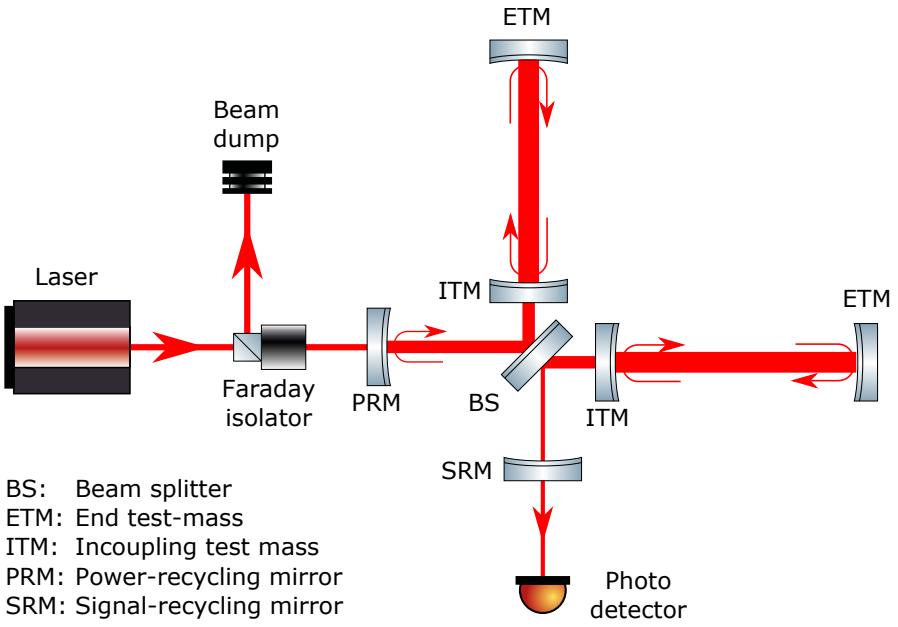

Figure 4.3: Schematic drawing of a dual-recycled Michelson interferometer using arm cavities. Additional to the Michelson-like interferometer, a power-recycling mirror in front of the beam splitter is introduced. This mirror builds a cavity with the end test-masses and reflects the light field back into the interferometer. Thereby, a higher light intensity inside the interferometer can be achieved. Inside each of the arms a cavity is formed by the incoupling test-masses and the end test-masses. This further increases the light power in the arms without increasing the power on the beam splitter that could lead to thermal lensing. The signal-recycling mirror reflects the signal from the dark port back into the interferometer which leads to a further increase of the signal.

increases the phase shift of the light field. A third technique is the implementation of a *signal-recycling* mirror in the dark port, retro-reflecting the signal back into the interferometer [Me88]. Thereby an increase in the signal can be gained. The design of such a dual-recycled interferometer with arm cavities is shown in figure 4.3.

There are many sophisticated techniques involved leading to the high sensitivity of state-of-the-art gravitational-wave detectors that can not all be mentioned here.

4.3 Limits to the detection sensitivity

The design sensitivity of Advanced LIGO is shown in figure 4.4 for a frequency range of 1 Hz to 5 kHz as presented in [Aa15]. In black, the sum of all noise contributions is shown. It is obvious, that the detector is mainly limited by quantum

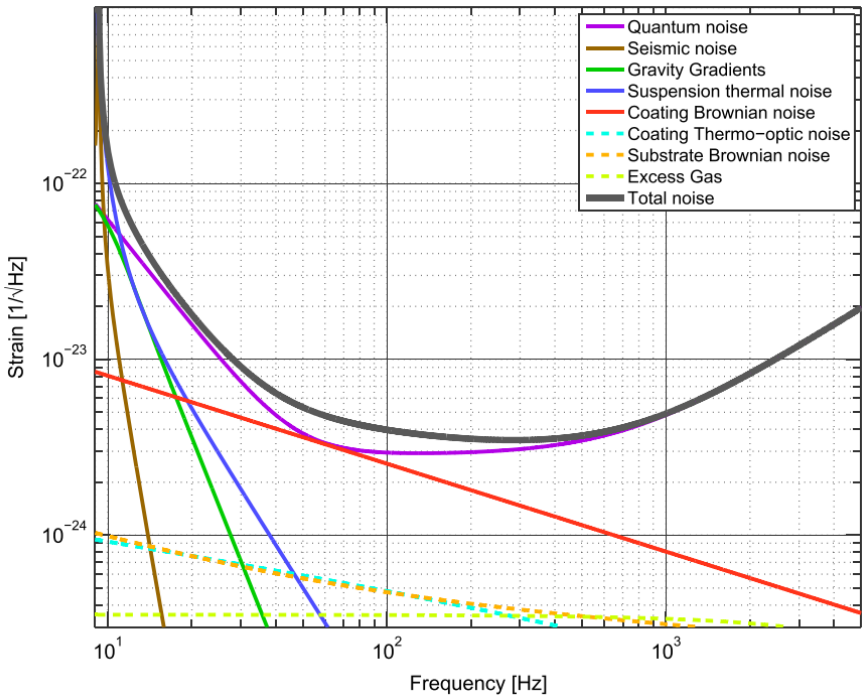

Figure 4.4: Design sensitivity for the Advanced LIGO detectors in the frequency range of 1 Hz to 5 kHz. The plot shows the total noise contributions as the black curve. The detectors are mainly limited by quantum noise shown as the purple curve. Only for low frequencies other noise components like seismic noise and suspension thermal noise play a dominant role. Coating Brownian noise has about the same influence as quantum noise in the range from 50 Hz to 80 Hz. The quantum noise is the sum of radiation pressure noise being dominant for lower frequencies and shot noise being dominant for higher frequencies. Picture taken from [Aa15].

noise shown as the purple curve. The physical background of quantum noise was given in chapter 2, but the coupling of quantum noise to an interferometer needs its own review.

A light field consists of photons that are independent with respect to each other. The average number of photons per time interval is constant, but they are not arriving at the same time at a photo detector. This is referred to as *photon shot-noise*, limiting the sensitivity of a measurement. The same property causes a second effect in a gravitational-wave detector. The radiation pressure of the light field pushes against the end mirrors and moves them a tiny bit, proportional to the light power. Since the photons arrive independently, the mirrors sense a fluctuating radiation pressure. This movement creates a back action on the light field. This noise source is referred to as *radiation-pressure noise* [Ca81]. The single-sided

power spectral densities of both displacement noises for a gravitational-wave detector read [Sa17]

$$S_x^{\mathrm{SN}} = \frac{c^2\hbar}{2\omega_0 P}\,, \tag{4.1}$$

$$S_x^{\mathrm{RPN}}(\Omega) = \frac{\hbar\omega_0 P}{c^2 m^2 \Omega^4}\,, \tag{4.2}$$

with P being the power of the laser, m the mass of the mirror and Ω the sideband frequency (above the resonance frequency of the mirror suspension). It can be seen that shot noise is inversely proportional to the laser power P, but radiation pressure noise is proportional to P. Additionally, radiation pressure noise is inversely proportional to the square of the mass of the mirrors. These displacement noises can be transferred into the strain $h = \frac{\Delta x}{L}$ of an interferometer (where the radiation pressure has to be taken into account twice) and read [Sa17]

$$h^{\mathrm{SN}} = \frac{1}{L}\sqrt{S_x^{\mathrm{SN}}} = \frac{c}{L}\sqrt{\frac{\hbar}{2\omega_0 P}}\,, \tag{4.3}$$

$$h^{\mathrm{RPN}}(\Omega) = \frac{2}{L}\sqrt{S_x^{\mathrm{RPN}}(\Omega)} = \frac{1}{mcL\Omega^2}\sqrt{2\hbar\omega_0 P}\,. \tag{4.4}$$

The sum of shot noise and radiation pressure noise is the optical readout noise and can be written as

$$h^{\mathrm{ORN}} = \sqrt{(h^{\mathrm{SN}})^2 + (h^{\mathrm{RPN}}(\Omega))^2}\,. \tag{4.5}$$

In figure 4.5 the optical readout noise for an interferometer of 4 km arm length, mirror masses of 10 kg at a wavelength of 1064 nm is shown for light powers 1 kW (blue), 10 kW (green) and 100 kW (red). Additionally, the respective shot-noise and radiation-pressure-noise contributions are given as dashed lines. A change by a factor of 10 in the optical power results in a factor of $\sqrt{10}$ reduction of the shot noise but a factor of $\sqrt{10}$ increase in radiation pressure noise. It can be seen that a region of sensitivity below a certain curve can not be reached even if the laser power can be chosen arbitrarily. This limit is referred to as the *standard quantum limit* and shown in black in figure 4.5. Mathematically, the standard quantum limit for the strain sensitivity of an interferometer can be written as

$$h^{\mathrm{SQL}}(\Omega) = \frac{2}{\Omega L}\sqrt{\frac{\hbar}{m}}\,. \tag{4.6}$$

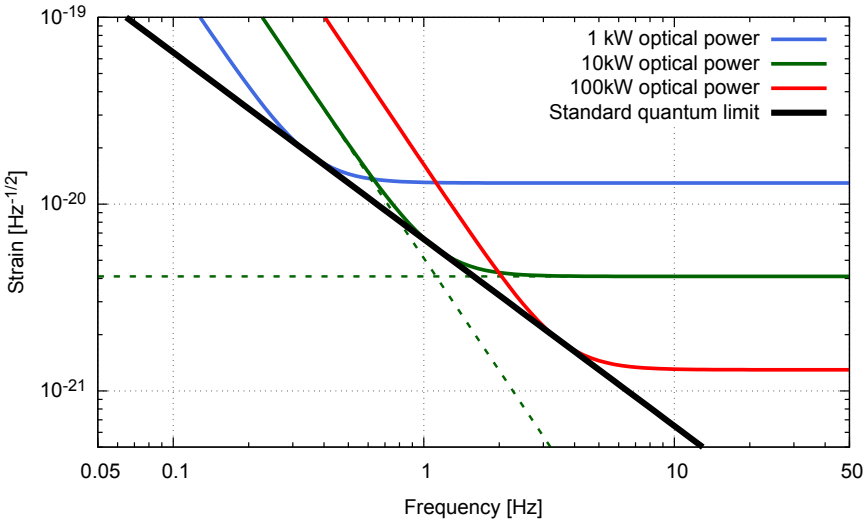

Figure 4.5: Simulation of optical readout noise for different light powers for an interferometer of 4 km arm length, mirror masses of 10 kg at a wavelength of 1064 nm. The noise is shown in the frequency range of 0.05 Hz to 50 Hz. The solid colored lines represent the sum of the radiation pressure noise (dashed lines proportional to Ω^{-2}) and the shot noise (dashed lines being frequency independent). The green line is the optical readout noise for an incident light power of 10 kW. Increasing the light power by a factor of 10 to 100 kW decreases the shot noise by a factor of $\sqrt{10}$, but the radiation pressure noise is increased by the same factor. By reducing the light power by a factor of 10 to 1 kW the shot noise is increased by a factor of $\sqrt{10}$ and the radiation pressure noise is decreased by the same factor. Taking the minimum noise depending on the light power for each frequency leads to the standard quantum limit shown as the black curve. This limit can not be overcome by only changing the light power.

4.4 Squeezed-light enhanced gravitational-wave detection

Gravitational-wave detectors are operated at the dark-port condition for the arm length difference. The incoming light of the laser is (almost perfectly) reflected back into the laser. On the other hand the vacuum noise entering through the dark port interferes with the signal inside the interferometer, leaves through the dark port and is detected on the photo detector. By replacing the incoupling vacuum state with a squeezed state of light the quantum noise contributions can be reduced [Ca81]. Thereby, the shot noise can be reduced by squeezing the phase quadrature and the radiation-pressure noise can be reduced by squeezing the amplitude quadrature. By applying amplitude- or phase-squeezed vacuum either the radiation-pressure *or* the shot noise can be reduced but the noise in the orthogonal quadrature is increased at the same time. A schematic setup of a

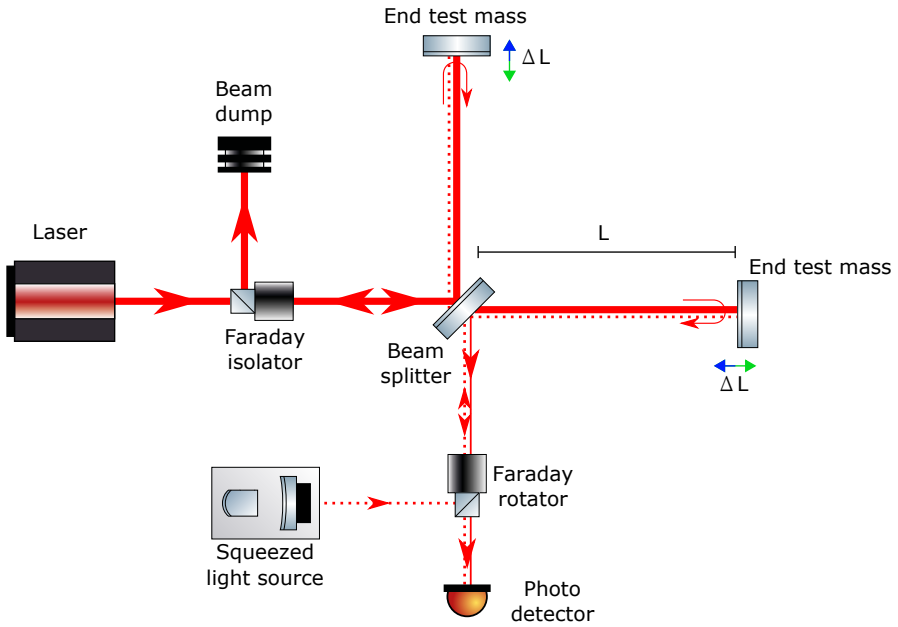

Figure 4.6: Schematic drawing of a squeezed-light-enhanced Michelson interferometer. The squeezed states of light are coupled into the interferometer via a Faraday rotator in the output port. They interfere with the signal field inside the interferometer and are sent back to the dark port. Now, the are transmitted by the Faraday rotator and sent on a photo detector. By that scheme, the vacuum noise can be reduced in one quadrature. Here, for simplification arm cavities, signal and power recycling mirrors are omitted.

squeezed-light-enhanced interferometer is given in figure 4.6, where the squeezed vacuum is coupled into the dark port via a Faraday rotator.

The effect on the strain sensitivity is shown in figure 4.7. Using only amplitude or phase squeezed states of light is equivalent to decreasing or increasing the light power by the same factor. Nevertheless, increased light power implies higher technical difficulties like thermal lensing effects due to absorption. This can be avoided by using squeezed light. The first application of squeezed light was performed in the GEO600 detector with phase-squeezed light [Gr13]. As it can be seen in figure 4.7, it is not possible to achieve sensitivities below the standard quantum limit with states having squeeze angles along the amplitude or phase quadrature operators.

Nevertheless, it is possible to achieve sensitivities below the standard quantum limit by using other squeeze angles. E.g. a squeeze angle of 45° introduces correlations of the amplitude and phase quadrature in the output ports. Thereby, a sensitivity below the standard quantum limit is possible within a small frequency band. This is possible because the calculations for the standard quantum limit assumed uncorrelated noise in both quadratures.

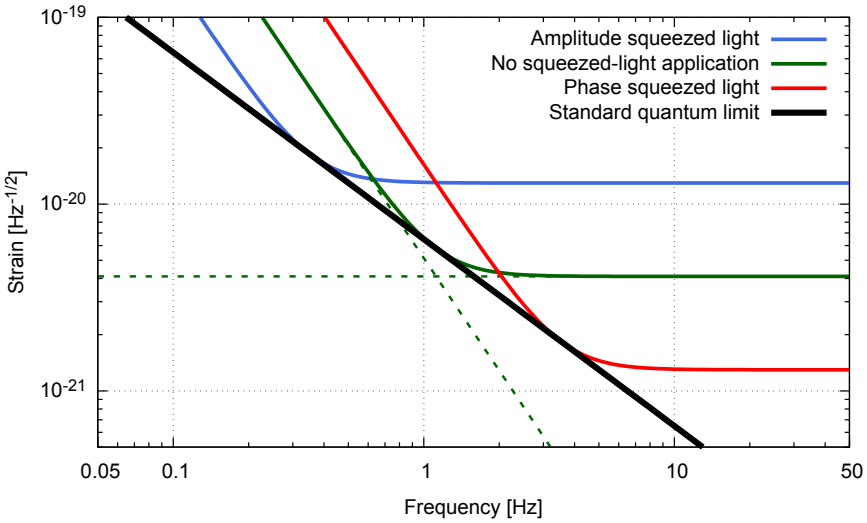

Figure 4.7: Effect of squeezed light on the strain sensitivity of a Michelson interferometer. The simulation of optical readout noise is done for an optical power of 10 kW in an interferometer of 4 km arm length, mirror masses of 10 kg at a wavelength of 1064 nm. The noise is shown in the frequency range of 0.05 Hz to 50 Hz. The green curve is the initial setup with no squeezed light application. The red curve simulates a 10 dB phase squeezed state reducing the shot noise by a factor of $\sqrt{10}$, whereas the radiation pressure noise is increased by the same factor. The blue curve simulates a 10 dB amplitude squeezed state reducing the radiation pressure noise by a factor $\sqrt{10}$ but increasing the shot noise by the same amount. The application of phase (or amplitude) squeezed states has the same effect as increasing (or decreasing) the optical power. Therefore, by using only phase or amplitude squeezed light it is impossible to reach sensitivities below the standard quantum limit.

So far, only frequency-independent angles of the squeezed states were investigated. From the previous examples it is obvious that for every detection frequency Ω a perfect squeeze angle $\phi(\Omega)$ can be defined. This is described by [Ki01]

$$\phi(\Omega) = \frac{1}{2}\,\mathrm{arccot}\left(\frac{4I_0\omega_0}{mL^2\Omega^2(\Omega^2+\gamma^2)}\right), \tag{4.7}$$

where I_0 is the input laser power, ω_0 the laser frequency, m the end mirror mass, L the length of the arm cavities and γ the bandwidth of the arm cavities. Instead of injecting a frequency-independent squeezed state it can be replaced by a modified state, where the optimal squeeze angle for every frequency is chosen. This is called frequency-dependent squeezing and is also shown in chapter 3.4 in the phasor picture. The squeezed vacuum via parametric down-conversion is produced frequency-independently and acquires a frequency-dependent phase shift

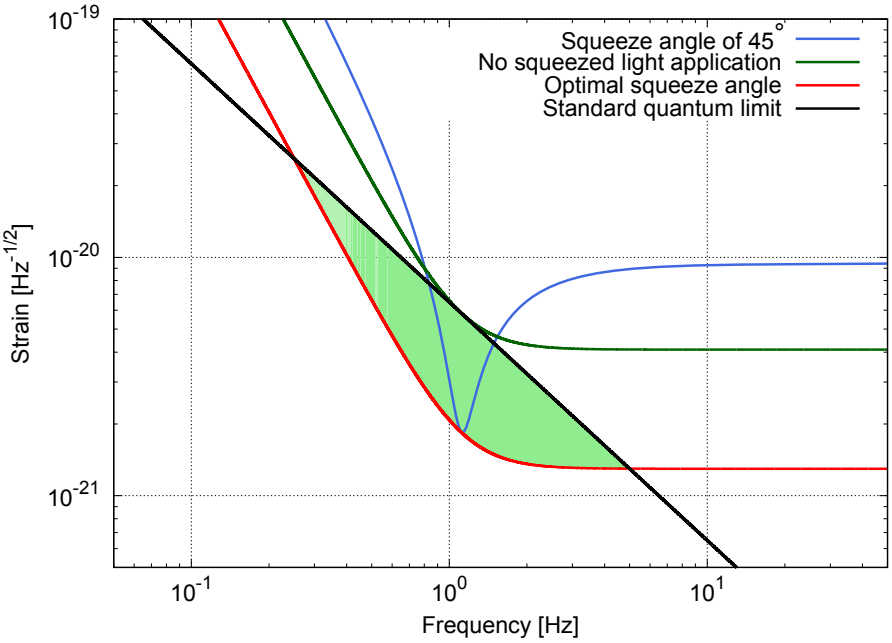

Figure 4.8: Effect of squeezed light at 45° (blue trace) and optimized, frequency-dependent squeeze angles (red trace) on the strain sensitivity of a Michelson interferometer. The simulation of optical readout noise is done for an optical power of 10 kW in an interferometer of 4 km arm length, mirror masses of 10 kg at a wavelength of 1064 nm. The noise is shown in the frequency range of 0.05 Hz to 50 Hz. For comparison, the initial setup with no squeezed light application is shown (green trace). The 45° rotated squeezed angle can improve the sensitivity compared to no squeezed light application in a small frequency band even below the standard quantum limit. For other frequencies the noise in increased. The optimized squeezed angle promises a broadband improvement in sensitivity by applying the perfect angle for every frequency. The sensitivity is below the standard quantum limit in a broad range (green area).

by reflecting the squeezed vacuum off cavities that have an optimal bandwidth and detuning [Ki01]. Then, the frequency-dependent squeezed state is injected through the dark port of the interferometer as in the frequency-independent case. Both the effects on the sensitivity of squeezed states at 45° and the optimal frequency-dependent squeeze angle are shown in figure 4.8. It is visible that for a certain bandwidth a sensitivity below the standard quantum limit can be reached.

However, frequency-dependent squeezed states are not easily produced. Kimble et al. proposed two detuned cavities off which the squeezed states are reflected to achieve the optimal squeeze angle for all frequencies [Ki01]. Later, Khalili proposed one cavity being suitable [Kh10]. A possible setup for frequency-dependent squeezed states in gravitational-wave detection (as proposed by Kimble et al.) is

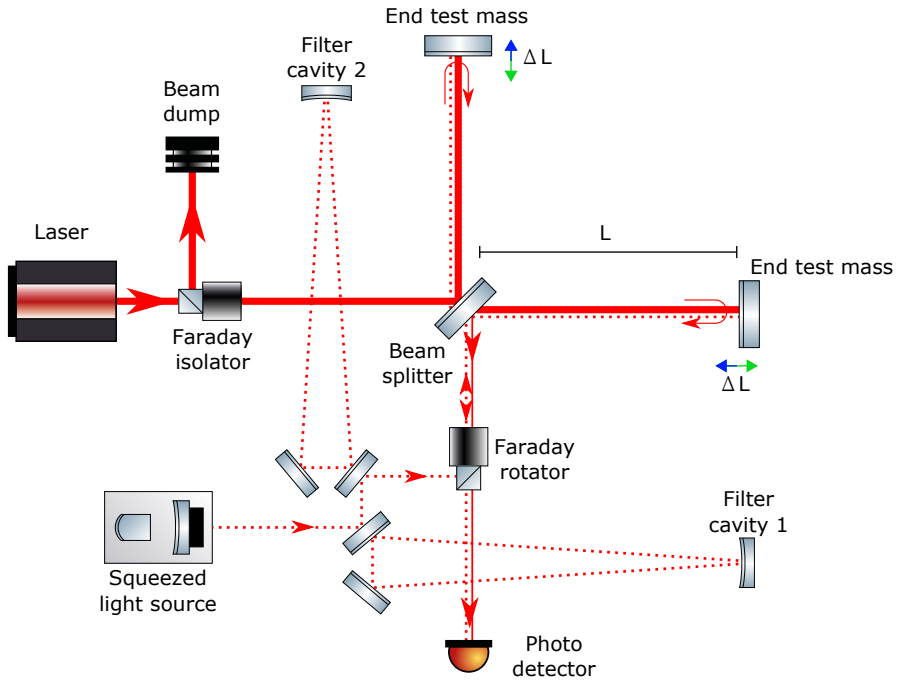

Figure 4.9: Schematic drawing of a frequency-dependent squeezed-light-enhanced Michelson interferometer. The squeezed states are reflected off two detuned filter cavities to achieve an optimal frequency-dependent squeeze angle. Afterwards, the squeezed states are coupled into the Michelson interferometer as shown before.

shown in figure 4.9. Since squeezed states strongly suffer from optical losses, the round trips in the cavity need to be minimized to avoid losses inside the coatings, but the required bandwidth has to be in the order of the detection bandwidth. This leads to filter cavities that have length in the order of 100 m [Ca16, LIGO18]. Building, maintaining and controlling them is a high technical effort and cost-intensive.

4.5 Proposal for using conditional squeezing in gravitational-wave detectors

In 2017 Ma et al. [Ma17] proposed a different scheme to achieve a broadband noise reduction below the standard quantum limit. This proposal does not require additional filter cavities to rotate the squeeze angle, but uses the signal-recycling cavity of the interferometer to perform a suitable phase transition. In conventional schemes, squeezed states were produced with a center frequency that equals the interferometer carrier frequency ω_0. They are generated by the parametric down-conversion process being pumped by a bright field at the frequency $2\omega_0$ and pro-

ducing frequency-independent squeezed states. The proposal exploits frequency-shifted squeezed light, where the pump frequency is shifted to $2\omega_0 + \Delta - \delta$, with Δ being the free spectral range of the interferometer cavity and δ an additional detuning. Thereby, sidebands at the frequencies ω_0 (lower sideband) and $\omega_0 + \Delta - \delta$ (upper sideband) are created. They are fed into the dark port of the interferometer. The lower sideband is resonant for the interferometer but the upper sideband is off-resonant. The upper sideband acquires a frequency-dependent phase shift with respect to the lower sideband depending on the detuning δ due to the reflection off the cavity. By setting the detuning an optimal phase rotation can be achieved. Both sidebands leave the interferometer through the signal port and are separated by output mode cleaners. They are sent on homodyne detectors and overlapped with local oscillators of their center frequencies ω_0 and $\omega_0 + \Delta - \delta$, respectively. The measurement at the lower sideband frequency resolves the signal produced by the gravitational wave detector and can be conditionally improved by the subtraction of the upper sideband's noise information.

In more detail the measurements at the upper and lower center frequencies are resolved at sideband frequencies Ω that lie in the detection band of a few 100 Hz. Thereby, the sidebands at frequencies $\omega_0 + \Omega$ and $\omega_0 + \Delta - \delta - \Omega$ are correlated as well as the sidebands at frequencies $\omega_0 - \Omega$ and $\omega_0 + \Delta - \delta + \Omega$. The conditioning is applied by subtracting the measured noise of the correlated sidebands.

Due to the detection of each sideband with its own local oscillator the effective squeeze factor is reduced compared to the direct detection with one local oscillator. The improvement is given by $\log(\cosh(2r))/2$. This reduction is referred to as *3 dB-penalty* since it reduces strongly squeezed states by 3 dB. Weakly squeezed states are affected less. Nevertheless, the possibility of avoiding the operation and installation of long filter cavities as proposed by Kimble et al. can be seen as the higher advantage compared to the disadvantage of the 3 dB-penalty.

The setup proposed by Ma et al. is depicted in figure 4.10.

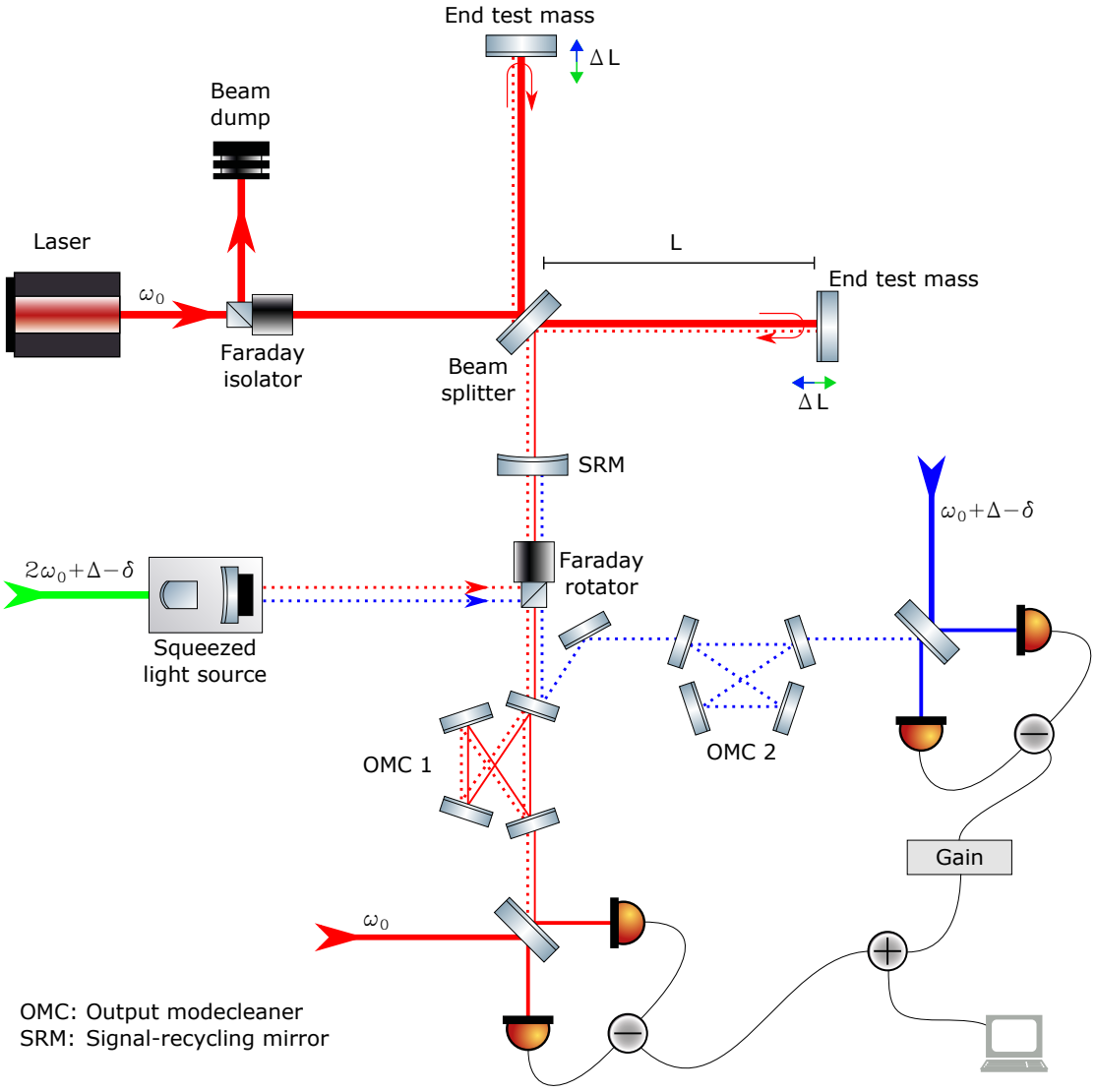

Figure 4.10: Schematic drawing of a frequency-dependent squeezed-light-enhanced Michelson interferometer by exploiting Einstein-Podolsky-Rosen entanglement and conditioned measurements. The squeezed states are produced detuned to the cavity-carrier light. A lower sideband is resonant for the cavity, while the entangled, upper sideband is off-resonant. The reflected field is separated into a part around the lower sidebands (containing the gravitational-wave signal) and a part around the upper sidebands. The measurements at the lower sidebands can be conditioned on measurements at the upper sidebands. By setting the detuning, an optimal phase rotation can be achieved.

CHAPTER 5

Experimental methods

This chapter is dedicated to the description of experimental techniques implemented in the optical setups used during this work.

5.1 Pound-Drever-Hall locking scheme

Holding optical cavities on resonance is essential for operating setups that include several cavities. The cavity length can be varied slightly by including piezoelectric elements in the design that shift one mirror of the cavity in the range of the optical wavelength. Though, a signal to stabilize a cavity is not easily generated. Detecting the reflected (or transmitted) intensity and minimizing (or maximizing) the signal in a control loop is not possible, since the resonance peak is symmetric and the control loop can not distinguish between the cavity becoming longer or shorter. The Pound-Drever-Hall locking scheme (as described in [Bl01]) uses a phase modulation of frequency Ω on the incident light field (e.g. created by an electro-optic modulator). Thereby, for small modulation indices three light fields are generated, the carrier field and a lower and an upper sideband. Due to the different frequencies the sidebands achieve different phase shifts upon reflection off the cavity compared to the carrier field. The reflected light is sent onto a photo detector and the resulting signal is demodulated with an electronic local oscillator at the frequency Ω with an appropriate phase. This process creates signals around DC and 2Ω. The latter is cut off with a low-pass filter. The other part shows a zero crossing exactly at the resonance of the cavity. Hence it contains an information whether the cavity is too long or too short and can serve as an error signal. This signal is typically sent through a proportional-integral-derivative

controller for a frequency-dependent shaping. Additionally, error signals with zero crossings are created for the resonances of the sidebands. The cavity can also be held on resonance for these sidebands. The sign of the zero crossings changes for the sidebands with respect to the sign of the zero crossing for the carrier field.

5.2 Generation of bright fields at sideband frequencies

In the experiments bright light fields (of $P_{\text{opt}} \approx 10\,\text{mW}$) at sideband frequencies of $f \approx \pm 30\,\text{MHz}$ with respect to the laser frequency needed to be available. These sidebands can be imprinted as a strong phase modulation on the laser field by using an electro-optic modulator which is driven by a sinusoidal modulated voltage at the desired sideband frequency. I used a signal out of a self-built frequency generator and additionally amplified it by two commercially available *TB-45* amplifiers by Mini-Circuits. The resulting power of the signal that was sent to the electro-optic modulator was $P_{\text{sig}} \approx 30\,\text{dBm}$ and the modulator was additionally resonant for the signal frequency. The phase-modulated light was sent onto a first triangular cavity. A part of the reflected light was sent onto a photo detector. The photo detector signal was demodulated by an electronic local oscillator to generate an error signal for locking the cavity on resonance according to the Pound-Drever-Hall locking scheme. This error signal can be used to lock the cavity on either the carrier light field or one of the sidebands. In the experiment the lower sideband was chosen. Thereby, this sideband was transmitted through the cavity while the carrier field and the upper sideband were reflected. The reflected fields were sent onto a second triangular cavity. The reflected field was detected by a second photo detector to lock the cavity on resonance for the upper sideband. The upper sideband was transmitted and the carrier field was reflected. By this scheme, all three light fields can be separated and accessed individually. A schematic setup is shown in figure 5.1. The exact sideband frequency was easily adjustable at the frequency generator.

Another scheme to generate bright sidebands is the application of acousto-optic modulators. Thereby, the fields acquire a spatial separation and no cavity is needed to separate the sidebands. Disadvantageous in this scheme is the dependence of the angle of the generated sidebands on the modulation frequency. This does not allow to fine tune the modulation frequency without the need of readjusting the beams. Therefore, this scheme was not chosen in this experiment.

5.3 Balanced homodyne detection

The description of balanced homodyne detection is based on the textbooks [GK05, SZ97]. For characterizing squeezed states of light, access to all possible quadratures is needed. With one photo detector it is possible to measure squeezed states only in the amplitude quadrature. The photo current of one photo diode is proportional to the number of photons hitting the diode and hence to the photon number operator,

$$\hat{i}(t) \propto \hat{n}(t) = \hat{a}^\dagger(t)\hat{a}(t)\,. \tag{5.1}$$

The annihilation and creation operators can be rewritten as

$$\hat{a} = \langle\hat{a}\rangle + \delta\hat{a} = \alpha + \delta\hat{a}\,, \tag{5.2}$$

$$\hat{a}^\dagger = \left\langle\hat{a}^\dagger\right\rangle + \delta\hat{a}^\dagger = \alpha^* + \delta\hat{a}^\dagger\,, \tag{5.3}$$

where they are described by an expectation value (the coherent amplitude α) and the fluctuations of the operators. By inserting these expressions for the annihilation and creation operators into equation (5.1) and assuming a real amplitude $\alpha = \alpha^*$ it yields

$$\hat{i}(t) \propto (\alpha^* + \delta\hat{a}^\dagger)(\alpha + \delta\hat{a}) \tag{5.4}$$

$$= |\alpha|^2 + \alpha\left(\delta\hat{a}^\dagger + \delta\hat{a}\right) + \delta\hat{a}^\dagger\delta\hat{a} \tag{5.5}$$

$$\approx |\alpha|^2 + \alpha\delta\hat{X}\,. \tag{5.6}$$

The term with the product of fluctuations was approximated to be negligible. The definition of the amplitude operator from equation (2.4) was used. This illustrates, that one photo diode only senses the amplitude quadrature. Information about the phase quadrature can only be gained by an interferometric measurement. For this, the signal field is overlapped with a bright field, usually referred to as *local oscillator*, on a 50/50 beam splitter. This setup is depicted in figure 5.2. The phase difference between the signal field and the local oscillator is described by φ. The output fields read

$$\hat{a}_1 = \frac{1}{\sqrt{2}}\left(\hat{a}_{\mathrm{Sig}} + \hat{a}_{\mathrm{LO}}\mathrm{e}^{\mathrm{i}\varphi}\right)\,, \tag{5.7}$$

$$\hat{a}_2 = \frac{1}{\sqrt{2}}\left(\hat{a}_{\mathrm{Sig}} - \hat{a}_{\mathrm{LO}}\mathrm{e}^{\mathrm{i}\varphi}\right)\,. \tag{5.8}$$

This leads to photo currents being proportional to

$$\hat{i}_1 \propto \hat{a}_1^\dagger\hat{a}_1 = \frac{1}{2}\left(\hat{a}_{\mathrm{Sig}}^\dagger + \hat{a}_{\mathrm{LO}}^\dagger\mathrm{e}^{-\mathrm{i}\varphi}\right)\left(\hat{a}_{\mathrm{Sig}} + \hat{a}_{\mathrm{LO}}\mathrm{e}^{\mathrm{i}\varphi}\right)\,, \tag{5.9}$$

$$\hat{i}_2 \propto \hat{a}_2^\dagger\hat{a}_2 = \frac{1}{2}\left(\hat{a}_{\mathrm{Sig}}^\dagger - \hat{a}_{\mathrm{LO}}^\dagger\mathrm{e}^{-\mathrm{i}\varphi}\right)\left(\hat{a}_{\mathrm{Sig}} - \hat{a}_{\mathrm{LO}}\mathrm{e}^{\mathrm{i}\varphi}\right)\,. \tag{5.10}$$

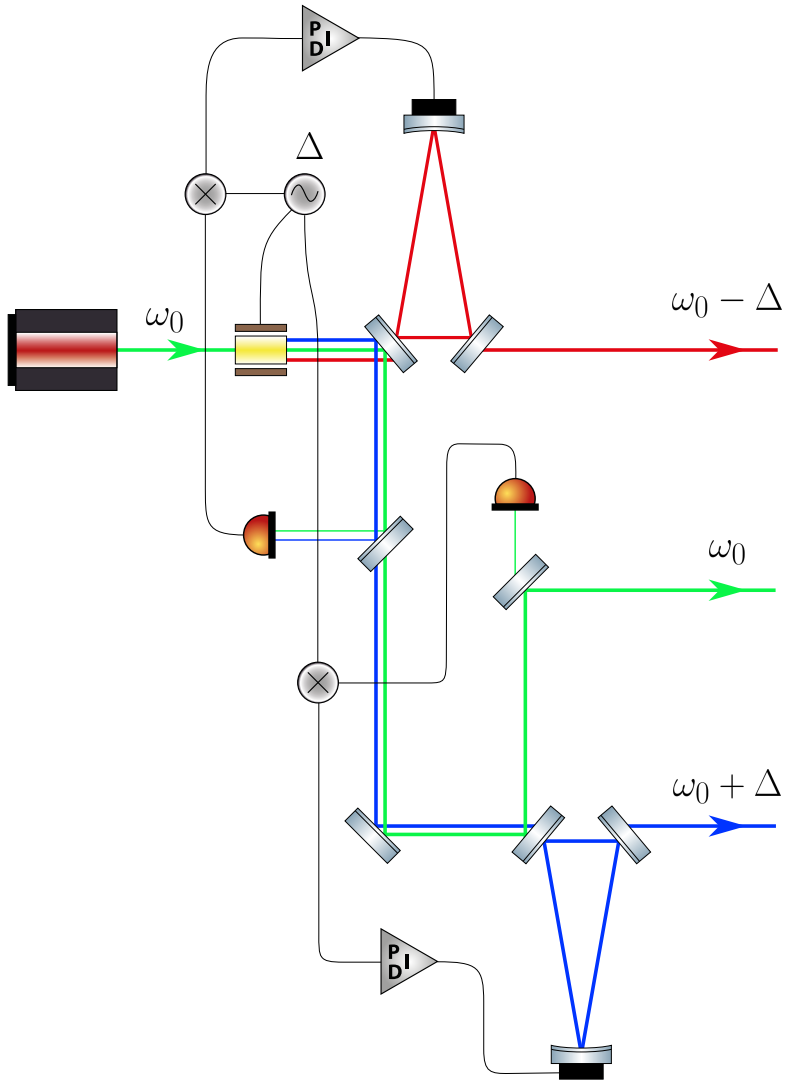

Figure 5.1: Schematic setup of the generation of bright upper and lower sidebands. The sidebands were generated by a phase modulation in a electro-optic modulator with a modulation frequency of $\frac{\Delta}{2\pi} \approx \pm 30\,\mathrm{MHz}$. To achieve a high modulation depth, the sinusoidal electronic signal to the modulator was amplified by two *TB-45* amplifiers to a power of $P \approx 30\,\mathrm{dBm}$. A ring mode cleaner cavity being resonant for the lower sideband extracted this sideband. The other two fields were sent on another modecleaner being resonant for the upper sideband. Both cavities were locked with the Pound-Drever-Hall locking technique. This scheme allowed to separate and access all three sidebands and easily adjust the modulation frequency.

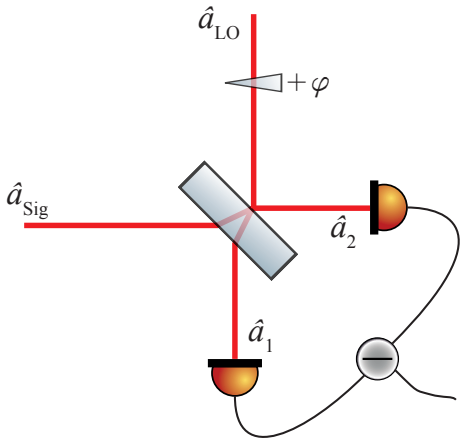

Figure 5.2: Schematic setup of balanced homodyne detection. The signal field $\hat{a}_{\mathrm{Sig}}$ from the left and the local oscillator $\hat{a}_{\mathrm{LO}}$ from the top are overlapped on a balanced beam splitter. The phase φ between both beams can be changed via a phase shifter in one path (here in the local oscillator path). The outgoing fields are detected each on a photo diode and the photo currents are subtracted from each other.

The outputs of the beam splitter are both detected on photo diodes and the resulting photo currents are subtracted from each other. The difference of the photo currents reads

$$\hat{i}_- = \hat{i}_1 - \hat{i}_2 \propto \hat{a}^\dagger_{\mathrm{Sig}}\hat{a}_{\mathrm{LO}}\mathrm{e}^{\mathrm{i}\varphi} + \hat{a}_{\mathrm{Sig}}\hat{a}^\dagger_{\mathrm{LO}}\mathrm{e}^{-\mathrm{i}\varphi}\,. \tag{5.11}$$

When the operators are again rewritten as in equations (5.2) and (5.3), higher order fluctuations are omitted, the identity of $\mathrm{e}^{\mathrm{i}\varphi} + \mathrm{e}^{-\mathrm{i}\varphi} = 2\cos\varphi$ is used and the assumption of real amplitudes $\alpha_{\mathrm{Sig}} = \alpha^*_{\mathrm{Sig}}$ and $\alpha_{\mathrm{LO}} = \alpha^*_{\mathrm{LO}}$ (the complex phase is completely described by the phase φ) is made, the difference current reads

$$\hat{i}_- \propto 2\alpha_{\mathrm{LO}}\alpha_{\mathrm{Sig}}\cos(\varphi) + \alpha_{\mathrm{LO}}\left(\delta\hat{a}^\dagger_{\mathrm{Sig}}\mathrm{e}^{\mathrm{i}\varphi} + \delta\hat{a}_{\mathrm{Sig}}\mathrm{e}^{-\mathrm{i}\varphi}\right) + \alpha_{\mathrm{Sig}}\left(\delta\hat{a}^\dagger_{\mathrm{Sig}}\mathrm{e}^{\mathrm{i}\varphi} + \delta\hat{a}_{\mathrm{Sig}}\mathrm{e}^{-\mathrm{i}\varphi}\right)\,, \tag{5.12}$$

and with equation (2.9)

$$\hat{i}_- \propto 2\alpha_{\mathrm{LO}}\alpha_{\mathrm{Sig}}\cos(\varphi) + \alpha_{\mathrm{LO}}\hat{X}_{\mathrm{Sig},\varphi} + \alpha_{\mathrm{Sig}}\hat{X}_{\mathrm{LO},-\varphi} \tag{5.13}$$

$$\approx 2\alpha_{\mathrm{LO}}\alpha_{\mathrm{Sig}}\cos(\varphi) + \alpha_{\mathrm{LO}}\hat{X}_{\mathrm{Sig},\varphi}\,. \tag{5.14}$$

The term $\alpha_{\mathrm{Sig}}\hat{X}_{\mathrm{LO},-\varphi}$ can be neglected for two reasons. On the one hand the coherent amplitude of the local oscillator is much larger then of the signal field

$\alpha_{\mathrm{LO}} \gg \alpha_{\mathrm{Sig}}$ but at the same time the quadrature amplitude is not much smaller, so in total $\alpha_{\mathrm{LO}}\hat{X}_{\mathrm{Sig},\varphi} \gg \alpha_{\mathrm{Sig}}\hat{X}_{\mathrm{LO},-\varphi}$. On the other hand (squeezed) vacuum states have no amplitude at all $\alpha_{\mathrm{Sig}} = 0$, which then even leads to a vanishing first term.

All in all, the balanced homodyne detection scheme allows to measure the quadrature operator $\hat{X}_\varphi$ of the signal field. By changing the relative phase between signal and local oscillator field any quadrature operator of the signal field can be read out.

Experimentally, the phase shift is achieved by mirrors mounted on piezoelectric elements. For this detection scheme it is very important to maintain a good spatial-mode, polarization and frequency overlap between the signal and local oscillator field. In a typical squeezing experiment the frequency is determined by the laser and the polarization is easily controllable. The spacial mode overlap can be achieved by matching both input fields from a point behind the beam splitter onto a reference cavity. Thereby, an overlap of both spatial modes on the beam splitter is achieved.

5.4 Squeezed-vacuum generation

As mentioned in chapter 2.8 squeezed states of light can be created via higher-order susceptibilities of media. The first realization of squeezed state was achieved by Slusher et al. using a four-wave-mixing process in sodium atoms in 1985 [Sl85]. The most powerful resource for creating strongly squeezed vacuum states of light is the parametric down-conversion in crystals with sufficiently high $\chi^{(2)}$ parameters [Co84]. To observe high squeeze factors, this process needs to be enhanced by a cavity, the optical parametric amplifier, for both the pump field and the fundamental field. Thereby, the effective pump power interacting with the crystal can be increased by a high factor without the need of producing such high laser powers. By having a cavity additionally for the squeezed field the down-conversion process into other modes then the fundamental mode is suppressed. This setup is operated below its oscillation threshold. In the crystal, the pump and fundamental field overlap. To achieve the best overlap all modes need to have a perfect phase relation over the whole crystal. Otherwise a created field (at the fundamental frequency) at one point in the crystal interferes destructively with another created field at other points. The length for which the generated field at the fundamental wavelength interferes still constructively with itself is called coherence length $l_{\mathrm{c}} = \frac{c}{4\omega_1(n(\omega_1)-n(\omega_2))}$. A perfect phase relation is reached when the refractive indices for both the pump and fundamental wavelength are the same, although typically $n(\omega_1) \neq n(\omega_2)$ for $\omega_1 \neq \omega_2$. In the case of equal refractive indices, the difference of all wave vectors vanishes

$$|\vec{k}_{\omega_+} + \vec{k}_{\omega_-} - \vec{k}_{2\omega}| = 0\,. \tag{5.15}$$

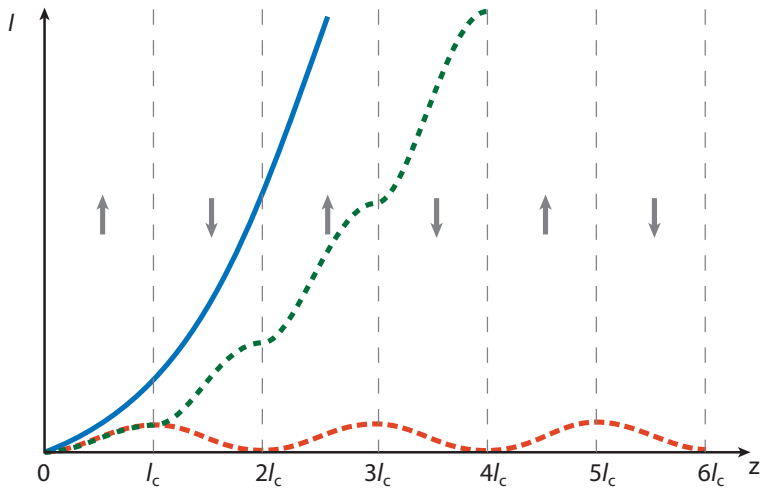

Figure 5.3: Different phase matching conditions in nonlinear materials in a second-harmonic generation process. The blue curve depicts the intensity of the second harmonic for perfect phase matching temperatures. An continuously increasing intensity can be observed. The red curve shows the intensity of the generated field in the case of no phase matching. The intensity can only reach a low value and is afterwards converted back to the fundamental field. The green line shows the case of quasi-phase matching using periodically poled crystals. The poling is indicated by the vertical black dashed lines and the different signs of the poling by the arrows. In the case of quasi-phase matching light is converted to the second harmonic up to a maximum from where it would be converted back without a periodically poling. But since the poling changes, the conversion starts to rise again on every change of the poling. Picture taken from [St13].

This is called *phase matching*. For squeezed light generation birefringent materials are utilized [St13]. By having the second harmonic and fundamental field in orthogonal polarizations (*Type I phase matching*) and using different temperature dependencies for the two wavelength $\frac{\mathrm{d}n(\omega)}{\mathrm{d}T}$ phase matching ($n(\omega) = n(2\omega)$) is possible. In figure 5.3 the intensity of the generated field for a second-harmonic process is shown in dependence of the interaction length with the crystal for different phase matching conditions. Perfect phase matching is depicted as the blue curve. As a comparison the intensity in case of no phase matching is shown in red. Disadvantageous is the reliance of materials having equal refractive indices at temperatures that are sufficiently low to be used for cavities.

Another possibility is using *quasi phase matching*. This scheme does not rely on equal refractive indices. The crystal is divided into zones of the length l_c along the

propagation axis of the light fields. After each zone, the sign of the susceptibility is flipped. Here, the wave vectors drift apart during the propagation in one zone, but sensing the flipped susceptibility in the next zone, the difference in the wave vectors vanishes again. This leads to a slower increase of the intensity of the generated field as shown in figure 5.3 as the green dashed line, but is experimentally easier controllable. The sign of the susceptibility is depicted by the arrows. A heating of the crystal is still necessary to compensate for a non-perfect length of the zones in the crystal but this temperature can be chosen much lower.

5.5 Spectra of squeezed states from cavity-enhanced generation

The spectrum of the squeezed light is reduced in a cavity-enhanced generation due to the linewidth of the cavity. The spectra of noise power in the squeezed and anti-squeezed quadratures for a given cavity with full-width-half-maximum linewidth γ and oscillation threshold P_{thres} is described by [Fu15]

$$S_{\text{sqz/asqz}}(P,f) = 1 \mp \eta \frac{4\sqrt{P/P_{\text{thres}}}}{\left(1 \pm \sqrt{P/P_{\text{thres}}}\right)^2 + 4\left(\frac{2\pi f}{\gamma}\right)^2}\,, \tag{5.16}$$

where P is the pump power, f the sideband frequency and η the total detection efficiency.

5.6 Bichromatic homodyne detection of squeezed states

The local oscillator of the homodyne detection was so far considered to be monochromatic at the center frequency ω_0 of the squeezed field. The homodyne detector measures at a sideband frequency of Ω around the frequency ω_0 of the local oscillator, so in total two sidebands are measured. The monochromatic local oscillator can be replaced by a field consisting of two frequencies $\omega_0 \pm \Delta$. Each detection with a local oscillator measures an upper and lower sideband at the frequency of Ω around its center frequency. In total, four sidebands are measured at frequencies $\omega_0 - \Delta \pm \Omega$ and $\omega_0 + \Delta \pm \Omega$. Having a squeezed field centered at ω_0 the sidebands at $\omega_0 - \Delta + \Omega$ and $\omega_0 + \Delta - \Omega$ are entangled as well as the sidebands at $\omega_0 - \Delta - \Omega$ and $\omega_0 + \Delta + \Omega$. In a bichromatic measurement both entangled pairs are resolved at the sideband frequency Ω in a single-sided spectrum. The resulting noise spectra of the squeezed and anti-squeezed quadrature can be described by two detuned spectra from equation (5.16) [Xi18]

$$S_{\text{bi,sqz/asqz}}(P,f) = \frac{1}{2}\left(S_{\text{sqz/asqz}}(P,\Delta - \Omega) + S_{\text{sqz/asqz}}(P,\Delta + \Omega)\right)\,, \tag{5.17}$$

where the same detection efficiency η and optical power for both local oscillators is assumed.

CHAPTER 6

Compact source of squeezed vacuum-states at 1064 nm

In the recent years the footprints of sources of squeezed states of light became progressively smaller [Va10, Sc18a]. Compact setups allow flexible applications of squeezed states. The squeezed-light source for the gravitational-wave detector GEO600 at 1064 nm was built 2010 on a breadboard of 1.5 m^2. It was the first source of strongly squeezed states that was transported to its place of operation. In [Sc18a] a source was built on a footprint of 0.64 m^2 working at the telecommunication wavelength of 1550 nm. Here, I present a squeezed-light source that I designed and assembled on a breadboard with a footprint of $1 \times 0.8\,m^2$ working at the wavelength of 1064 nm. This size was achieved by carefully arranging standard-sized optical components in a computer-aided-design before placing them on a breadboard. I achieved a noise reduction of more then 10 dB below the vacuum noise. The source is dedicated to reduce the quantum noise in downstream experiments. Lukas Terkowski was involved in the assembly as a master student and demonstrated a first application in an opto-mechanical experiment [Te17].

6.1 Experimental setup

The schematic drawing of the source is shown in figure 6.1, divided in the parts *Light preparation*, *Second-harmonic generation*, *Squeezed-light generation*, *Balanced homodyne detection* and *Extension for coherent control lock*. The following subsections will explain these parts in more detail.

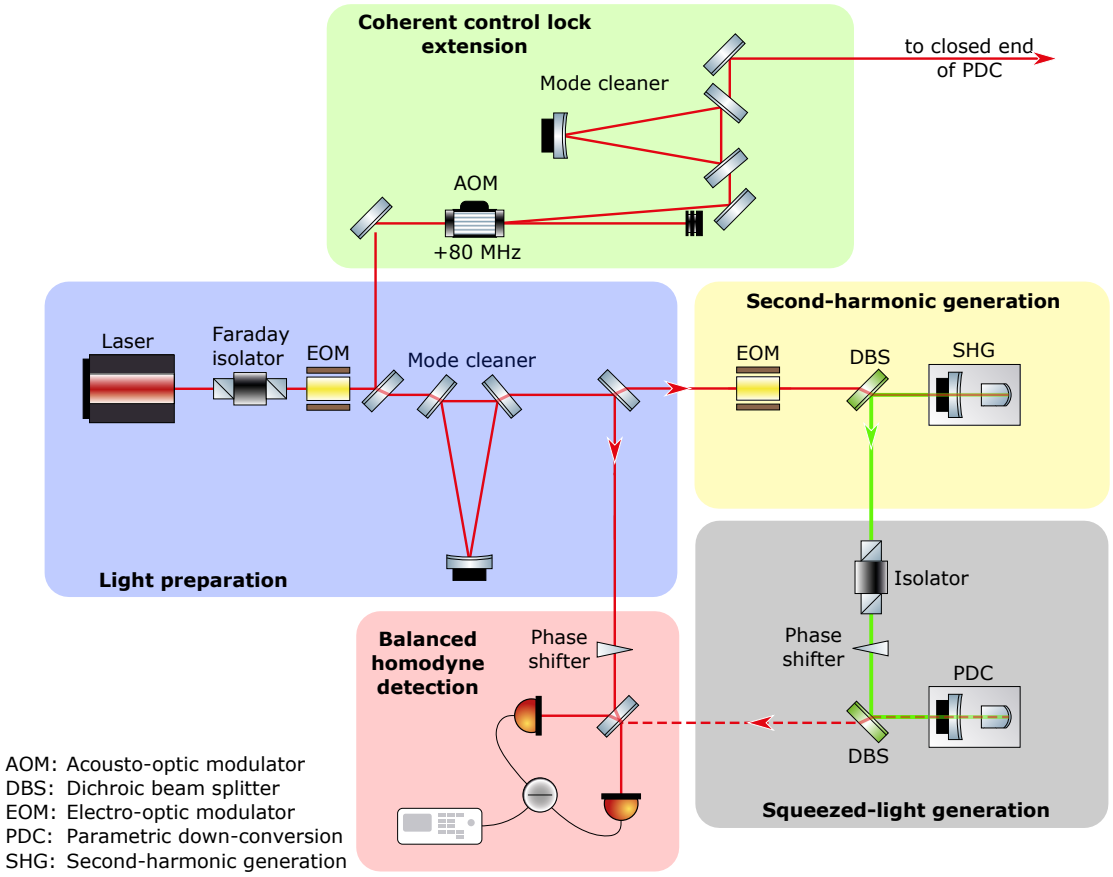

Figure 6.1: Schematic drawing of the setup for a compact source of squeezed vacuum-states of light. The setup is divided into the parts *Light preparation* (blue box), *Second-harmonic generation* (yellow box), *Squeezed-light generation* (grey box), *Balanced homodyne detection* (red box) and *Extension for coherent control lock* (green box). This overview excludes electronics and all beams that are not important for the understanding of the setup. A detailed description of these parts is given in the respective sections.

6.1.1 Laser light preparation

The coherent-light source used in this experiment was a diode-pumped Nd:YAG laser Mephisto by *Innolight* with a total output power of 2 W at the wavelength of 1064 nm. A Faraday isolator was used to prevent back-reflected light from the experiment hitting the laser and disturbing its mode of operation. A quarter-wave plate and half-wave plate were used to achieve optimal transmission through the isolator. Although the spatial mode of the laser was already very good, the light was sent through a filter cavity. This ensured higher order spatial modes, remaining contaminations in the orthogonal polarization and high-frequency amplitude noise on the light to be filtered out. To stabilize the cavity, the Pound-Drever-Hall

locking technique was used. Therefore, a phase modulation at the frequency of 66.4 MHz was imprinted on the light by using an electro-optic modulator. The light reflected off the ring cavity was sent to a resonant photodetector, the resulting photocurrent was converted to a voltage and electronically demodulated with the modulation frequency. A low-pass cuts the components at twice the modulation frequency off and hence an error signal was generated. This was sent to a proportional-integral-derivative controller and the resulting feedback signal was amplified to a voltage range of 0-400 V. The signal was sent to an piezoelectric actuator being able to shift the round-trip length of the cavity in the order of the wavelength of the light. This kept the resonator on resonance. Afterwards, the light was split up by a beam splitter. One part served as the local oscillator for the balanced homodyne detection, the other as the pump for the second-harmonic generation. The setup of the light preparation is depicted in figure 6.2.

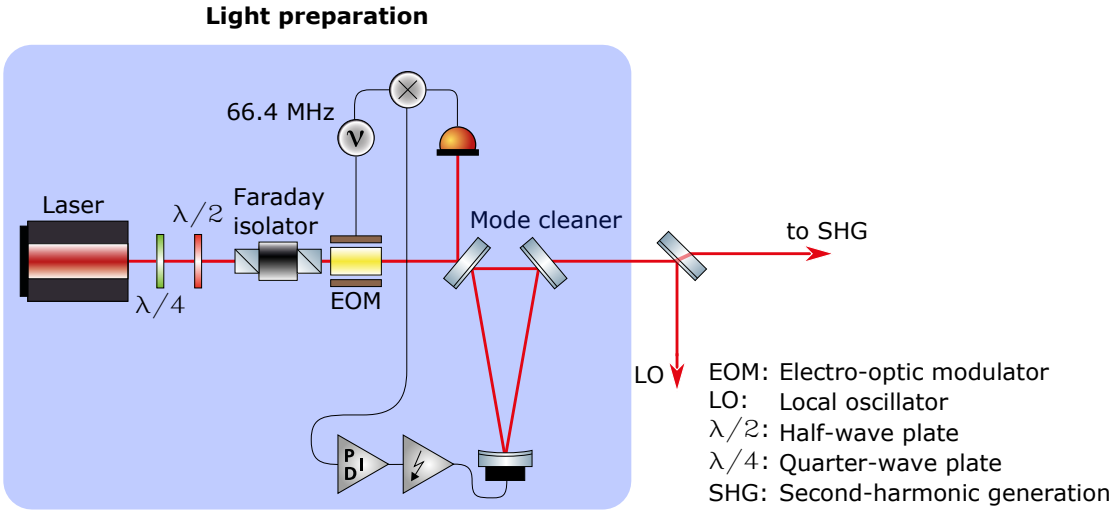

Figure 6.2: Schematic drawing of the setup of the laser light preparation stage. The light at the wavelength of 1064 nm was sent through a Faraday isolator. A phase modulation at the frequency of 66.4 MHz was imprinted by an electro-optic modulator. These sidebands were used to stabilize the mode-cleaner cavity on resonance by the Pound-Drever-Hall locking technique. Afterwards, one part of the light part served as the local oscillator for the balanced homodyne detection, the other as the pump for the second-harmonic generation.

6.1.2 Second-harmonic generation

A detailed illustration of the second-harmonic generation cavity is given in figure 6.3. The cavity consisted of a lithium niobate crystal with a magnesium-oxide-doping concentration of 7 % and with the dimensions 2 mm × 2.5 mm × 6.5 mm.

One side was curved with a radius of curvature of 12 mm. This side was highly reflective for both wavelengths ($R_{1064} > 99.96\,\%$ and $R_{532} > 99.9\,\%$) and acted as the closed end of the cavity. The crystal was mounted on two separated copper blocks. They can be heated to individual temperatures by Peltier elements being placed below the copper. Here, the larger part of the cavity was heated to a temperature to achieve a good phase-matching between the two beams at 1064 nm and 532 nm. The smaller part consisted of the closed end of the cavity. The temperature of this part was used to fine tune the propagation lengths of both fields due to different penetration depth in the coatings of the crystal. The other side of the crystal was plane and coated anti-reflectively for both wavelengths. The cavity was formed with a coupling mirror having an air gap of 22 mm to the crystal. This mirror had power reflectivities of $R_{1064} = 89\,\%$ and $R_{532} = 19\,\%$ and a radius of curvature of 25 mm on the side facing the cavity. Additionally, the side of the mirror facing the outside had a radius of curvature of 20 mm to reduce the beam divergence and avoid parasitic cavities between optical surfaces. On the outside, a piezoelectric element was placed to tune the length of the cavity in the order of the involved wavelengths. For each temperature stage two negative-temperature-coefficient resistors (*NTC833*) were placed inside the copper blocks. One of them was used to lock the temperature to a defined value using a feedback loop with the Peltier elements as actuators. The other was used to monitor the temperature. For a good conversion efficiency both temperatures were set to be around 20 kΩ or 60 °C respectively.

Following the light preparation stage, the light was sent through another electro-optic modulator where a phase modulation with the frequency of 77.8 MHz was imprinted on the light. Afterwards, the laser beam was focused into the second-harmonic generation cavity, where a bright light field at 532 nm was generated. The residual light at 1064 nm and 532 nm leaking out of the cavity through the highly-reflective side was separated with a dichroic beam splitter. The light at 1064 nm was sent onto a resonant photo detector and demodulated with an electronic local oscillator. The resulting error signal was fed back via a proportional-integral-derivative controller and an amplifier for high voltage onto a piezoelectric element to keep the cavity length on resonance. The leaking light at 532 nm was detected by a photo detector to find the optimal conversion temperatures of the crystal. The main part of the converted light is leaving the cavity through the coupling mirror. It is separated from the light at 1064 nm by a dichroic beam-splitter. A part of the phase modulation at 78.7 MHz on the pump field is also up-converted to 532 nm and can be used further for the lock of the parametric down-conversion cavity. The setup for the second-harmonic generation is depicted in figure 6.4.

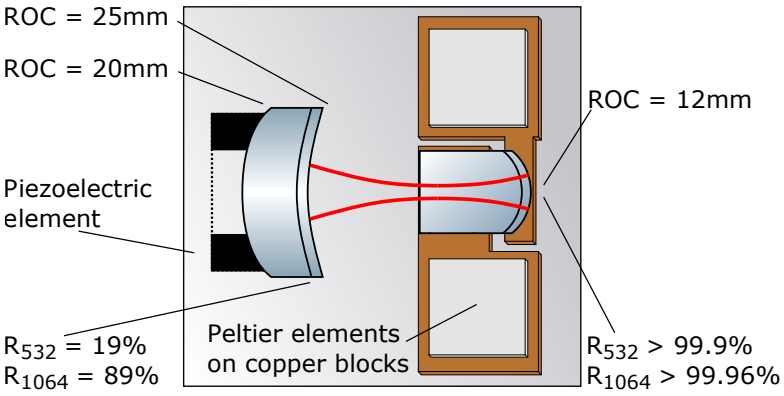

Figure 6.3: Detailed schematic drawing of the second-harmonic generation cavity. The cavity consisted of a lithium niobate crystal with a magnesium-oxide-doping concentration of 7 % and with the dimensions 2 mm×2.5 mm×6.5 mm. One side of the crystal was curved with a radius of curvature of 12 mm. This side was highly reflective for both the fundamental and second-harmonic wavelength ($R_{1064} > 99.96\,\%$ and $R_{532} > 99.9\,\%$) and acted as the closed end of the cavity. The other side of the crystal was plane and coated anti-reflectively for both wavelengths. The cavity is formed with the coupling mirror that is placed with an air gap of 22 mm in front of the plane side of the crystal. It had power reflectivities of $R_{1064} = 89\,\%$ and $R_{532} = 19\,\%$ and a radius of curvature of 25 mm on the side facing the cavity. Additionally, the side of the mirror facing the outside had a radius of curvature of 20 mm to reduce the beam divergence and avoid parasitic cavities. On the outside of the mirror a piezoelectric element was placed to change the length of the cavity in the order of the involved wavelengths. The crystal was placed on two copper blocks that can be heated individually by two Peltier elements. The temperature of the main part of the crystal was used to achieve a good phase-matching between both beams at 1064 nm and 532 nm. The other part consisted of the back side of the crystal and its temperature was used to achieve a fine tuning for the propagation lengths of both beams due to different penetration depth in the coatings of the crystal. For each block two negative-temperature-coefficient elements (*NTC833*) were used. One element was used to lock the temperature of the crystal to a desired value and the other was used to monitor this temperature.

6.1.3 Parametric down-conversion

The design of the cavity for the parametric down-conversion process was exactly the same as the one of the second-harmonic generation. The only difference was the crystal material being periodically-poled potassium titanyl phosphate (PPKTP). The crystal had dimensions of 1 mm × 2 mm × 5 mm and a radius of curvature of $r = 10$ mm on the closed end. This side was coated highly-reflective for

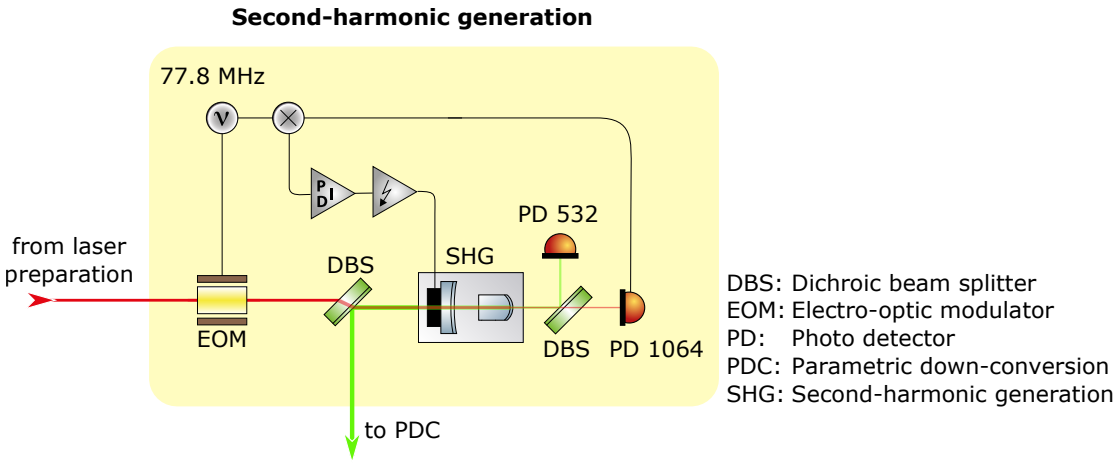

Figure 6.4: Schematic drawing of the setup of the second-harmonic generation stage. In an electro-optic modulator, a phase modulation at the frequency of 78.7 MHz was imprinted to the light at 1064 nm. Afterwards, the light was sent into a cavity consisting of a lithium niobate crystal. Here, a bright field a 532 nm was generated. This field was separated from the fundamental field by a dichroic beam-splitter. The cavity was locked on resonance by the Pound-Drever-Hall locking technique using a resonant photo detector in transmission of the cavity. The error signal was fed back to a piezoelectric electric element on the coupling mirror to change the length of the cavity. A photo detector for light at 532 nm was used to monitor the generated light power and fine tune the temperature settings for phase matching.

both wavelengths. The plane side is anti-reflectively coated for both wavelengths. The coupling mirror had power reflectivities of $R_{1064} = 89\,\%$ and $R_{532} = 97.5\,\%$ and was placed in front of the plane side of the crystal with an air gap of 22.5 mm. The cavity design is depicted in figure 6.5.

The beam at 532 nm was sent through a Faraday isolator to avoid back-reflections into the second-harmonic generation cavity. Afterwards, it was reflected off a phase-shifter mirror. This design was implemented to allow a later extension of the experiment by installing a lock of the pump phase, see also chapter 6.1.5. Then, it was sent into the down-conversion cavity. The reflected light off that cavity was detected on a resonant photo detector in the output of the Faraday isolator. The photo current was transformed into a voltage, demodulated with an electronic local oscillator at 78.7 MHz and low-pass filtered. The resulting error signal was sent to a proportional-integral-derivative controller, amplified to high voltage and sent back onto the piezoelectric element inside the cavity to keep it on resonance. Here, the up-converted phase modulation at 78.7 MHz on the pump beam was used. The squeezed light was leaving the cavity through the coupling mirror and was separated from the pump beam by a dichroic beam-splitter. Insert-

ing a control beam at 1064 nm from the closed end into the cavity helped to find the best phase-matching temperature and to perform beam alignment and mode matchings along the squeezed-light path. This was necessary since the squeezed vacuum has no coherent excitation. Via a flip mirror a single sideband field with an offset of +80 MHz with respect to the laser light frequency can be injected into the cavity. This was part of the coherent control extension described in chapter 6.1.5. Simultaneous resonance for both wavelengths was monitored by overlapping the resonance peaks of the pump beam at 532 nm (on the photo detector used for locking the cavity) and the control beam at 1064 nm (on one of the photo diodes of the homodyne detector) by tuning the temperatures of the crystal. The setup of the parametric down-conversion stage is depicted in figure 6.6.

6.1.4 Balanced homodyne detection

The local oscillator and the squeezed light were superimposed on a 50/50 beam splitter. In the path of the local oscillator, a piezoelectric phase-shifter mirror was placed to adjust the relative phase between the two fields. The outgoing fields of the beam splitter were focused on photo diodes. They were placed on a printed circuit board such that the resulting photo currents were subtracted directly. The resulting current was converted to a voltage, high-pass filtered and recorded with a spectrum analyzer. To achieve a good mode matching between the local oscillator and the squeezed light, a flip mirror was installed in one of the arms behind the beam splitter. It guided the fields to a ring cavity. Both fields were mode matched onto this diagnostic mode cleaner and were thereby well overlapped on the beam splitter.

6.1.5 Possible extension to coherent control lock

The setup includes the possible extension to a coherent control lock of the phase of the squeezed light to the local oscillator as described in [Va08]. This enables a phase lock without the need of a coherent field at the laser frequency. Such a design is essential to achieve phase-locking of squeezed states at low sideband frequencies. Without adding this technique technical noise due a bright control field at the laser frequency disturbs the measurements. For the lock, a single-sideband generation is already included in the setup. A tap-off before the first mode cleaner of the laser light at frequency ω_0 is sent through an acousto-optic modulator that is driven with an electronic sinusoidal signal at 80 MHz. This creates a bright field at $\omega_0 + 80\,\mathrm{MHz}$ leaving the modulator under an angle with respect to the fundamental light. The single sideband passes pin holes to block the fundamental field and is finally filtered by a ring mode cleaner cavity as described in chapter 6.1.1. It is locked in the same way by using the Pound-Drever-Hall technique utilizing the phase modulation of 66.4 MHz. The sideband is fed into

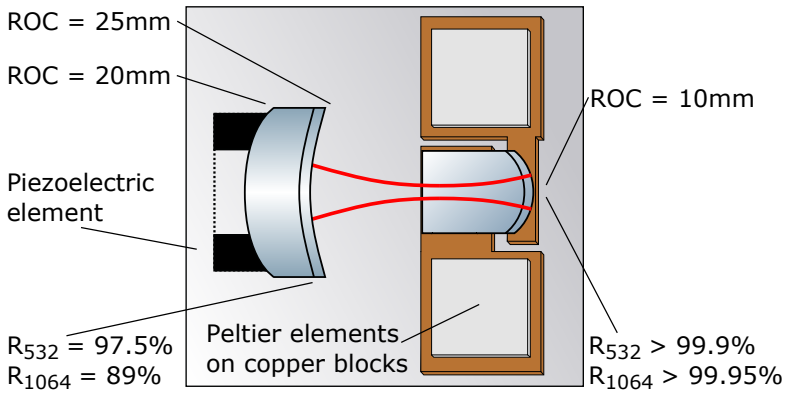

Figure 6.5: Detailed schematic drawing of the parametric down-conversion cavity. The cavity consisted of a periodically-poled potassium titanyl phosphate crystal with the dimensions of 1 mm × 2 mm × 5 mm. One side of the crystal was curved with a radius of curvature of 10 mm. This side was highly reflective for both the fundamental and second-harmonic wavelength ($R_{1064} > 99.95\,\%$ and $R_{532} > 99.9\,\%$) and acted as the closed end of the cavity. The other side of the crystal was plane and coated anti-reflectively for both wavelengths. The cavity was formed with the coupling mirror placed in front of the plane side of the crystal with an air gap of 22.5 mm. It had power reflectivities of $R_{1064} = 89\,\%$ and $R_{532} = 97.5\,\%$ and a radius of curvature of 25 mm on the side facing the cavity. Additionally, the side of the mirror facing the outside had a radius of curvature of 20 mm to reduce the beam divergence and avoid parasitic cavities. On the outside of the mirror a piezoelectric element was placed to change the length of the cavity in the order of the involved wavelength. The crystal was placed on two copper blocks that can be heated individually by two Peltier elements. The temperature of the main part of the crystal was used to achieve a good phase matching between both beams at 1064 nm and 532 nm. The other part consisted of the back side of the crystal and its temperatures was used to achieve a fine tuning for the propagation length of both beams due to different penetration depth in the coatings of the crystal. For each block two-negative-temperature coefficient elements were used. One element was used to lock the temperature of the crystal to a desired temperature and the other was used to monitor this temperature.

the parametric down-conversion cavity through the back side via a flip mirror. The down-conversion process generates a sideband at $\omega_0 - 80\,\mathrm{MHz}$ that can be used to lock the phase of the pump field to the sideband and afterwards the phase of the local oscillator to the squeezed field. Details can be found in [Va08]. The lock is only a possible extension to the setup and was not completed.

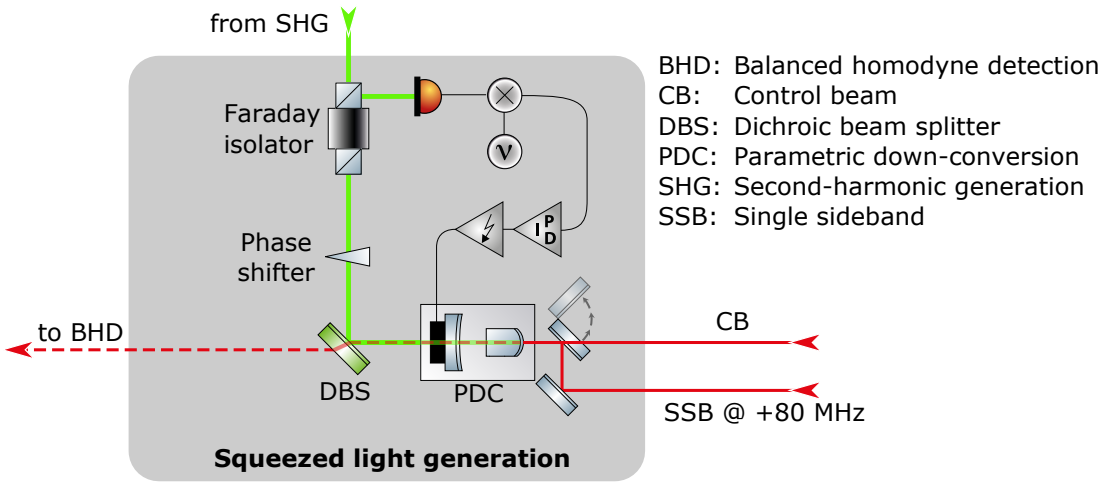

Figure 6.6: Schematic drawing of the setup of the parametric down-conversion stage. The pump beam at 532 nm was sent through a Faraday rotator to avoid back-reflections to the second-harmonic generation cavity. A phase-shifter mirror can be used to control the phase of the pump beam. Then, the light was sent into the parametric down-conversion cavity. The reflected light was sent to a photodetector in reflection of the Faraday isolator and the up-converted phase modulation from the second-harmonic stage at a frequency of 78.7 MHz was used with the Pound-Drever-Hall locking technique to keep the cavity on resonance. The generated squeezed light was separated from the pump beam via a dichroic beam-splitter. From the closed end of the cavity, a control beam can be sent into the cavity to find the best phase matching temperature and for beam alignment along the path of the squeezed field. Via a flip mirror, a single sideband with a frequency shift of +80 MHz with respect to the fundamental beam can be injected to use a coherent control lock.

6.2 Experimental results

For the generation of the light field at 532 nm, a total pump power of 350 mW at 1064 nm was sent into the second-harmonic generation cavity. The temperature of the long part of the crystal was set to 20.6 kΩ and of the shorter part to 20.2 kΩ, respectively 59.8 °C and 60.3 °C. With these settings, an output power of $\sim$ 100 mW at 532 nm was generated. The conversion efficiency of this process is $\frac{P_{\text{in}}}{P_{\text{out}}} \approx 28\,\%$. The reason for the low conversion efficiency was not further investigated since the generated optical power was high enough for the parametric down-conversion. Additionally, the output mode showed a contribution of another mode. The origin of this mode could not be determined, but had no influence on further measurements since it was suppressed by the down-conversion cavity. The mode matching of the pump field to the down-conversion cavity was 76 % and

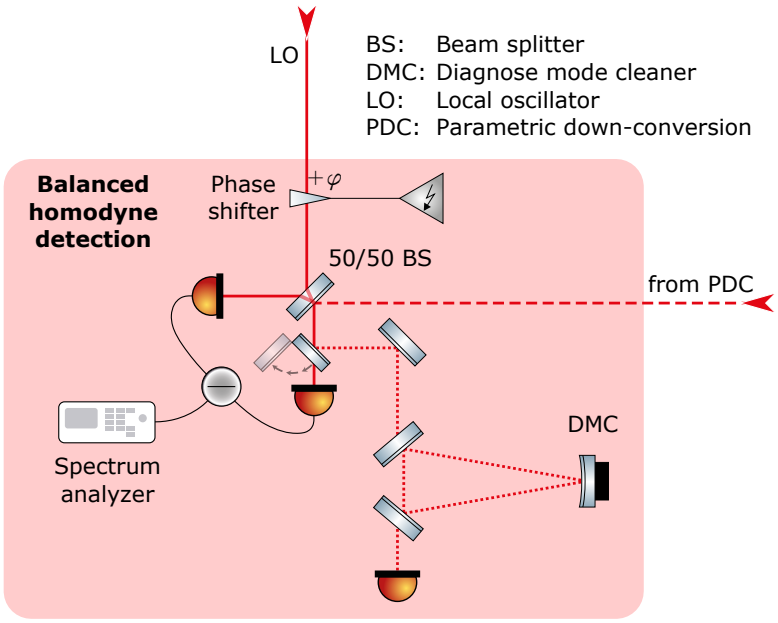

Figure 6.7: Schematic drawing of the balanced homodyne-detection stage. The local oscillator and the squeezed light field were superimposed on a balanced beam splitter. Both outcomes were detected with photo diodes. The resulting photo currents were subtracted directly on the printed circuit board and transformed into a voltage, high-pass filtered and recorded with a spectrum analyzer. In one of the arms behind the beam splitter, a flip mirror was placed to send the beams to a diagnose mode cleaner. Both the local oscillator and the squeezed field were mode matched onto this cavity to achieve a good overlap of the modes on the beam splitter.

mainly limited by the contribution of the other mode. For all measurements with this setup, the power of the pump field was measured with a power meter directly in front of the down-conversion cavity and this value was corrected by a factor of 0.76 to determine the power entering the cavity in the fundamental mode. All stated pump powers are the corrected values.

A homodyne detector with a linear response function is essential for the measurement of strongly squeezed states. The shot noise power scales linearly compared to the local oscillator power. Here, the local oscillator power was set to different values between 1 mW and 25 mW and the shot-noise power at the sideband frequency of 5 MHz scaled linearly with to the local oscillator power.

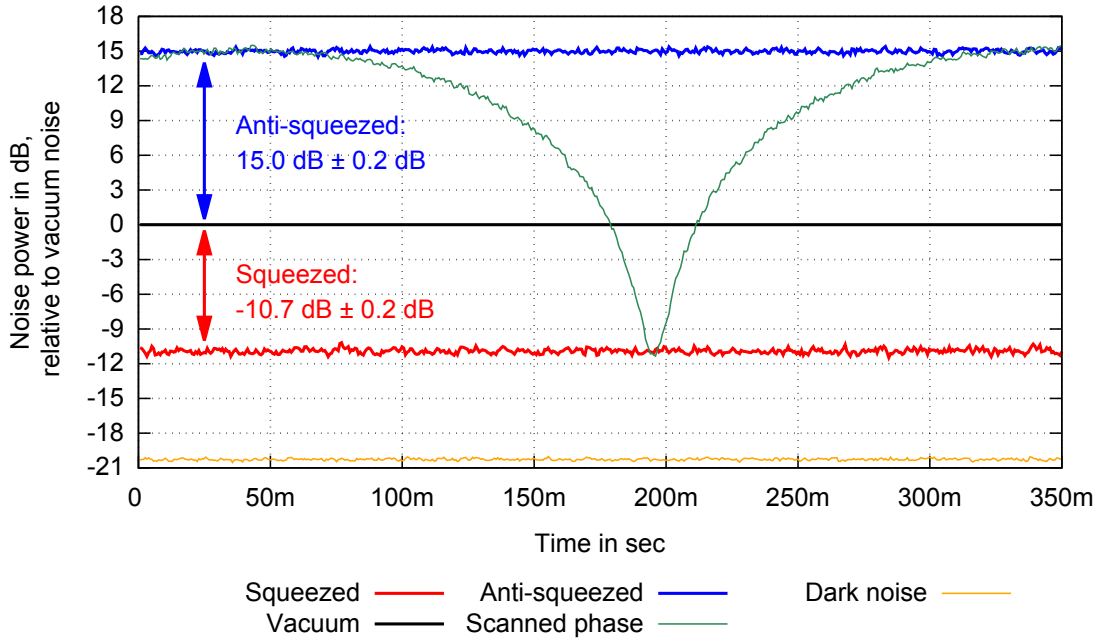

Figure 6.8: Noise power of squeezed states normalized to vacuum noise at the sideband frequency of 5 MHz. The measurements were taken with a resolution bandwidth of 300 kHz and a video bandwidth of 300 Hz. The vacuum noise power (black trace) was measured with a blocked signal path and averaged 5 times. With an open signal path, the noise power of the squeezed (red trace) and the anti-squeezed (blue) quadrature were measured The phase between the signal field and the local oscillator was adjusted manually. The vacuum noise power was subtracted of the noise power of the squeezed states. A noise reduction of 10.7 dB ± 0.2 dB below the vacuum noise was achieved. The related anti-squeezed quadrature showed an increase in noise power of 15.0 dB ± 0.2 dB above the vacuum noise. This equals a total loss of 5.7 % ± 0.5 %. A measurement of the noise power of the squeezed states with a slowly scanned readout phase (green trace) is shown for comparison. The electronic dark noise power of the detector was measured to be 20.2 dB below the vacuum noise.

6.2.1 Zero-span measurements of noise power of squeezed states at 5 MHz

A first characterization of the squeezed states produced by this setup was performed with zero-span measurements of the noise power at the sideband frequency of 5 MHz. This frequency is far above frequencies for which squeezed states are limited by technical noise but still within the bandwidth of the down-conversion cavity. A pump power of 30 mW and a local oscillator power of 22 mW were used. The phase-matching temperatures for the crystal were set to 60.9 kΩ for

the longer part and 64.5 kΩ for the shorter part, respectively 32.2 °C and 30.8 °C. The resulting measurements of the noise power of squeezed states are shown in figure 6.8, where the resolution bandwidth of the spectrum analyzer was 300 kHz and the video bandwidth was 300 Hz. The vacuum noise power (black trace) was measured with a blocked signal path and averaged 5 times. With an open signal port the noise power of the squeezed states was measured and the phase between the local oscillator and the signal field was controlled with a piezoelectric element in the local oscillator path. The vacuum noise power was subtracted of the noise power of the squeezed states. A measurement of the noise power of the squeezed states with a slowly scanned readout phase (green trace) covers all possible readout angles. The noise power of the squeezed (red trace) and anti-squeezed (blue trace) quadratures were measured by controlling the readout phase manually. Thereby, a noise reduction of 10.7 dB ± 0.2 dB below the vacuum noise was achieved. The related anti-squeezed quadrature showed an increase in noise of 15.0 dB ± 0.2 dB above the vacuum noise. This equals to a total loss of 5.7 % ± 0.5 % according to equation (2.33). After these measurements the vacuum noise power was checked again to ensure same noise levels. The electronic dark noise power of the detector (orange trace) was 20.3 dB below the vacuum noise power. By correcting the noise powers for the dark noise, a reduction of 11.2 dB ± 0.2 dB below the vacuum noise results. Principally, a loss of 5.7 % allows a reduction of quantum noise of 12.4 dB below vacuum noise. Here, the initial squeeze factor was limited by the phase matching temperatures.

6.2.2 Spectrum measurements of noise power of squeezed states

The spectrum of the noise power of squeezed states was measured in a lower frequency band between 20 kHz and 1 MHz and a higher frequency band between 2 MHz and 65 MHz. For the lower frequency band, a resolution bandwidth of 6.25 kHz and a video bandwidth of 30 Hz were used. In the higher band, a resolution bandwidth of 30 kHz and a video bandwidth of 300 Hz were used. A pump power of 30 mW and a local oscillator power of 22 mW were used. Here, no lock for the readout quadrature was available. Since a spectrum measurement takes some seconds in which the phase drifts, the measurements were taken in the MINHOLD (respectively MAXHOLD) mode of the analyzer for the squeezed (respectively the anti-squeezed) quadrature. In this mode, the analyzer saves the minimal (or maximal) value for each frequency during the measurement time. The measurement was performed for several sweeps over the frequency band with a slowly changed phase so that the optimal readout quadrature was measured for all frequencies with a high probability. The vacuum noise power was acquired with a blocked signal port in both analyzer modes. A normalization of the noise power of the squeezed quadrature was made to the vacuum noise power measured with the MINHOLD mode, for the anti-squeezed quadrature the normalization was

made to the vacuum noise power measured in the MAXHOLD mode. From these measurements, a quantitative analysis of the noise power in the squeezed and anti-squeezed quadratures is not possible with absolute certainty since the measured results are distorted. Special care needs to be taken to have a low noise on each measured trace. Nevertheless, a qualitative discussion of the presence of squeezed light for different sideband frequencies and the estimation of the linewidth of the down-conversion cavity can be made. The squeezed states were generated with a pump power of 27 mW.

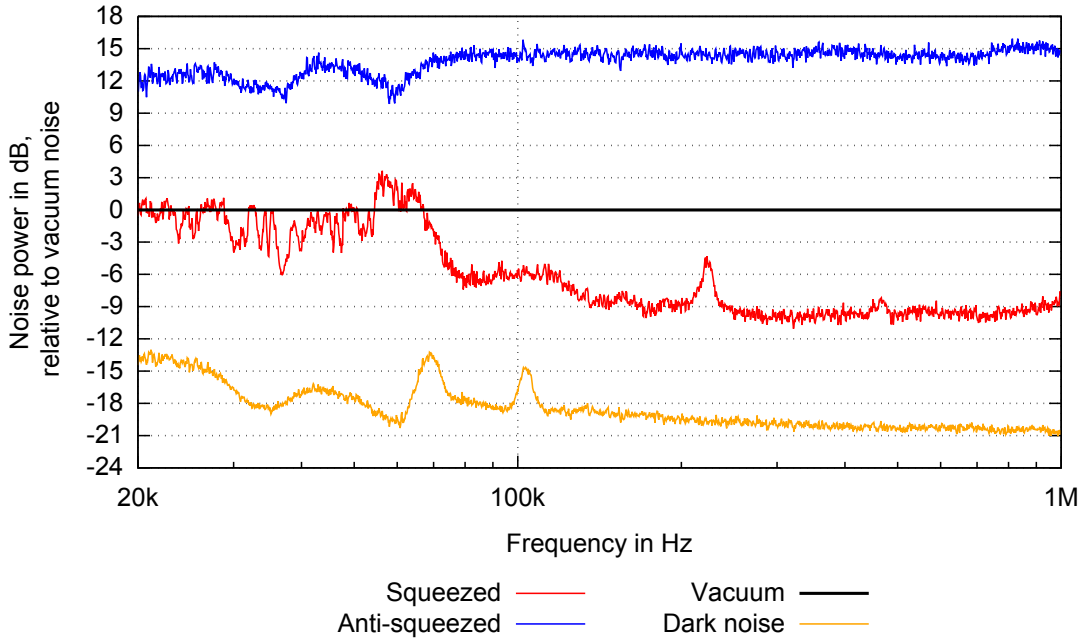

Figure 6.9: Spectra of the noise power of squeezed states normalized to vacuum noise in a frequency band between 20 kHz and 1 MHz. The measurements were taken with a resolution bandwidth of 6.25 kHz and a video bandwidth of 30 Hz. A pump power of 30 mW and a local oscillator power of 22 mW were used. Since no lock for the readout phase was available, the squeezed quadrature (red trace) was measured with the MINHOLD mode of the analyzer, the anti-squeezed quadrature (blue trace) in the MAXHOLD mode. Each measurement was taken for several sweeps of the analyzer over the frequency band with a slowly scanned phase. They were each normalized to the vacuum level (black trace) measured in the same mode. A measurement in these modes requires special care to not strongly distort the results and is referred to in the main text. A noise reduction below the vacuum noise is possible down to a frequency of 70 kHz. Below that frequency the squeezed properties were most likely masked by technical noise on the local oscillator that was not fully suppressed. The noise in the anti-squeezed quadrature was above the vacuum noise in the whole detection band. In this frequency range, the detection was not limited by the detector's electronic dark noise (orange trace). For all measurements, I performed a verification with the noise power measured in the *CLR/WRITE* mode, the mode used typically for measurements of noise power of squeezed states.

Slight adjustments of the phase-matching temperatures compared to the zero-span measurement at 5 MHz were made to compensate for less heating by pump power absorption in the crystal. For all measurements, I performed a verification

with the noise power measured in the *CLR/WRITE* mode, the mode used typically for measurements of noise power of squeezed states.

For the lower frequency band, the measurements of the noise power are shown in figure 6.9. A reduction of the noise power below the vacuum noise (red trace) was observed down to a frequency of 70 kHz. Below that frequency, the squeezed properties were most likely masked by technical noise on the local oscillator that was not fully suppressed. This might have resulted from a non-perfect splitting ratio at the homodyne detector. The noise in the anti-squeezed quadrature was above the vacuum noise in the whole detection band. The measurements were not limited by the detector's electronic dark noise (orange trace) in the given frequency range.

For the higher frequency band, the measurements of the noise power are shown in figure 6.10. A reduction of the noise in the squeezed quadrature below the vacuum noise (red trace) over the whole frequency band was achieved. The corresponding the anti-squeezed quadrature (blue trace) had a noise power above the vacuum noise for all given frequencies. A large dark-noise clearance of up to 20 dB (compared to the vacuum noise) for lower frequencies and 16 dB at the sideband frequency of 60 MHz was achieved. For higher frequencies both the squeezed and the anti-squeezed quadrature showed the influence of the finite bandwidth of the down-conversion cavity. For both quadratures, equation (5.16) with the respective sign was fitted to the measured data, where the pump threshold P_{th}, the cavity linewidth γ_{lw} and the total loss L_{tot} were the fitting parameters (blue dashed trace for the squeezed, red dashed trace for the anti-squeezed quadrature). The fit resulted in values for the pump threshold of the down-conversion cavity of $P_{\mathrm{th}} = 53\,\mathrm{mW}$ and a linewidth of $\gamma_{\mathrm{lw}} = 2\pi \cdot 98\,\mathrm{MHz}$ for the wavelength of 1064 nm.

6.2.3 Pump power dependence of the noise power of squeezed states

At the sideband frequency of 5 MHz, the noise power of the squeezed and anti-squeezed quadratures were recorded in individual measurements with different pump powers in a range from 3.5 mW to 32 mW. Each measurement of noise power was normalized to the vacuum noise (solid black trace) and the results are shown in figure 6.11 (red crosses for noise power in squeezed, blue crosses for noise power in anti-squeezed quadratures). For each measurement the vacuum noise was recorded separately and checked again after the measurement to ensure same power levels. Additionally, the temperatures of the crystal were tuned individually for every pump power due to different heating by absorption of pump light. The phase of the local oscillator was manually controlled. For both quadratures, equation (5.16) with the respective sign was fitted to the measured data (red solid trace for noise power in squeezed, blue solid trace for anti-squeezed quadrature). The pump threshold P_{th}, the cavity linewidth γ_{lw} and the total loss L_{tot} were the fitting parameters. The fit resulted in a pump threshold of $P_{\mathrm{th}} = 52\,\mathrm{mW}$, a linewidth

of $\gamma_{\mathrm{lw}} = 2\pi \cdot 102\,\mathrm{MHz}$ for the wavelength of 1064 nm and a total loss of $L_{\mathrm{tot}} = 8.7\,\%$. The linewidth and the pump threshold are in good accordance with the results from chapter 6.2.2. The detection efficiency was smaller than in the other measurements. Since the pump-power dependence was measured on a different day, there might have been a worse overlap of the squeezed light's mode and the local oscillator's mode on the beam splitter. For the pump powers between 7 mW and 17.5 mW, both measurements of noise power in the squeezed and anti-squeezed quadratures have less gain of the down-conversion process and lie above (squeezed quadrature) or below (anti-squeezed quadrature) the fitted trace. This can be explained by non-perfect temperature settings of the crystal.

6.3 Conclusion

Here, I present a source of squeezed states of light that was built on a breadboard with a footprint of 80 cm × 100 cm including a homodyne detection. The source provides squeezed states of up to $10.7\,\mathrm{dB} \pm 0.2\,\mathrm{dB}$ noise reduction below the vacuum noise at the sideband frequency of 5 MHz with a corresponding anti-squeezed quadrature with increased noise of $15\,\mathrm{dB} \pm 0.2\,\mathrm{dB}$ above vacuum noise. This equals to a total loss of $5.7\,\% \pm 0.5\,\%$. Down to a sideband frequency of 70 kHz squeezed properties were observed. For higher frequencies the influence of the linewidth of the down-conversion cavity was shown, which was measured to be $\sim 2\pi \cdot 100\,\mathrm{MHz}$. The pump threshold was measured to be 53 mW.

The low conversion efficiency and the origin of the second mode on the light field at 532 nm were not investigated here. The source can be further improved by integrating a coherent control lock of the phase of the squeezed light to the local oscillator. Preliminary steps for this lock were presented. With this integration, longer measurement times of a defined quadrature are possible. A loss of 5.7 % allows a reduction of quantum noise of 12.4 dB below vacuum noise by finding better phase matching temperatures and increasing the squeeze factor. An investigation of limiting factors such as technical noise on the local oscillator allows the measurement of squeezed properties at lower frequencies than 70 kHz. By reducing the size of optical components, especially of the modecleaner cavities and mirror holders, the size of the source can be decreased further.

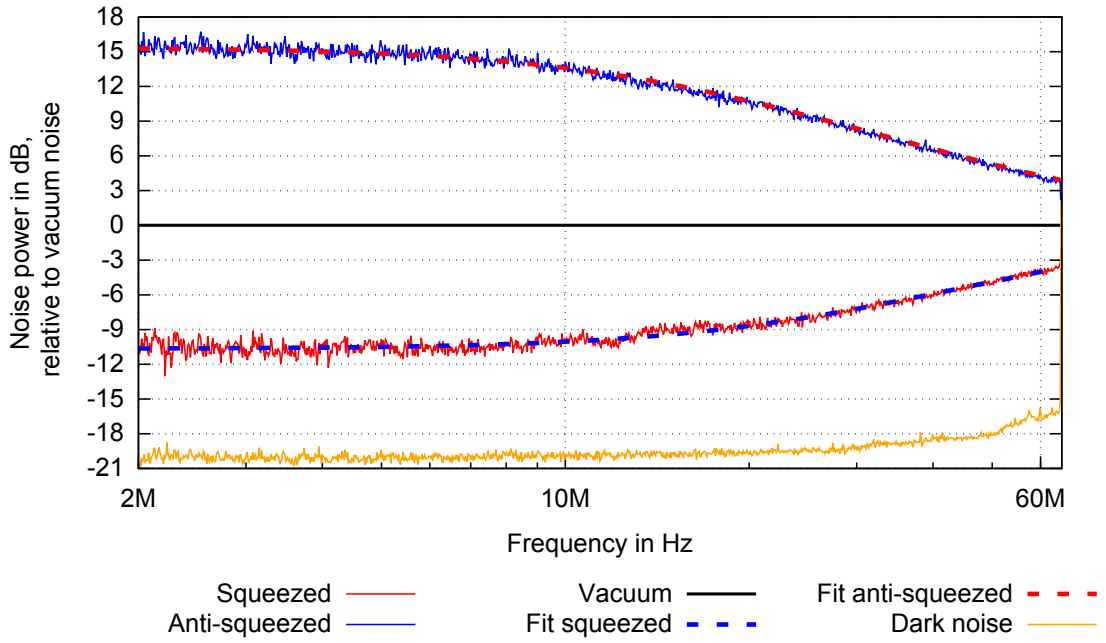

Figure 6.10: Spectra of the noise power of squeezed states normalized to vacuum noise in a frequency band between 2 MHz and 65 MHz. The measurements were taken with a resolution bandwidth of 30 kHz and a video bandwidth of 300 Hz. A pump power of 30 mW and a local oscillator power of 22 mW were used. The measurements were performed in the same detection modes (MINHOLD/MAXHOLD) as in the spectrum measurement at low frequencies. A measurement in these modes requires special care to not strongly distort the results and is referred to in the main text. The squeezed quadrature (red trace) showed a noise reduction below the vacuum noise (black trace) over the whole frequency range. The anti-squeezed quadrature (blue trace) had an increased noise above the vacuum noise for all frequencies in this detection band. For both quadratures, equation (5.16) with the respective sign was fitted to the measured data, where the pump threshold P_{th}, the cavity linewidth γ_{lw} and the total loss L_{tot} were the fitting parameters (blue dashed trace for the squeezed, red dashed trace for the anti-squeezed quadrature). The fit resulted in values for the pump threshold of the down-conversion cavity of $P_{\mathrm{th}} = 53\,\mathrm{mW}$ and a linewidth of $\gamma_{\mathrm{lw}} = 2\pi \cdot 98\,\mathrm{MHz}$ for the wavelength of 1064 nm.

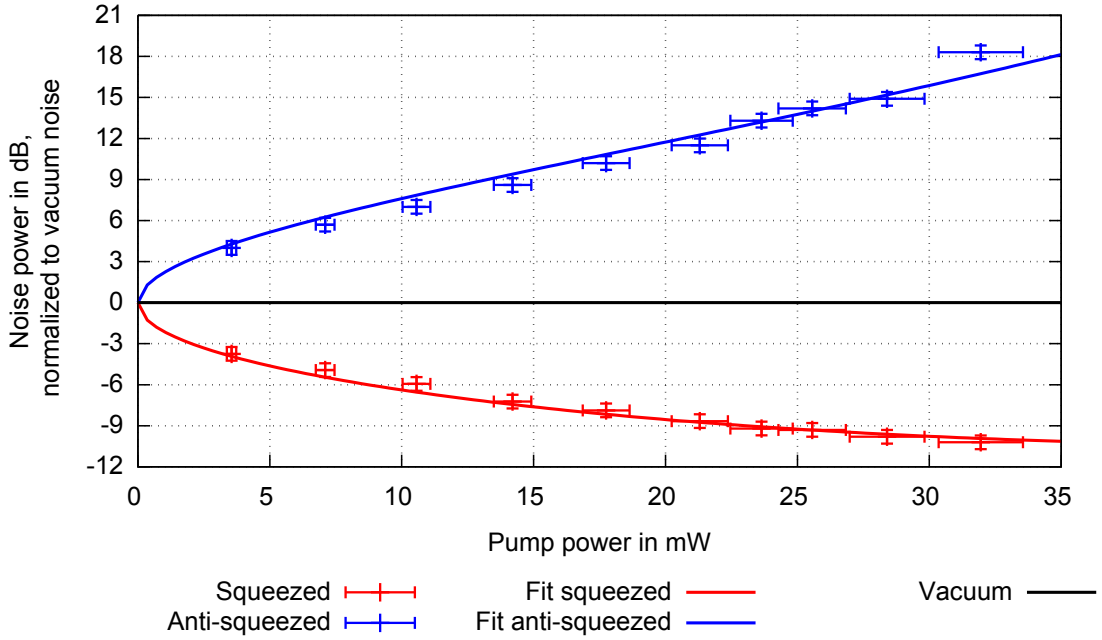

Figure 6.11: Noise power of squeezed states normalized to vacuum noise at the sideband frequency of 5 MHz for different pump powers. The measurements were performed in individual measurements for pump powers between 3.5 mW and 32 mW and normalized to the vacuum noise (black solid trace). For each measurement the temperature of the crystal was adjusted due to different heating by absorption of the pump power. The phase of the local oscillator was manually set to measure noise power in the squeezed (red crosses) or anti-squeezed (blue crosses) quadrature. Afterwards, a fit of equation (5.16) to the noise power in both quadratures was performed with the respective sign (red solid trace for noise power in squeezed, blue solid trace for anti-squeezed quadrature). The fit resulted in values of $P_{\mathrm{th}} = 52\,\mathrm{mW}$ for the pump threshold, a linewidth of $\gamma_{\mathrm{lw}} = 2\pi \cdot 102\,\mathrm{MHz}$.

CHAPTER 7

Interferometer enhancement at low frequencies by high-frequency squeezed states

Balanced homodyne-detection measurements at frequencies in the audio band and their enhancement through squeezed light are technically challenging due to several noise sources [St12]. Parasitic interferences from back-scattered stray light of the local oscillator [Sc18a, Va07], electronic noise, beam jitter, and coupling from noise on the local oscillator [Mc07] lead to measurements that are not quantum-noise limited. Additionally, the generation of squeezed states at low frequencies is challenging by itself [Va08]. Nevertheless, balanced homodyne detection is an important tool in quantum-optics measurements allowing to measure a signal in an arbitrary quadrature [BR04,Fr14]. The noise sources can be mitigated by using super-polished optical components, experiments in clean-room environments, special selection of electronics components, stable optics mountings and a very good beam splitting for the homodyne detection. However, these techniques are cost-intensive and require a specific know-how and are therefore not always feasible. In [Li17] the enhanced detection of a signal at low frequencies by using broadband squeezed states and a bichromatic local oscillator is reported. There, the squeezed field is produced detuned to the signal frequency and the measurement on the signal is conditionally improved on a measurement on the entangled sidebands. Here, we present the experimental realization of a squeezed-light-enhanced interferometer with a single monochromatic heterodyne readout of the signal. By shifting the local oscillator frequency, limitations at low frequencies can be avoided. The squeezed states in this scheme are at high sideband frequencies and are used to improve a measurement of a signal at low frequencies. We can show a signal-to-noise improvement of 3.4 dB. This scheme has the potential to improve experiments

where a homodyne detection at low frequencies or the generation of squeezed states at these frequencies is not possible.

7.1 Description of the detection scheme

We have a linear cavity of $L = 2.5\,\mathrm{m}$ length with a free spectral range of $\frac{\Delta}{2\pi} = c/(2L) = 58.73\,\mathrm{MHz}$. The transfer function of the cavity is shown in figure 7.1. The carrier field at the frequency ω_0 is resonant for the cavity. This implies, that light at the frequency $\omega_0 + \Delta$ is resonant as well. We produce squeezed states with a center frequency exactly in the middle of two resonance peaks, $\omega_{\mathrm{SQZ}} = \omega_0 + \Delta/2$. The squeezed states are reflected off the interferometer cavity, where the quantum-correlated lower and upper sidebands at ω_0 and $\omega_0 + \Delta$ acquire the same phase shift. In fact, the phase shift is equal for all entangled sidebands of the squeezed states, making the squeeze angle frequency-independent. We consider a signal to have a frequency of $|\delta|$. Together the carrier field, a signal at $\omega_0 \pm \delta$ and the squeezed field are sent onto a balanced detector. They are overlapped with a light field at the frequency $\omega_0 + \Delta$ serving as the local oscillator for a heterodyne measurement of the signal frequency. Due to the quantum correlations of the squeezed states the noise at the signal frequencies $\omega_0 \pm \delta$ can be conditionally squeezed by the upper sideband's noise at $\omega_0 + \Delta \mp \delta$. Compared to a homodyne measurement of a signal, a heterodyne detection suffers a 3 dB-reduction in signal-to-noise ratio [Bu03]. With the notation used in this description, the additional noise can be understood as follows: In a heterodyne readout, resolving the full signal at the two sidebands $\omega_0 \pm \delta$ involves a detection of *four* quantum-noise sidebands at $\omega_0 \pm \delta$ and $\omega_0 + \Delta \mp \delta$. In a homodyne readout of the same signal and with a local oscillator at ω_0, only *two* quantum noise sidebands at $\omega_0 \pm \delta$ are involved.

7.2 Experimental setup

In this section the experimental setup for interferometer enhancement at low frequencies by high-frequency squeezed states is described. A schematic drawing of the setup is depicted in figure 7.2. In the following the highlighted subsections *Squeezed-light generation* (blue box), *Interferometer cavity* (grey box), *Sideband generation* (green box), *Orthogonal polarization lock* (yellow box) and *Balanced heterodyne detection* (red box) are addressed in more detail. Due to an already existing setup of a squeezed light source, the laser frequency defined the center frequency of the squeezed light. In the experiment the carrier field for the cavity was generated as described in chapter 5.2. I denote the carrier frequency by $\omega_{\mathrm{Carrier}} = \omega_0$ and the laser frequency $\omega_{\mathrm{Laser}} = \omega_0 + \Delta/2$.

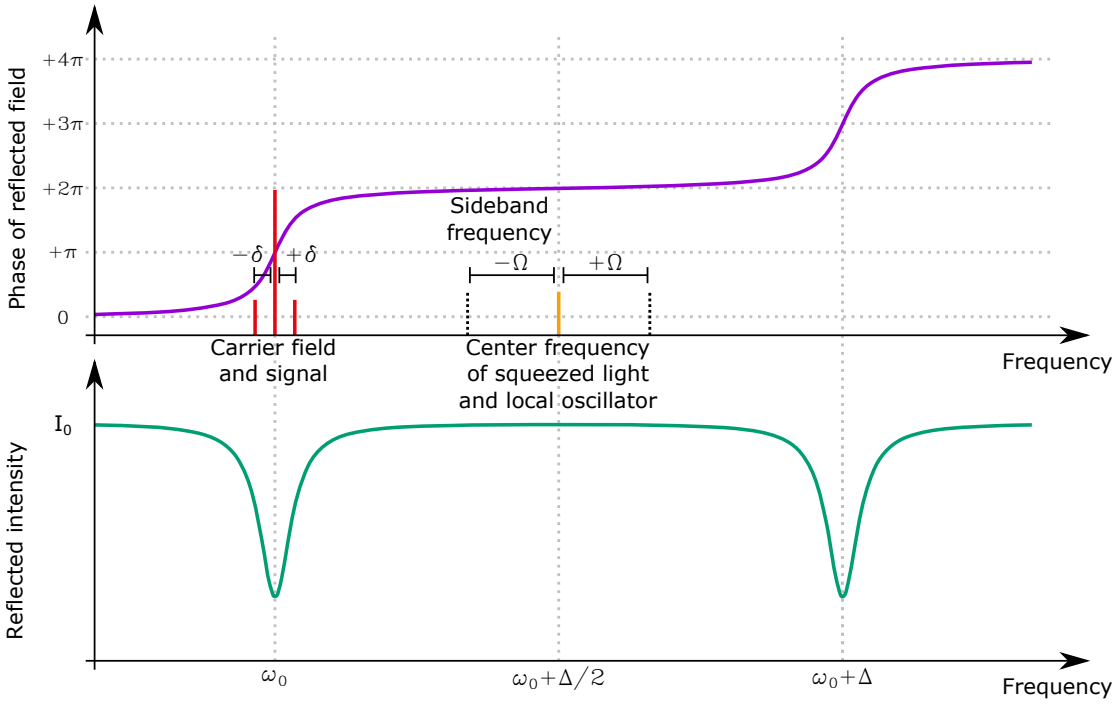

Figure 7.1: Transfer function of the interferometer cavity and involved sidebands for interferometer enhancement at low frequencies by high-frequency squeezed states. Shown are two adjacent resonance peaks of a cavity of length L being separated by one free spectral range $\frac{\Delta}{2\pi} = c/(2 \cdot L)$. The cavity is operated at the carrier frequency ω_0. The center frequency of the squeezed field is at half the free spectral range at $\omega_{\mathrm{SQZ}} = \omega_0 + \Delta/2$. Upon reflection off the cavity all sidebands that are entangled acquire the same phase shift, making the squeeze angle frequency-independent. We consider a signal to have a frequency of $|\delta|$. The local oscillator for the balanced heterodyne detection of the signal is at the center wavelength $\omega_0 + \Delta/2$ of the squeezed light.

7.2.1 Squeezed-light generation

The squeezed-light generation used here was already set up for previous work and is described in detail in [St13], [Ba13] and [As17].

A part of the laser light was sent to the second-harmonic generation cavity which consists of a magnesium-oxide-doped lithium niobate crystal. It is locked by the Pound-Drever-Hall locking scheme using a phase-modulation of 124.1 MHz. This setup is able to produce more than 200 mW of light at 532 nm, which is sufficient for the parametric down-conversion process. This field is further filtered by a mode cleaner ring cavity that is locked by an up-converted phase modulation of 124.1 MHz. Afterwards it is sent to the down-conversion cavity via a dichroic beam splitter. This cavity is monolithic and consisting of a periodically poled potassium

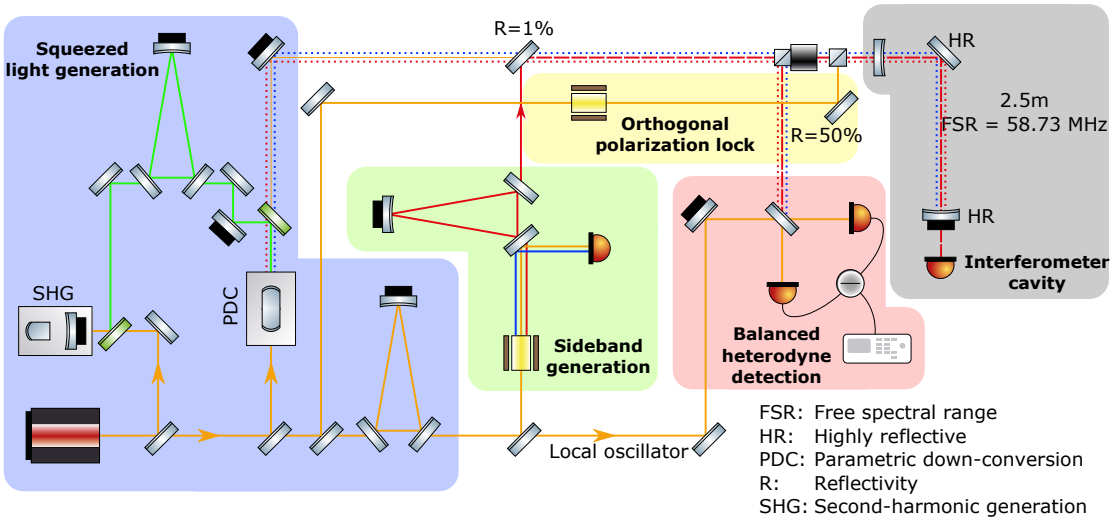

Figure 7.2: Schematic drawing of the setup for interferometer enhancement at low frequencies by high-frequency squeezed states. The setup is divided into the parts *Squeezed-light generation* (blue box), *Interferometer cavity* (grey box), *Sideband generation* (green box), *Orthogonal polarization lock* (yellow box) and *Balanced heterodyne detection* (red box). This overview excludes electronics and beams that are not important for the understanding of the detection scheme. A detailed description of the highlighted parts is given in the respective sections.

titanyl phosphate(PPKTP) crystal. A control field of the laser at the wavelength 1064 nm is sent to the back side of the cavity. The laser frequency is locked to this cavity by the Pound-Drever-Hall locking technique using a phase-modulation of 47.8 MHz on the control field. The phase of the pump field can be locked by demodulating the control field by an additional phase offset of 90 ° compared to the laser lock. The monolithic cavity has a full-width-half-maximum linewidth of $\frac{\gamma}{2\pi} = 156\,\mathrm{MHz}$. The squeezed light field generated in the cavity co-propagates with the control field towards the interferometer cavity. A tap-off of the laser light is filtered by a ring mode cleaner and serves as the local oscillator for the balanced heterodyne detection of the signal. The squeezed-light generation setup is shown in figure 7.3 including simplified electronic locking loops.

7.2.2 Interferometer cavity

In this experiment, a linear cavity of 2.5 m length served as an interferometer. The back mirror was highly reflective, whereas the coupling mirror had a reflectivity of 97 %. The cavity had a free spectral range of $\frac{\Delta}{2\pi} = 58.73\,\mathrm{MHz}$. The length of the cavity was a trade-off of having the free spectral range small enough with respect to the bandwidth of the squeezed light and fitting the cavity onto an

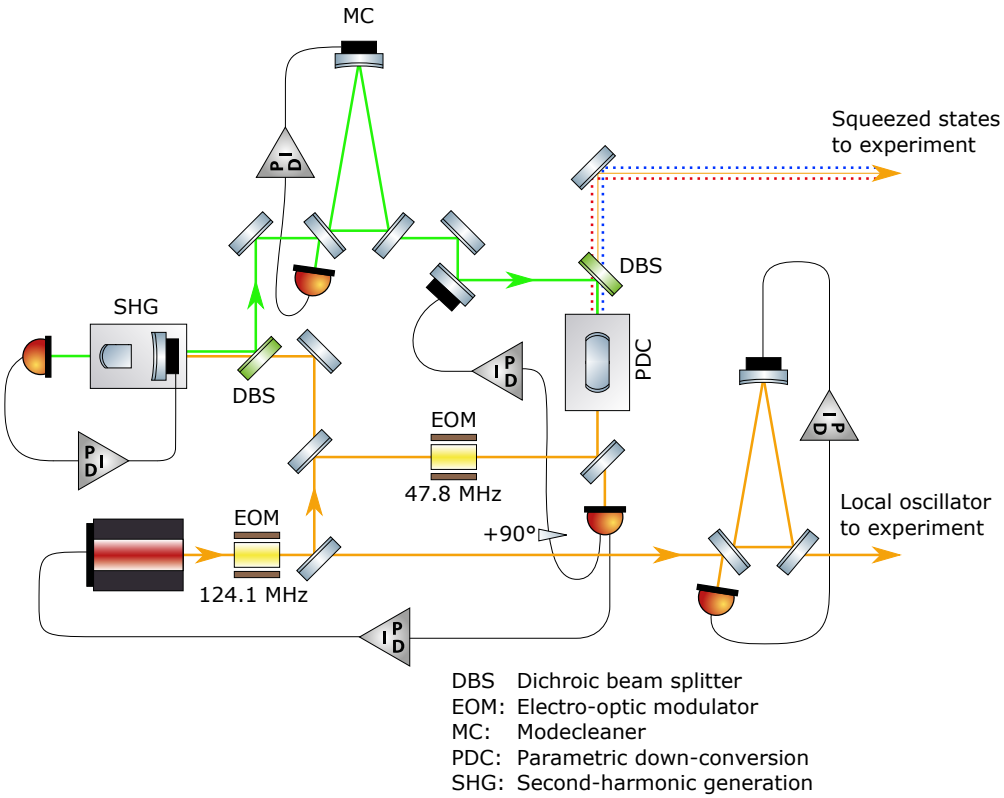

Figure 7.3: Schematic drawing of the squeezed-light generation. The laser frequency at 1064 nm is locked to the monolithic down-conversion cavity with the Pound-Drever-Hall locking technique. A part of the laser is sent to the second-harmonic generation cavity, producing $\sim 200\,\mathrm{mW}$ of light at 532 nm. This green field is filtered in a mode cleaner cavity and serves as the pump for the down-conversion process in a monolithic cavity consisting of a periodically poled potassium titanyl phosphate(PPKTP) crystal. The broadband squeezed field co-propagates with the transmitted control field towards the interferometer cavity. A tap-off of the laser light is filtered by a ring mode cleaner cavity to serve as a local oscillator in the balanced heterodyne detection. The drawing includes simplified electronic locking loops.

optical table. However, we needed to use a highly reflective mirror inside the cavity that allows for a 90° corner to achieve the desired length. Due to different penetration depth in the coating of this mirror for horizontally and vertically polarized light, the cavity had a slight detuning for the polarizations. Therefore, it was not resonant for both polarizations at the same time. The back mirror was mounted on a piezoelectric element to change the length of the cavity in the range of the wavelength of the carrier light field. Behind the cavity, a photo detector was placed to monitor the transmitted light power and to perform mode matchings to the cavity. The carrier field was overlapped with the squeezed field on a mirror

with a reflectivity of 1 % and detected in one port. The signal was demodulated with an electronic local oscillator at the beat frequency of 29.365 MHz an error signal for a phase lock of the two fields was generated and fed back to a piezoelectric element in the squeezed light path. Both fields were afterwards sent onto the interferometer cavity, the reflected field was separated by a Faraday rotator and sent to the balanced heterodyne detector. An electronic sinusoidal modulation at the frequency of 250 kHz was imprinted on the piezoelectric element of the cavity to simulate a signal. The interferometer cavity and the balanced heterodyne detection are shown in figure 7.4.

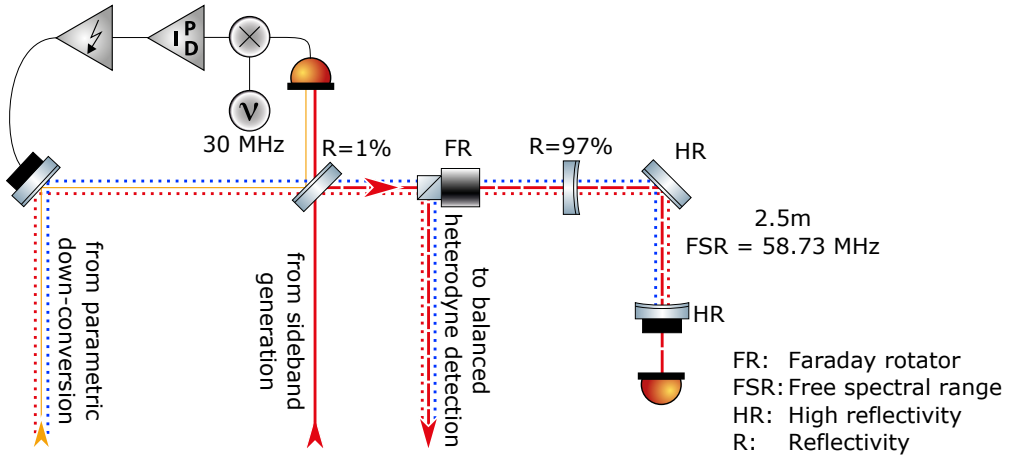

Figure 7.4: Schematic drawing of the linear cavity including the phase lock between carrier light and squeezed field. The cavity has a length of 2.5 m which results in a free spectral range of 58.73 MHz. A highly reflective mirror is placed inside the cavity due to the limited length of the optical table. This mirror creates a slight detuning for different polarizations. The squeezed light is overlapped with the carrier light on a mirror with a reflectivity of 1 % and the transmitted field is sent to the cavity. The reflected light is used to create a phase lock of the squeezed field and carrier field by demodulating the signal with the beat frequency of 29.365 MHz and feeding the error signal back to a piezoelectric element in the path of the squeezed light. The squeezed light passes a Faraday rotator and is sent onto the cavity. The reflected field is reflected by the rotator and sent to the balanced heterodyne detection.

7.2.3 Cavity lock in orthogonal polarization

The interferometer cavity needed to be locked to resonance for the carrier field at the frequency ω_0 in horizontal polarization. Unfortunately, standard approaches were not feasible here. A lock via the Pound-Drever-Hall locking technique using a phase modulation on the carrier field requires a strong carrier light field being

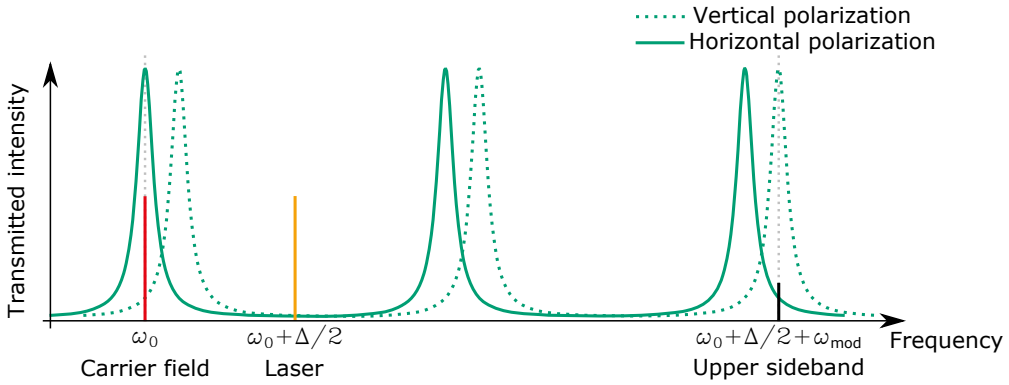

Figure 7.5: Scheme for locking the cavity on a sideband of an additional, phase-modulated field in orthogonal polarization to the signal field. This scheme avoids an impact of the lock field on the signal and allows an easy separation both fields. Shown are the resonance peaks of the linear cavity for the horizontal (green solid line) and vertical polarization (green dashed line). The phase modulation on the lock field was chosen such that the cavity is simultaneously resonant for the upper sideband of the modulation and the signal field. The modulation frequency was therefore $\frac{\omega_{\mathrm{mod}}}{2\pi} = 89.1\,\mathrm{MHz}$.

present for this lock. This results in a strong beat with the local oscillator saturating the detector. The cavity can as well not be locked on a carrier field in the vertical polarization using the Pound-Drever-Hall lock, since the cavity was not degenerate in the polarization modes due to the mirror inside the cavity.

Here, a modification of the Pound-Drever-Hall scheme combined with an additional field in the orthogonal polarization was used. Light in the vertical polarization was tapped off the laser at the frequency $\omega_0 + \Delta/2$ and a phase modulation at the frequency ω_{mod} was applied to this field. The modulation frequency was tuned such that the upper sideband of the modulation at $\omega_0 + \Delta + \omega_{\mathrm{mod}}$ was simultaneously resonant for the cavity as the carrier light at ω_0 in the horizontal polarization. The modulation frequency was therefore $\frac{\omega_{\mathrm{mod}}}{2\pi} = 89.1\,\mathrm{MHz}$. The cavity could now be locked using the zero-crossing of the error signal that occurs for the upper sideband and made it as well resonant for the carrier light. This idea is presented in figure 7.5 including the involved frequencies.

The lock field was overlapped with the signal field on a polarizing beam splitter in front of the linear cavity. After being reflected off the cavity, it was separated by the same beam splitter of the signal field and sent to a 50/50 beam splitter. The transmitted part was sent on a photo detector and mixed with an electronic oscillator at the modulation frequency. Thereby, an error signal is generated and the cavity is locked on the upper sideband which coincided with the resonance of the signal field. The schematic setup of this lock is shown in figure 7.6.

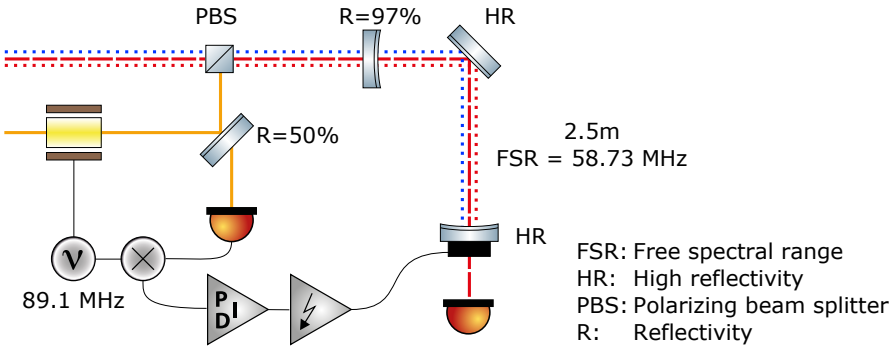

Figure 7.6: Schematic drawing of the lock of the interferometer cavity in orthogonal polarization to the signal field. On the laser field in vertical polarization a phase modulation of 89.1 MHz was imprinted. That frequency was chosen to match the cavity resonance of the signal field in the horizontal polarization. Both fields in orthogonal polarizations were overlapped on a polarizing beam splitter and sent to the cavity. The reflected lock field was sent to a 50/50 beam splitter, sent to a photo detector and the signal was demodulated with an electronic local oscillator at 89.1 MHz. This error signal was used to lock the cavity on resonance for the upper sideband of the phase modulation in vertical polarization. This coincided with the resonance of the signal field in horizontal polarization.

7.2.4 Balanced heterodyne detection

The reflected fields of the interferometer cavity, consisting of the carrier field at ω_0, the signal at $\omega_0 \pm \delta$ and the squeezed field, were overlapped with the local oscillator at the frequency of $\omega_0 + \Delta/2$. The detector had a demodulation stage that was used to demodulate the signal with an electronic oscillator at 47.8 MHz. After low-pass filtering, this error signal was used to lock the phase of the squeezed field and the local oscillator. In one of the arms of the heterodyne detector, a flip mirror was placed to mode match all fields onto a diagnose mode cleaner to achieve the best mode overlap on the beam splitter. The signal of the detector was high-pass filtered and sent to a spectrum analyzer.

7.3 Experimental results

For the experiments presented in this chapter, the pump power of the parametric down-conversion cavity was set to 100 mW. Firstly, the squeezed states were sent directly onto the detector with a bypass to check the properties of the down-conversion cavity. Since the local oscillator frequency and the center frequency of the squeezed light are equal, a homodyne detection of the squeezed field was performed here. At the sideband frequency of 5 MHz the squeezed states showed a noise reduction of 10.1 dB below the vacuum noise for the squeezed quadrature

and correspondingly an increase of 17 dB above vacuum noise for the anti-squeezed quadrature. The optical power of the control field was 0.5 mW.

To illustrate the limitations of generating squeezed light at low frequencies, I took a spectrum of the squeezed field with the control field in the sideband range from $f = 50\,\mathrm{kHz}$ to $f = 10\,\mathrm{MHz}$, where the readout angle of the homodyne detector was locked to measure the squeezed quadrature. The results are shown in figure 7.7. Due to the control field, squeezed properties (red trace) were only measured above $\sim 2.5\,\mathrm{MHz}$. Below this frequency, the noise was even increased above the vacuum noise (black trace) due to technical noise on the control field. The electronic darknoise (green trace) was not limiting in this sideband range. Measurements of signals below 2.5 MHz could not be improved by squeezed light in this configuration. This limitation motivates the implementation of the scheme for interferometer enhancement at low frequencies by high-frequency squeezed states presented in this chapter.

7.3.1 Double-sided spectrum of the squeezed-light-enhanced measurement by heterodyne detection

For the demonstration of the improvement of signals at low frequencies, the squeezed states were sent onto the interferometer cavity. Firstly, the results are presented as a double-sided spectrum as directly measured by the heterodyne detector. The cavity was locked on resonance for the carrier light and a signal was generated by a modulation of $\frac{\delta}{2\pi} = 250\,\mathrm{kHz}$ to the piezoelectric element. Since the local oscillator was at the center wavelength of the squeezed light the carrier light created a peak at $f = 29.365\,\mathrm{MHz}$ in the spectrum. The signal was present at $f = 29.365\,\mathrm{MHz} \pm 250\,\mathrm{kHz}$. The spectrum of this measurement is shown in figure 7.8. All measurements were taken with a resolution bandwidth of 6.25 kHz and a video bandwidth of 50 Hz. Without the application of squeezed light, the signal had a signal-to-noise ratio of $19.2\,\mathrm{dB} \pm 0.2\,\mathrm{dB}$ (blue trace). Here, the path from the down-conversion cavity was blocked and the noise level was given by vacuum noise. This was verified in a measurement where the path from the cavity to the detector was blocked (grey trace) and vacuum noise was recorded. This had the same noise power as the noise limiting the measurement with the open port. By applying detuned squeezed states to the cavity (red trace), the signal-to-noise ratio was improved to $22.6\,\mathrm{dB} \pm 0.2\,\mathrm{dB}$. This corresponds to an improvement of $3.4\,\mathrm{dB} \pm 0.3\,\mathrm{dB}$ compared to the measurement without squeezed light. In all measurements the carrier field showed a broadened peak around 29.365 MHz due to technical noise on the carrier field. The modulation of 250 kHz was chosen to be outside the influence of the technical noise. In all measurements, including the dark noise (black trace), a peak at 29.365 MHz is visible due to electronic pick-up from the frequency generators. The enhancement by the squeezed light was mainly limited by the mode matching from the cavity to the diagnostic mode

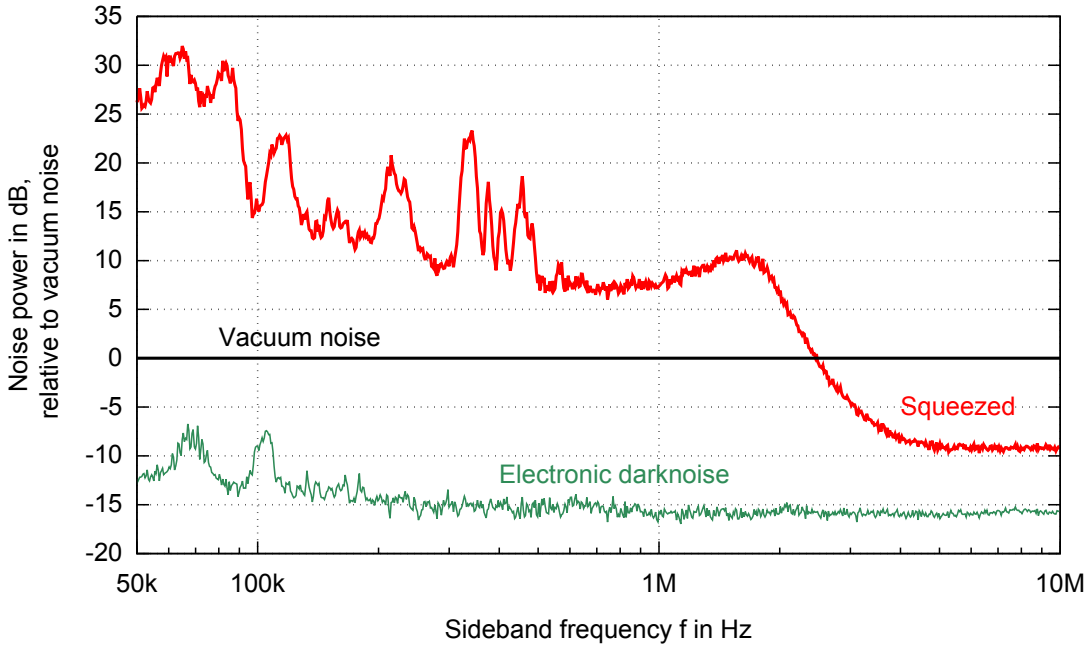

Figure 7.7: Spectrum of noise power of squeezed states with a copropagating control field of the source used in this chapter. This measurement illustrates the limitation of generating squeezed states at low frequencies in this setup. The measured noise power (red trace) was only reduced below vacuum noise (black trace) for sideband frequencies above $f = 2.5\,\mathrm{MHz}$. Below that frequency, the noise was even increased due to technical noise on the control field. Squeezed properties at low frequencies are only achievable if the control field is switched off. However, this field is used for locking purposes here. This limitation motivates the implementation of the scheme for interferometer enhancement at low frequencies by high-frequency squeezed states presented in this chapter.

cleaner of the heterodyne detector of a value of $\sim 80\,\%$ and the small dark noise clearance of 8.5 dB of the vacuum noise. The modematching was limited by an additional mode, whose origin was not understood, but which may resulted from a reflection of the anti-reflective coating of the coupling mirror of the cavity. A higher local oscillator power to increase the dark noise clearance was not feasible here due to saturation of the heterodyne detector.

7.3.2 Single-sided spectrum of the squeezed-light-enhanced measurement

To compare these results to a typical measurement, the output from the heterodyne detector was electronically demodulated at 29.365 MHz. Thereby, a single-

sided spectrum was created. The results are shown in figure 7.9. All measurements were taken with a resolution bandwidth of 10 kHz and a video bandwidth of 500 Hz. Here, a signal-to-noise ratio of 18.4 dB ± 0.2 dB was measured, where the squeezed light was blocked (blue trace). Again, this noise was checked to be vacuum noise by a measurement with a blocked path from the interferometer cavity to the heterodyne detector. The application of squeezed states resulted in a signal-to-noise ratio of 21.9 dB ± 0.2 dB, being an improvement of 3.5 dB ± 0.3 dB (red trace), which is in good accordance to the result of the measurement of the double-sided spectrum. However, the difference in the absolute signal-to-noise ratio can not be fully explained by the different resolution bandwidths. Below the signal frequency of $f = 250$ kHz, an influence of the technical noise on the carrier field was visible in a higher noise on both measurements with the signal field. The dark noise clearance of 8.5 dB (black trace) and the mode matching were again the limiting factors.

7.4 Conclusion

With the scheme introduced in this chapter an interferometer enhancement at low frequencies by high-frequency squeezed states was demonstrated. By applying detuned squeezed states and performing a heterodyne measurement we showed an increase of signal-to-noise ratio of 3.4 dB ± 0.3 dB. We presented the results in a double-sided spectrum, as directly measured, and in a single-sided spectrum generated by electronic demodulation. In comparison to a homodyne measurement of the signal this scheme suffers a 3 dB penalty. Since the improvement was higher then 3 dB an overall improvement in signal-to-noise ratio was still achieved. The main limitations of the improvement factor were the mode matching of the interferometer cavity to the heterodyne detector of only $\sim 80\,\%$ and the dark-noise clearance of the vacuum noise level of 8.5 dB. For future experiments the additional mode in the mode matching should be investigated and its influence reduced. The heterodyne detector can be equipped with electronic components generating less dark noise or additional filters for reducing the saturation. To achieve a lower frequency of the signal, the influence of technical noise on the carrier field can be reduced, e.g. by additional filter cavities.

We suggest this scheme to be used in experiments where a homodyne detection at low frequencies is not possible due to the mentioned limitations or the generation of squeezed states at these frequencies is not feasible.

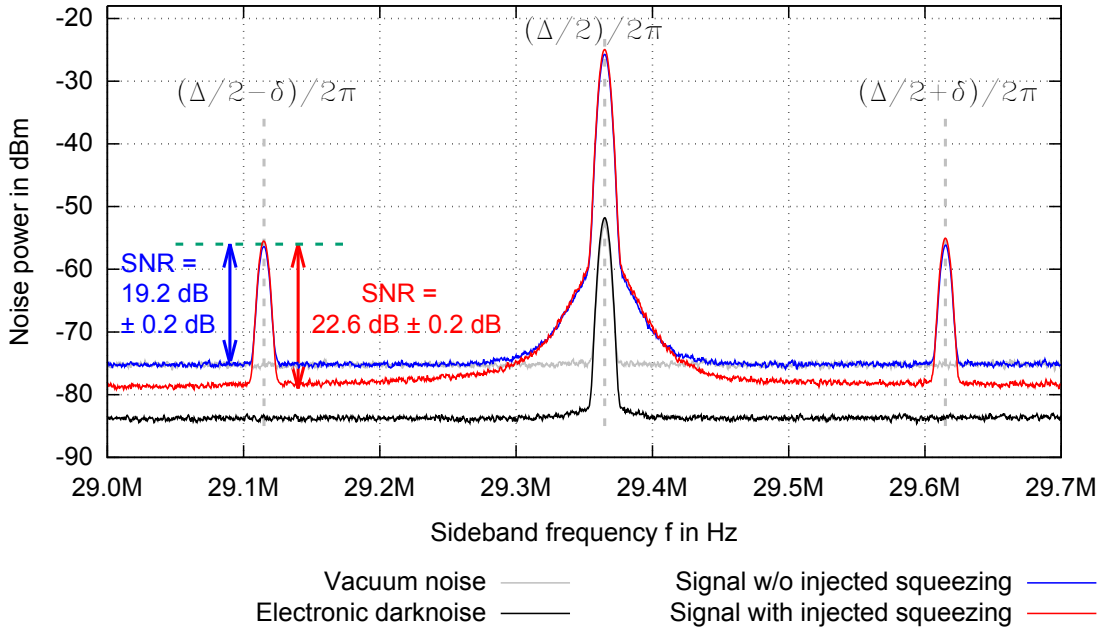

Figure 7.8: Double-sided spectrum of a squeezed-light-enhanced measurement in a heterodyne readout scheme. The interferometer cavity was locked on resonance and a signal at $\delta/(2\pi) = 250\,\mathrm{kHz}$ was imprinted by a modulation of the piezoelectric element. Due to the heterodyne readout the carrier field created a peak at $(\Delta/2)/(2\pi) = 29.365\,\mathrm{MHz}$. The signal was present at $(\Delta/2 \pm \delta)/(2\pi) = 29.365\,\mathrm{MHz} \pm 250\,\mathrm{kHz}$. Without the application of squeezed light (blue trace), the signal-to-noise ratio was $19.2\,\mathrm{dB} \pm 0.2\,\mathrm{dB}$. The noise was independently confirmed to be vacuum noise by a measurement with a blocked path from the cavity to the heterodyne detector (grey trace). With the application of detuned squeezed states, a signal-to-noise ratio of $22.6\,\mathrm{dB} \pm 0.2\,\mathrm{dB}$ was achieved. This is an improvement in the sensitivity of $3.4\,\mathrm{dB} \pm 0.3\,\mathrm{dB}$. The influence of technical noise on the carrier light was visible in a broadened peak around $f = 29.365\,\mathrm{MHz}$. The signal frequency was chosen to be outside this influence. The improvement was mainly limited by the mode matching from the cavity to the diagnostic mode cleaner of the heterodyne detector and the dark noise clearance of the vacuum noise level of 8.5 dB (black trace). On all traces a peak at $f = 29.365\,\mathrm{MHz}$ was visible that resulted from electronic pick-up from the frequency generators.

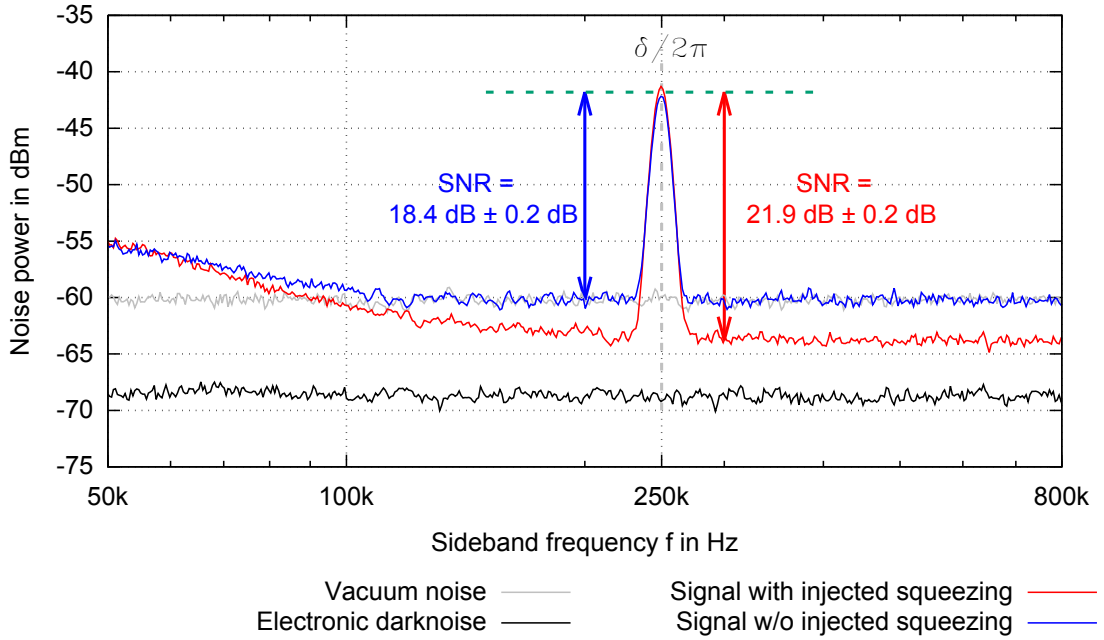

Figure 7.9: Single-sided spectrum of a squeezed-light-enhanced measurement in a heterodyne readout scheme. The cavity was locked on resonance for the carrier light and a modulation at 250 kHz was applied to the piezoelectric element changing the cavity length. The output from the heterodyne detector was electronically demodulated with a frequency of 29.365 MHz. This created a single-sided spectrum. All measurements were taken with a resolution bandwidth of 10 kHz and a video bandwidth of 500 Hz. With a blocked path from the parametric down-conversion cavity a signal-to-noise ratio of 18.4 dB ± 0.2 dB was achieved (blue trace). The noise was vacuum noise, which was verified by a measurement with a blocked path from the cavity to the heterodyne detector (grey trace). The application of detuned squeezed states led to a signal-to-noise ratio of 21.9 dB ± 0.2 dB, which is an improvement of 3.5 dB ± 0.3 dB.

CHAPTER 8

Demonstration of interferometer enhancement through EPR entanglement

For the broadband squeezed-light enhancement of gravitational-wave detectors a frequency-dependent rotation of the squeezed quadrature is necessary [Un83,JR90]. This rotation can be achieved by external filter cavities off which the squeezed states are reflected [Ki01]. In section 4.5 a novel scheme for the broadband reduction of vacuum noise in gravitational-wave detectors by squeezed-light injection was described *making* additional filter cavities obsolete. The authors of the proposal suggest the utilization of the signal-recycling cavity of the interferometer to achieve a frequency-dependent quadrature rotation. The squeezed states are sent into the output port of the interferometer. The center frequency of the squeezed states is detuned to be almost in the middle between two adjacent free spectral ranges of the signal-recycling cavity. It is set such that a lower sideband ω_{L} is resonant for the cavity, but the associated Einstein-Podolsky-Rosen(EPR)-entangled sideband at ω_{U} is off-resonant and acquires a frequency-dependent phase rotation. The carrier light of the cavity is at the frequency ω_{L}. The gravitational-wave signal is measured around ω_{L} and conditioned on a second measurement around the frequency ω_{U}.

This chapter is dedicated to an experimental realization of the detection of such detuned-cavity reflected EPR-entangled states. A $L = 2.5\,\mathrm{m}$-long linear cavity was emulating the signal-recycling cavity of a gravitational-wave interferometer. In the proposal by [Ma17] a filter cavity is introduced to separate the signals from the lower and upper sidebands. Afterwards, a homodyne measurement on each beam centered at the frequencies ω_{L} and ω_{U} is performed. In contrast to that, we built a readout scheme using a bichromatic local oscillator at the frequencies

ω_{L} and ω_{U} to avoid the need of the output filter cavity. This allowed measuring the fields reflected off the cavity on a single homodyne detector. Disadvantageous is the fact that we can not use a frequency-dependent (electronic) gain for the conditioning as proposed in [Ma17]. The gain between the two measurements can be influenced frequency-independently by using different local oscillator powers.

In our experiment the frequencies for the local oscillators were individually changeable. The measurements were taken for different sets of the detunings for the local oscillator frequencies. With these measurements we are able to show that the experimental results are in good accordance with a theoretical model we derived based on the work in [Ma17].

8.1 Theoretical model

This section presents the theoretical model of the noise spectra of initially frequency-independently squeezed states, being reflected off a cavity and read out by a bichromatic local oscillator. The formalism is similar to the description used in [Ma17] and was derived by Mikhail Korobko. The detailed description can be found in the appendix A.1. The calculations were done with *Mathematica 9.0/11.0* and a respective notebook is presented in the appendix A.2. The relation of the involved frequencies is explained in figure 8.1. The detunings of the lower and upper local oscillator to the resonance frequency of the cavity are described by δ_1 and δ_2. The relative powers of the local oscillators are described by α and β and the readout angle of the homodyne detection by ξ. The squeeze parameter is given by r and the total detection efficiency by η. The cavity has the half-width-half-maximum linewidth of γ. Given these parameters, the formula of the spectral density at the sideband frequency $\Omega = 2\pi \cdot f$ reads

$$
\begin{aligned}
S_{\mathrm{yy}} =& 1 - \eta + \eta\cosh(2r) + 2\alpha\beta\eta\sinh(2r)\cdot \\
&\Big[\left(\gamma^4 + (\delta_1^2 - \Omega^2)(\delta_2^2 - \Omega^2) - \gamma^2(\delta_1^2 + \delta_2^2 - 2\Omega^2 + 4\delta_1\delta_2)\right)\cos(\xi) \\
&\quad + 2\gamma(\delta_1 + \delta_2)(\gamma^2 - \delta_1\delta_2 + \Omega^2)\sin(\xi)\Big]\cdot \\
&\qquad \frac{\left[\gamma^4 + (\delta_1^2 - \Omega^2)(\delta_2^2 - \Omega^2) + \gamma^2(\delta_1^2 + \delta_2^2 + 2\Omega^2)\right]}{(\alpha^2 + \beta^2)(\gamma^2 + (\delta_1 - \Omega)^2)(\gamma^2 + (\delta_2 - \Omega)^2)(\gamma^2 + (\delta_1 + \Omega)^2)(\gamma^2 + (\delta_2 + \Omega)^2)}\,.
\end{aligned}
\tag{8.1}
$$

The formula does not include losses inside the cavity. Including these losses into the model is possible by extending the transfer functions from equation (A.13) and introducing additional vacuum fields. However, the formula for the spectral density becomes very complex in this case. We omitted this extension as we expect the additional losses to be very small. For the formula an infinite bandwidth of the squeezed spectrum was assumed.

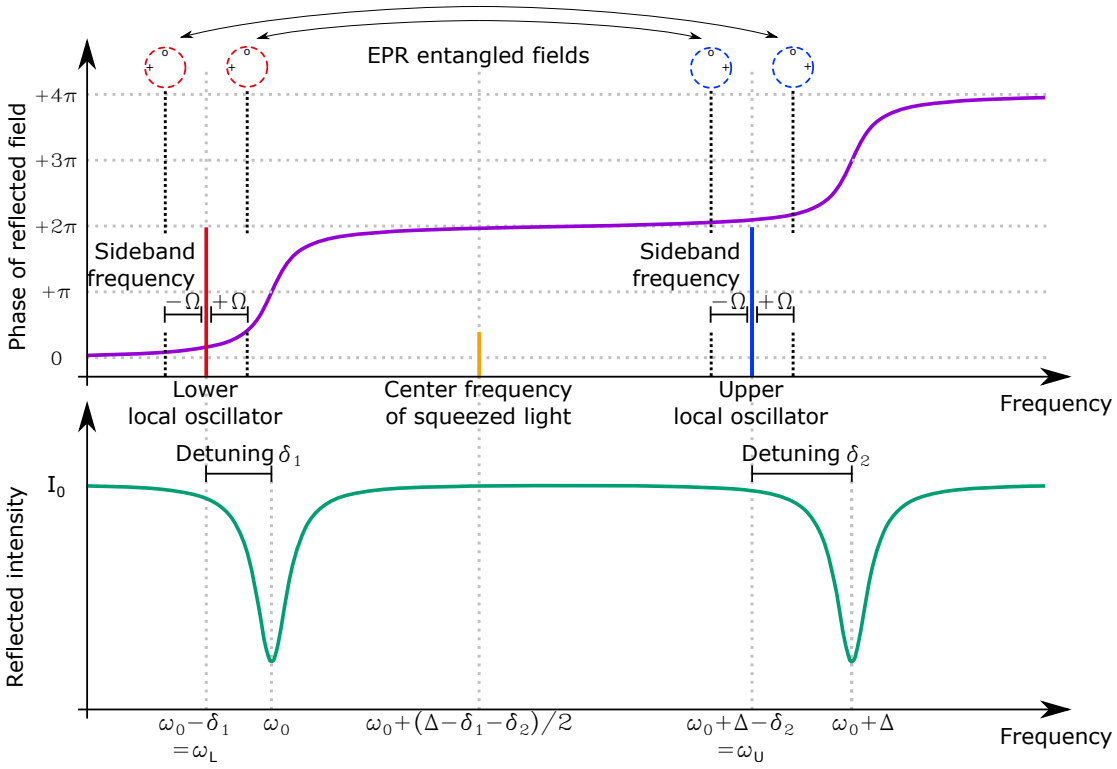

Figure 8.1: Transfer function of the interferometer cavity and involved frequencies. The transfer function shows the phase and intensity of a field reflected off a cavity. The cavity has a free spectral range of $\Delta = c/(2L)$. It is resonant for the optical frequencies ω_0 and for $\omega_0 + \Delta$. The two local oscillators are at frequencies $\omega_\mathrm{L} = \omega_0 - \delta_1$ and $\omega_\mathrm{U} = \omega_0 + \Delta - \delta_2$. Each measurement with a local oscillator is performed at an upper and lower sideband frequency $\pm\Omega$. The center frequency of the squeezed light is at the frequency of $\omega_\mathrm{SQZ} = \omega_0 + (\Delta - \delta_1 - \delta_2)/2$ exactly in middle between the two local oscillators.

8.2 Experimental setup

The setup was similar to the one from chapter 7 and presented in figure 8.2. The broadband squeezed-light source (blue box) and the $L = 2.5\,\mathrm{m}$-long linear interferometer cavity (grey box) including the locking scheme (yellow box) remained unchanged. The length L of the cavity is a trade-off of fitting the cavity on an optical table and having a free spectral range $\frac{\Delta}{2\pi} = c/(2L) = 58.73\,\mathrm{MHz}$ small enough being inside the bandwidth of the squeezed light. The generation of the local oscillators (green box) was extended as described in section 5.2 to produce bright fields at both the lower and upper oscillator frequency. In the readout scheme (red box) the bichromatic local oscillator replaced the monochromatic local oscillator. Both single oscillators were overlapped on a beam splitter and one output port was

sent towards the detector. Additionally, a bypass for the squeezed light was set up to guide the squeezed field directly onto the balanced bichromatic homodyne detection without the interaction with the cavity (cyan box). With this bypass a characterization of EPR-entangled states with a bichromatic readout scheme was possible.

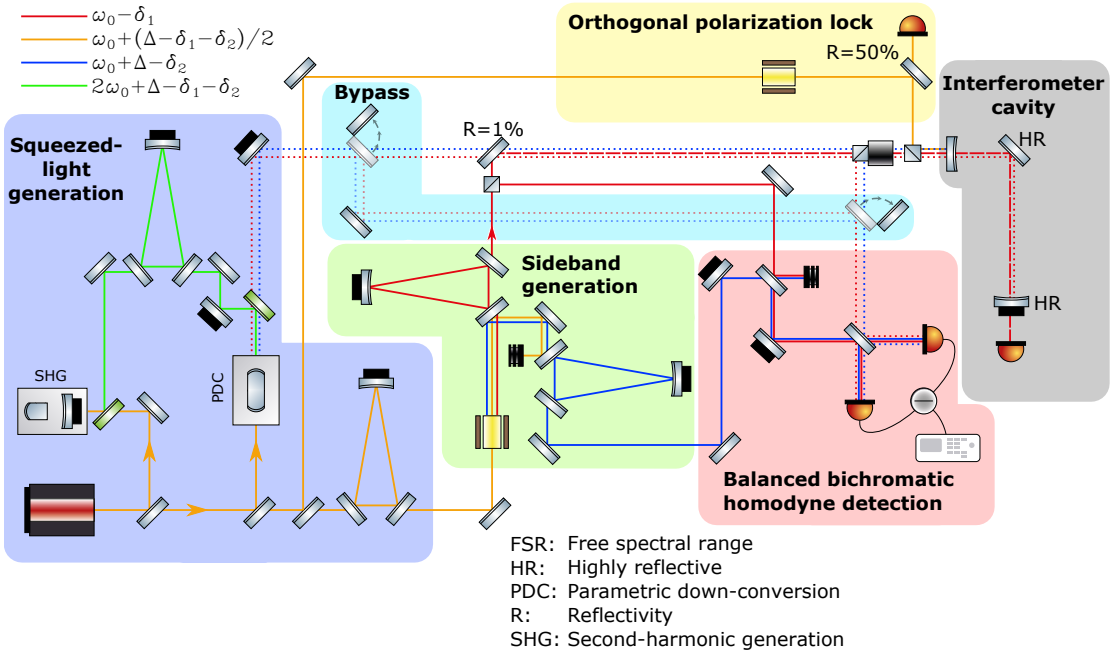

Figure 8.2: Schematic drawing of the setup for cavity enhancement through EPR entanglement. The squeezed light source (blue box) and the linear interferometer cavity including the locking scheme (yellow boy) remained unchanged compared to chapter 7. The generation of the local oscillators (green box) was extended to produce not only the lower but also the upper oscillator frequency. In the readout scheme (red box) the bichromatic local oscillator replaced the monochromatic local oscillator. The two single oscillators were overlapped on a beam splitter and one output port is sent towards the detector. Additionally, a bypass for the squeezed light (cyan box) was implemented to send the field directly onto the detector without being reflected off the interferometer cavity.

8.3 Experimental results

8.3.1 Spectrum of the noise power of squeezed states with a bichromatic local oscillator

Before investigating the EPR-entangled fields reflected off the cavity, I sent the squeezed states directly onto the bichromatic homodyne detector via the bypass shown in figure 8.2. Here, the squeezed light was centered around the frequency ω_{Laser}, and the lower and upper local oscillators were at frequencies $\omega_{\text{L/U}} = \omega_{\text{Laser}} \mp 2\pi \cdot 29.365\,\text{MHz}$. I chose the local oscillators frequencies at $\pm 2\pi \cdot 29.365\,\text{MHz}$ to fit to later measurements where these frequencies match half the free spectral range of the interferometer cavity. Due to the bichromatic local oscillator two homodyne measurements were performed simultaneously at sideband frequencies $\omega_{\text{L}} = \omega_{\text{Laser}} - 2\pi \cdot 29.365\,\text{MHz} \pm \Omega$ and $\omega_{\text{U}} = \omega_{\text{Laser}} + 2\pi \cdot 29.365\,\text{MHz} \mp \Omega$ and both were added directly. The power of each single local oscillator was 2 mW. Our spectrum analyzers measured sidebands in ordinary frequencies f instead of angular frequencies Ω and therefore all measurements are presented in ordinary frequencies f. The relation is given by $2\pi \cdot f = \Omega$. The measurements were taken in the sideband frequency band from $f = 1\,\text{MHz}$ to $f = 55\,\text{MHz}$, where I excluded measurements in the sideband frequency band from $f = 28\,\text{MHz}$ to $f = 30\,\text{MHz}$ due to electronic pickup of the sideband generation process. Since no control loop for the readout phase was installed, the phase was controlled manually by adjusting the offset voltage on piezoelectric element in the local oscillator path. The spectra of the noise powers of the squeezed and anti-squeezed quadrature, normalized to vacuum shot noise, are shown in figure 8.3. The squeezed quadrature (red trace) showed a maximal noise reduction of 6.5 dB below vacuum noise of both local oscillators, whereas the corresponding anti-squeezed quadrature (blue trace) showed an increase of 14 dB above the shot noise. The anti-squeezed quadrature showed the highest increase above vacuum noise around sideband frequencies of $f \approx 30\,\text{MHz}$. At these frequencies the local oscillators measured squeezed states close to the center frequency of the squeezed states, having the highest increase above shot noise. Both spectra were fitted with equation (5.17) with the corresponding sign for the squeezed (dashed blue) and anti-squeezed quadrature (dashed red), where the pump parameter $\sqrt{P/P_{\text{thres}}}$, the total detection efficiency η and the linewidth γ of the down-conversion cavity were the fitting parameters. The fit resulted in a linewidth of $\frac{\gamma}{2\pi} = 150\,\text{MHz}$, which is in good agreement with the linewidth measured in [Ba13]. The fit of the pump parameter resulted in $\sqrt{P/P_{\text{thres}}} \approx 0.76$ and the detection efficiency resulted in $\eta = 0.83$. The loss factor was high compared to a typical measurement of squeezed states. One the one hand the modematching of the squeezed field to the reference cavity was limited to 97%, on the other hand the readout scheme required matching an additional local oscillator to the reference cavity, resulting in more possible mismatches. Additionally, the param-

eters of the fit were used to simulate a measurement with a monochromatic local oscillator of squeezed state. The simulation shows the squeezed (dashed green) and anti-squeezed (dashed yellow) quadratures. The monochromatically measured noise power of the squeezed quadrature is always below the bichromatically measured squeezed quadrature. This is explained by the simultaneous measurement of two sideband frequencies of the squeezed states in the bichromatic measurement and the influence of the linewidth of the parametric down-conversion cavity. With the same argument the bichromatically measured anti-squeezed quadrature showed less increase of noise for lower measurement frequencies f compared to monochromatically measured anti-squeezed quadrature.

8.3.2 Relations of the involved frequencies

For the following measurements I removed the bypass shown in figure 8.2 and the EPR-entangled states were sent onto the interferometer cavity that was locked with the auxiliary field described in chapter 7.2.3. The reflected fields were then sent onto the bichromatic balanced homodyne detection. The measurements were taken for the following relations of the involved frequencies:

I Firstly, the upper and lower local oscillator were set to frequencies of $\omega_{\mathrm{L}} = \omega_0$ and $\omega_{\mathrm{U}} = \omega_0 + \Delta$ being resonant for the linear cavity, with a frequency difference Δ of one free spectral range of the cavity. This resulted in frequency-independent noise spectra, simulating an interferometer with tuned signal recycling and zero opto-mechanical coupling.

II Secondly, the upper local oscillator was detuned by δ_2 from resonance to a lower frequency $\omega_{\mathrm{U}} = \omega_0 + \Delta - \delta_2$ resulting in frequency-dependent noise spectra, simulating an interferometer with the influence of opto-mechanical coupling. The measurements were performed with two different detunings of **(a)** $\delta_2 = 2\pi \cdot 400\,\mathrm{kHz}$ and **(b)** $\delta_2 = 2\pi \cdot 4\,\mathrm{MHz}$.

III Afterwards, both local oscillators were detuned anti-symmetrically by $-\delta_1 = \delta_2 = 2\pi \cdot 400\,\mathrm{kHz}$ to frequencies of $\omega_{\mathrm{L}} = \omega_0 + \delta_1$ and $\omega_{\mathrm{U}} = \omega_0 + \Delta - \delta_2$. This led back to frequency-independent noise spectra and illustrated a broadband quantum-noise reduction. Additionally, it showed the broadband sensitivity-enhancement of a detuned signal-recycling cavity.

IV As a fourth step, both local oscillators were symmetrically detuned by $\delta_1 = \delta_2$ to frequencies of $\omega_{\mathrm{L}} = \omega_0 - \delta_1$ and $\omega_{\mathrm{U}} = \omega_0 + \Delta - \delta_2$ resulting in frequency-dependent EPR-entangled states, demonstrating that the system can produce frequency-dependent (conditional) squeezing. These measurements were performed for two different detunings of **(a)** $\delta_1 = \delta_2 = 2\pi \cdot 400\,\mathrm{kHz}$ and **(b)** $\delta_1 = \delta_2 = 2\pi \cdot 1\,\mathrm{MHz}$

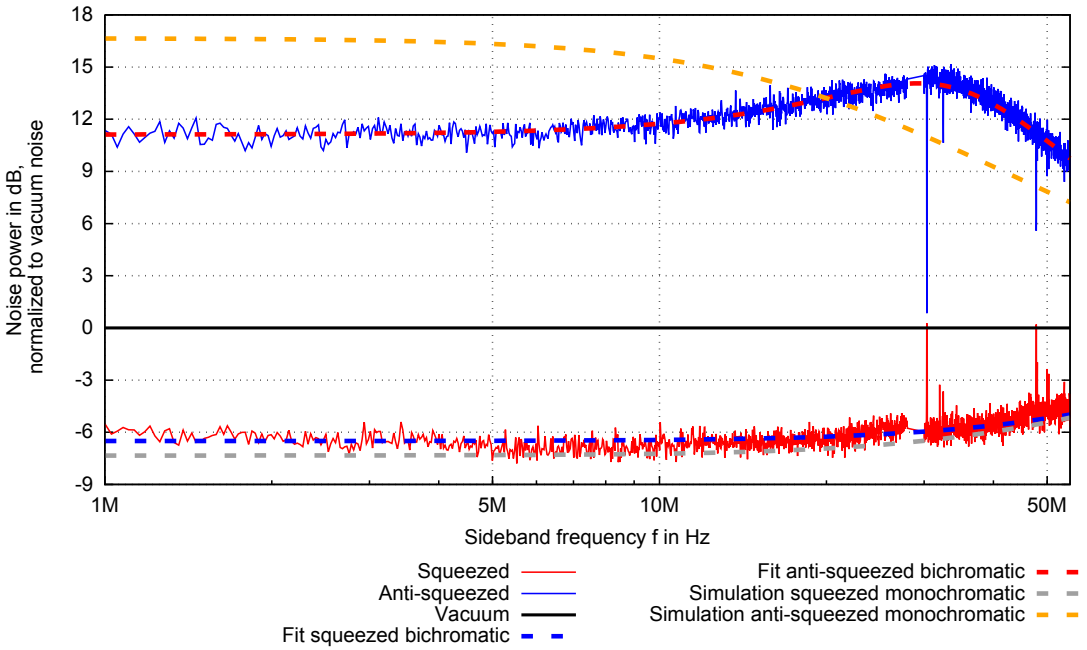

Figure 8.3: Spectrum of noise power of a broadband squeezed field detected with a bichromatic homodyne readout. The local oscillators are at frequencies $\omega_0 \pm 2\pi \cdot 29.365\,\mathrm{MHz}$ and the parametric-down conversion process is pumped at the frequency $2\omega_0$. Measurements in the frequency range of $f = 28\,\mathrm{MHz}$ to $f = 30\,\mathrm{MHz}$ are excluded due to electronic pickup of the sideband generation process. The squeezed quadrature (red trace) shows a maximal noise reduction of 6.5 dB below the vacuum noise of both local oscillators. The anti-squeezed quadrature shows a corresponding increase of 14 dB above the vacuum noise around the sideband frequency of $f \approx 30\,\mathrm{MHz}$. The fits of the measurements (dashed blue trace for squeezed, dashed red trace for anti-squeezed quadrature) yield parameters of $\frac{\gamma}{2\pi} = 150\,\mathrm{MHz}$ for the linewidth of the parametric down-conversion cavity, a pump parameter of $\sqrt{P/P_{\mathrm{thres}}} \approx 0.76$ and a detection efficiency of $\eta = 0.83$. For a comparison the simulation of squeezed and anti-squeezed quadrature with a monochromatic local oscillator and the same parameters is given (dashed green for squeezed, dashed yellow for anti-squeezed quadrature).

All measurement steps are presented on a double page, where on the top left page a spectrogram of the measured quantum noise power with a continuously swept phase of the local oscillator is shown. All spectrograms were recorded with a realtime analyzer. The quantum noise power was normalized to the shot noise of both oscillators. The theoretical model from equation (8.1) described in chapter 8.1 was fitted to the data. The readout angle was fitted with a quadratic function $\xi(t) = a + b \cdot t + c \cdot t^2$ to emulate a non-linear transfer function of

the piezoelectric element. The lower left picture shows the spectrogram of the fitted model. In both spectrograms the time axes were substituted with the fitted readout angle. The color coding is the same in all spectrograms. On the top right page the transfer function of the cavity for reflected light fields is shown including the involved frequencies of the local oscillators and the center wavelength of the squeezed light for every experimental step. In the lower right picture the spectra of two time traces of the spectrogram for readout angles of $\xi = (-)\pi/2$ and $\xi = (-)\pi$ is shown including the fitted model. The measurements were performed with local oscillators of 2 mW power each after overlapping them on the beam splitter. The fit parameters of all measurements are given in tables 8.1 and 8.2.

8.3.3 Results of bichromatic measurements of cavity-reflected EPR-entangled states

I. Bichromatic measurements of cavity-reflected EPR-entangled states without detuning

For the first measurement step, I set both local oscillator frequencies to be resonant for the cavity (detuning $\delta_1 = \delta_2 = 0$) as described in figure 8.5(a). All measured sidebands at frequencies $\omega_0 \pm \Omega$ and $\omega_0 + \Delta \mp \Omega$ acquired the same, but opposite phase shift upon reflection off the cavity and therefore the EPR-entangled fields were not rotated. This resulted in frequency-independent EPR-entangled states.

The measured quantum noise is shown in figure 8.4 in a spectrogram with a continuously swept phase and in a frequency range from 50 kHz to 2 MHz. The measurement shows that the quantum noise was frequency-independent. The model matches both spectra from figure 8.5(b). Only towards lower frequencies a deviation of the expected quantum noise is apparent. The origin can not be fully explained but might have arisen from one of the local oscillators not being exactly on resonance. Additionally, increasing darknoise of the detector for lower frequencies and a high-pass in the detectors output at 10 kHz limited the detection at low frequencies. The detection efficiency of $\eta = 0.69$ was even more reduced than in the measurements in chapter 8.3.1. This can be explained by additional losses due to a bad modematching from the interferometer cavity to the reference cavity of the homodyne detector. Here, a limiting mode appeared whose origin was not understood but might have arisen from a reflection of the anti-reflective coating of the coupling mirror of the cavity. The peak at $f = 1.1$ MHz resulted from electronic pickup, but was not identified.

II(a). Bichromatic measurements of cavity-reflected EPR-entangled states with detuning of the upper local oscillator of $2\pi \cdot 400$ kHz

In the second measurement step I set the lower local oscillator frequency to be resonant for the cavity (detuning $\delta_1 = 0$). The upper local oscillator was detuned

by $\delta_2 = 2\pi \cdot 400\,\mathrm{kHz}$ towards lower frequencies. This scheme is described in figure 8.7(a). The measured sidebands at frequencies $\omega_0 \pm \Omega$ and $\omega_0 + \Delta - \delta_2 \mp \Omega$ acquired different phase shifts upon reflection off the cavity. This resulted in frequency-dependent EPR-entangled states. The phase shift is strongest around $f = 400\,\mathrm{kHz}$.

The measured quantum noise is shown in figure 8.6 in a spectrogram with a continuously swept phase and in a frequency range from $f = 50\,\mathrm{kHz}$ to $f = 2\,\mathrm{MHz}$. The spectrogram shows that the quantum noise was frequency-dependent with a characteristic phase change around $f = 400\,\mathrm{kHz}$. The model matches both spectra from figure 8.7(b). Again, towards lower frequencies a deviation of the expected quantum noise is apparent. The peak at $f = 1.4\,\mathrm{MHz}$ resulted from electronic pickup, but was not identified.

II(b). Bichromatic measurements of cavity-reflected EPR-entangled states with detuning of the upper local oscillator of $2\pi \cdot 4\,\mathrm{MHz}$

This measurement was similar to the previous one. The detuning of the upper local oscillator is $\delta_2 = 2\pi \cdot 4\,\mathrm{MHz}$, resulting in the strongest phase shift around $f = 4\,\mathrm{MHz}$.

The measured quantum noise is shown in figure 8.8 in a spectrogram with a continuously swept phase and in a frequency range from $f = 50\,\mathrm{kHz}$ to $f = 6\,\mathrm{MHz}$. The spectrogram shows that the quantum noise was frequency-dependent with a characteristic phase change around 4 MHz. For this measurement also the detuning of the lower local oscillator δ_1 was included in the fit parameters and resulted in a small detuning of $\delta_1 = -2\pi \cdot 74\,\mathrm{kHz}$. This can be explained by an offset of the locking electronics of the interferometer cavity. The model matches both spectra from figure 8.9(b). Here, at sideband frequencies around $f = 4\,\mathrm{Mhz}$ a deviation of the expected quantum noise is apparent that can not be explained.

III. Bichromatic measurements of cavity-reflected EPR-entangled states with anti-symmetric detuning of both local oscillators of $2\pi \cdot 400\,\mathrm{kHz}$

For this measurement, the local oscillators were detuned by $-\delta_1 = \delta_2 = 2\pi \cdot 400\,\mathrm{kHz}$. As is the case without any detuning, all measured sidebands at frequencies $\omega_0 + 2\pi \cdot 400\,\mathrm{kHz} \pm \Omega$ and $\omega_0 + \Delta - 2\pi \cdot 400\,\mathrm{kHz} \mp \Omega$ acquired the same, but opposite phase shift upon reflection off the cavity and therefore the EPR-entangled fields were not rotated. This resulted again in frequency-independent EPR-entangled states.

The measured quantum noise is shown in figure 8.10 in a spectrogram with a continuously swept phase and in a frequency range from $f = 50\,\mathrm{kHz}$ to $f = 2\,\mathrm{MHz}$. The measurement shows that the quantum noise is frequency-independent. The

model matches both spectra from figure 8.11(b). Around $f = 400\,\mathrm{kHz}$ a little deviation from the expected model is apparent. This might have arisen from increases losses, when a field is resonant for the cavity. These losses are not included in the model. Again, towards lower frequencies a deviation is apparent.

IV(a). Bichromatic measurements of cavity-reflected EPR-entangled states with symmetric detuning of both local oscillators of $2\pi \cdot 400\,\mathrm{kHz}$

Here, the local oscillators were detuned by $\delta_1 = \delta_2 = 2\pi \cdot 400\,\mathrm{kHz}$. The measured sidebands at frequencies $\omega_0 - 2\pi \cdot 400\,\mathrm{kHz} \pm \Omega$ acquired the same phase shift upon reflection off the cavity as the sidebands at $\omega_0 + \Delta - 2\pi \cdot 400\,\mathrm{kHz} \mp \Omega$ and therefore the EPR-entangled fields were rotated depending on the sideband frequency Ω.

The measured quantum noise is shown in figure 8.12 in a spectrogram with a continuously swept phase and in a frequency range from $f = 50\,\mathrm{kHz}$ to $f = 2\,\mathrm{MHz}$. The measurement shows that the quantum noise was frequency-dependent with a characteristic phase change around $f = 400\,\mathrm{kHz}$. The model matches both spectra from figure 8.13(b). However, the fit resulted in detuning parameters that are equal but too low by $2\pi \cdot 60\,\mathrm{kHz}$ compared to the set values. This can be explained by an offset of the cavity lock that occurred during the measurement. Again, towards lower frequencies a deviation is apparent. The peak at $f = 1.4\,\mathrm{MHz}$ resulted from electronic pickup, but was not identified.

IV(b). Bichromatic measurements of cavity-reflected EPR-entangled states with symmetric detuning of both local oscillators of $2\pi \cdot 1\,\mathrm{MHz}$

This measurement was similar to the previous one, but the detunings of both oscillators were set to $\delta_1 = \delta_2 = 2\pi \cdot 1\,\mathrm{MHz}$. The EPR-entangled fields were again rotated and the rotation is depending on the sideband frequency Ω.

The measured quantum noise is shown in figure 8.14 in a spectrogram with a continuously swept phase and in a frequency range from $f = 50\,\mathrm{kHz}$ to $f = 2\,\mathrm{MHz}$. The measurement shows that the quantum noise was frequency-dependent with a characteristic phase change around $f = 1\,\mathrm{MHz}$. The model matches both spectra from figure 8.15(b). The fit resulted in detuning parameters that are both too low compared to the set values as in the previous case and might be explained in the same way. Additionally, the detuning parameters do not equal here which can not be explained. The peak at $f = 1.4\,\mathrm{MHz}$ resulted from electronic pickup, but was not identified.

I. Bichromatic measurements of cavity-reflected EPR-entangled states without detuning

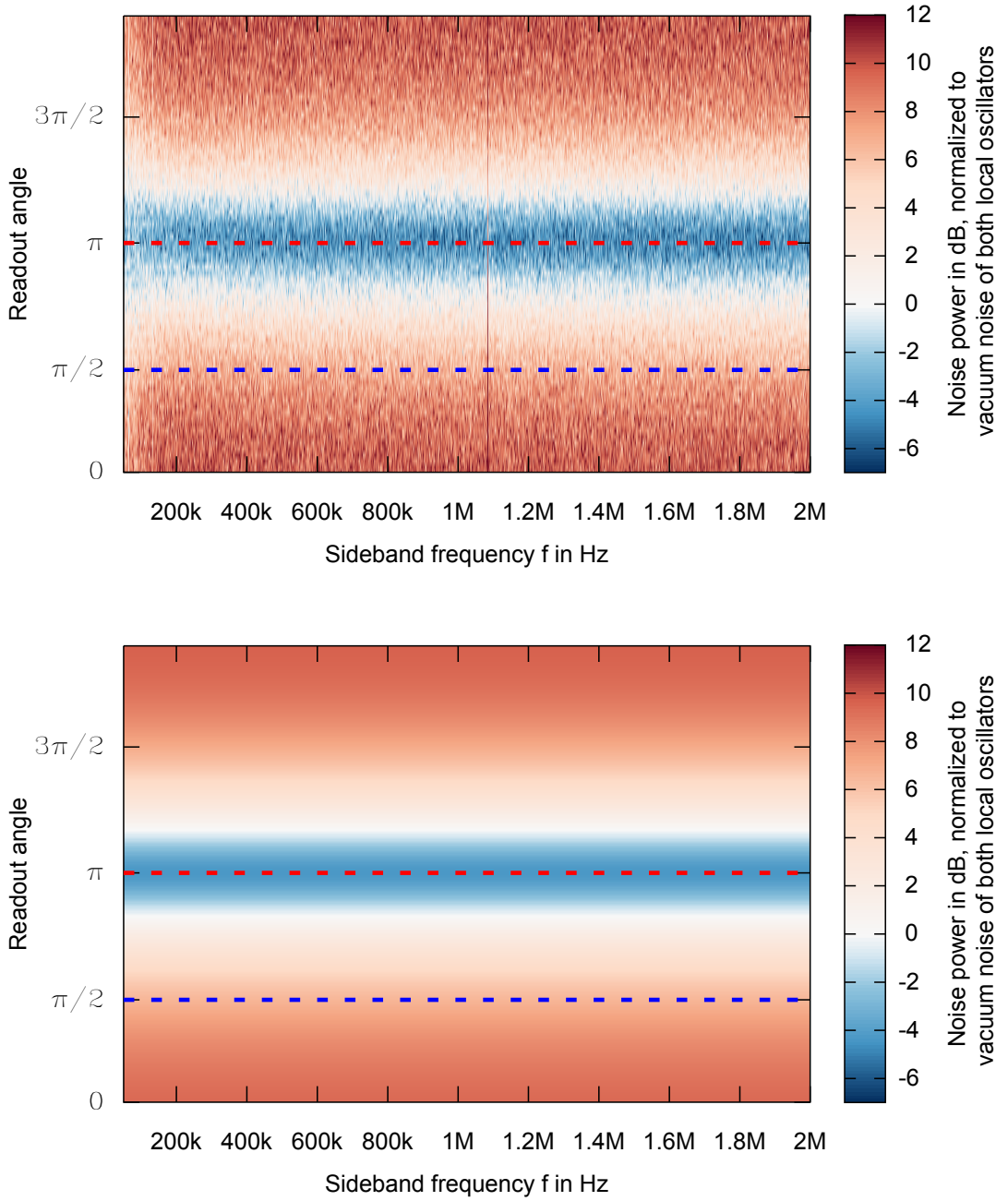

Figure 8.4: Spectrograms of measurements (upper subfigure) and fitted simulation (lower subfigure) without detuning of the local oscillators. The quantum noise was frequency-independent and for the readout angle of π a reduction below the vacuum noise was achieved. The readout angle is inferred from the fitting data. Further details are given in the main text.

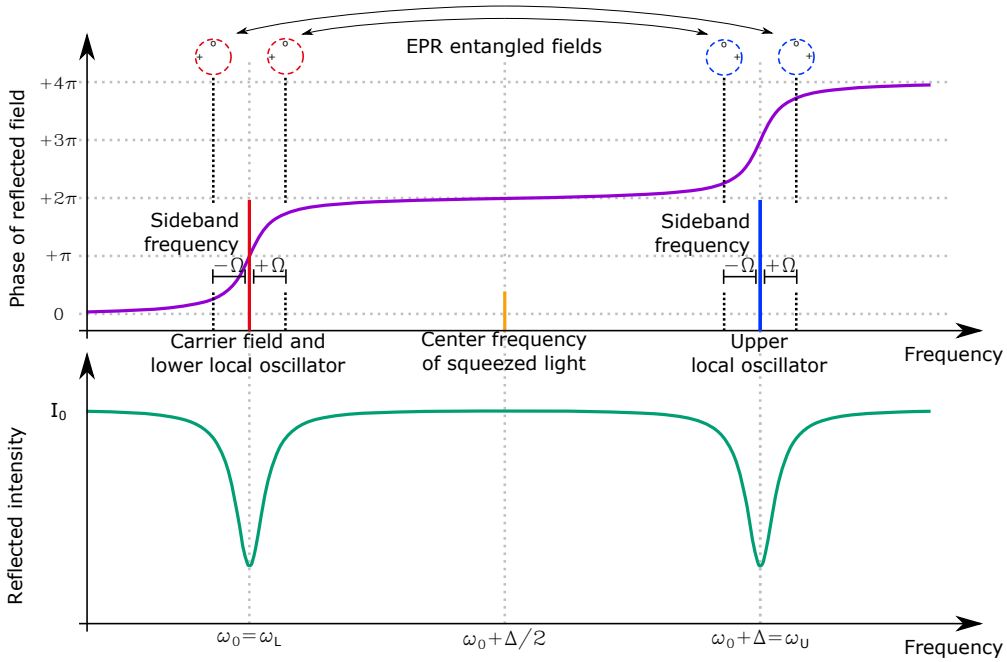

(a) Transfer function of the interferometer cavity and involved sideband frequencies without detuning.

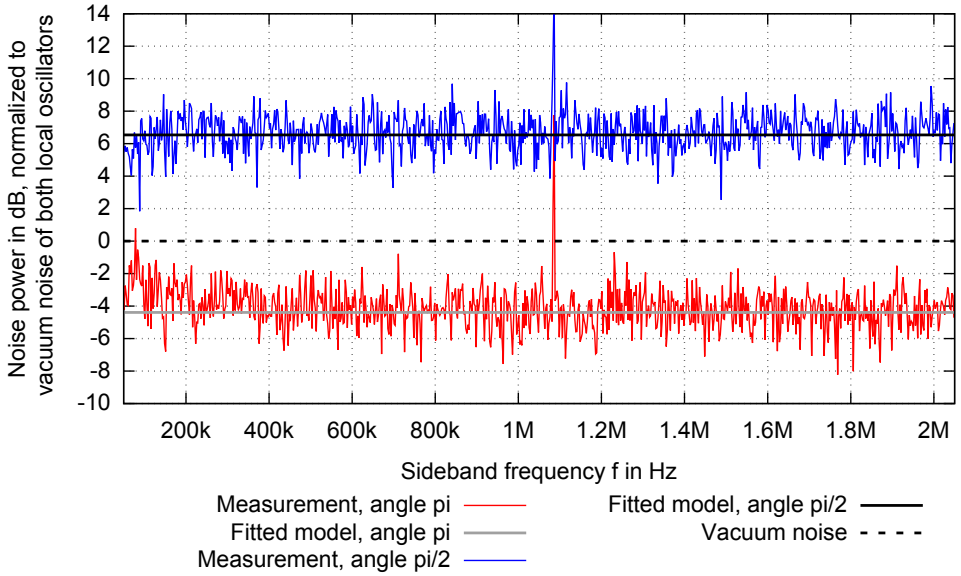

(b) Spectra of time traces with readout angles π and $\pi/2$

Figure 8.5: Transfer function of the interferometer cavity and involved sideband frequencies without detuning (subfigure **(a)**) and spectra of time traces as well as the fitted model for readout angles π and $\pi/2$ (subfigure **(b)**).

II(a). Bichromatic measurements of cavity-reflected EPR-entangled states with detuning of the upper local oscillator of $\delta_2 = 2\pi \cdot 400\,\mathrm{kHz}$

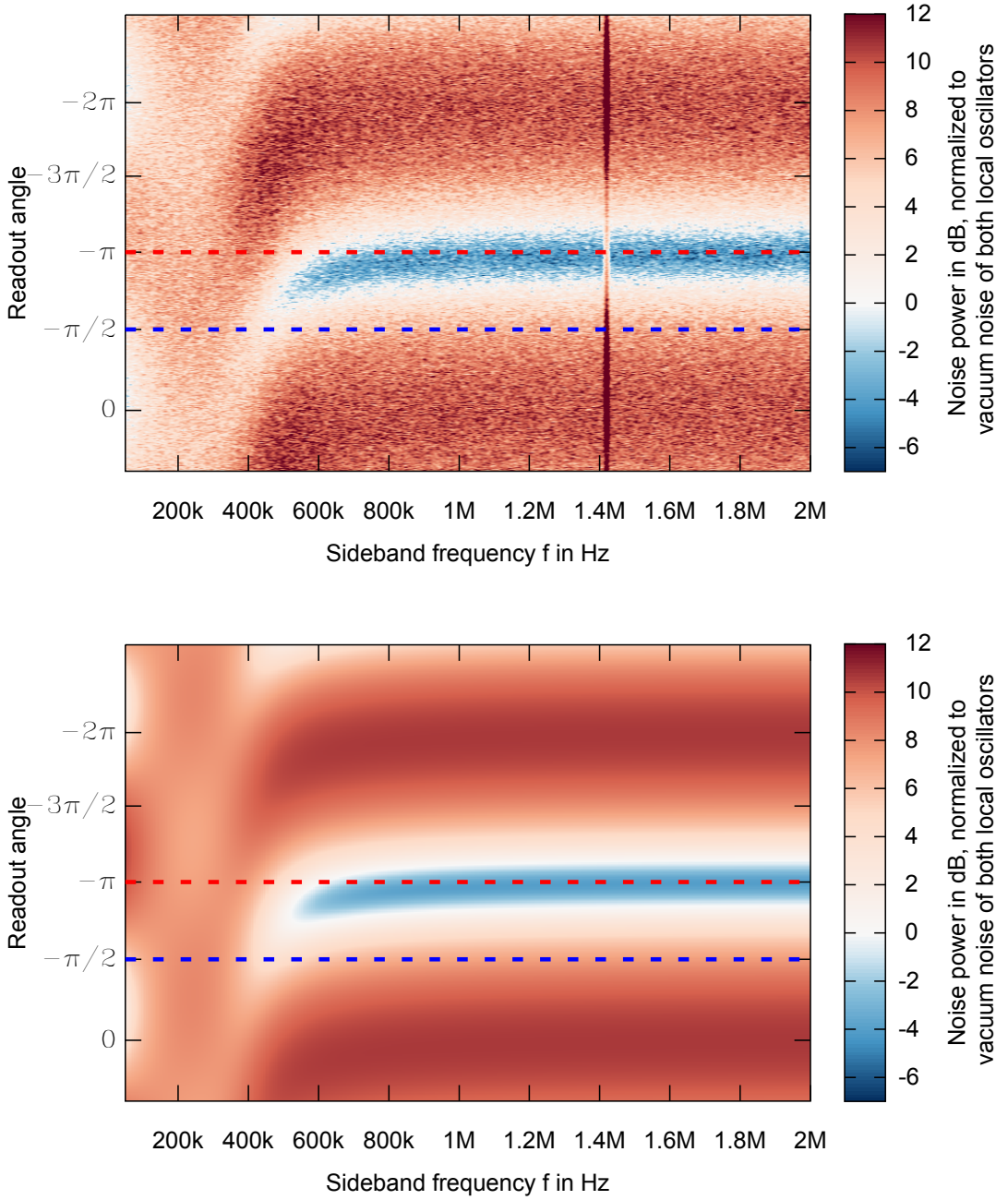

Figure 8.6: Spectrograms of measurements (upper subfigure) and fitted simulation (lower subfigure) with detuning of the upper local oscillator of $\delta_2 = 2\pi \cdot 400\,\mathrm{kHz}$. The quantum noise was frequency-dependent with a characteristic phase change around $f = 400\,\mathrm{kHz}$. The readout angle is inferred from the fitting data. Further details are given in the main text.

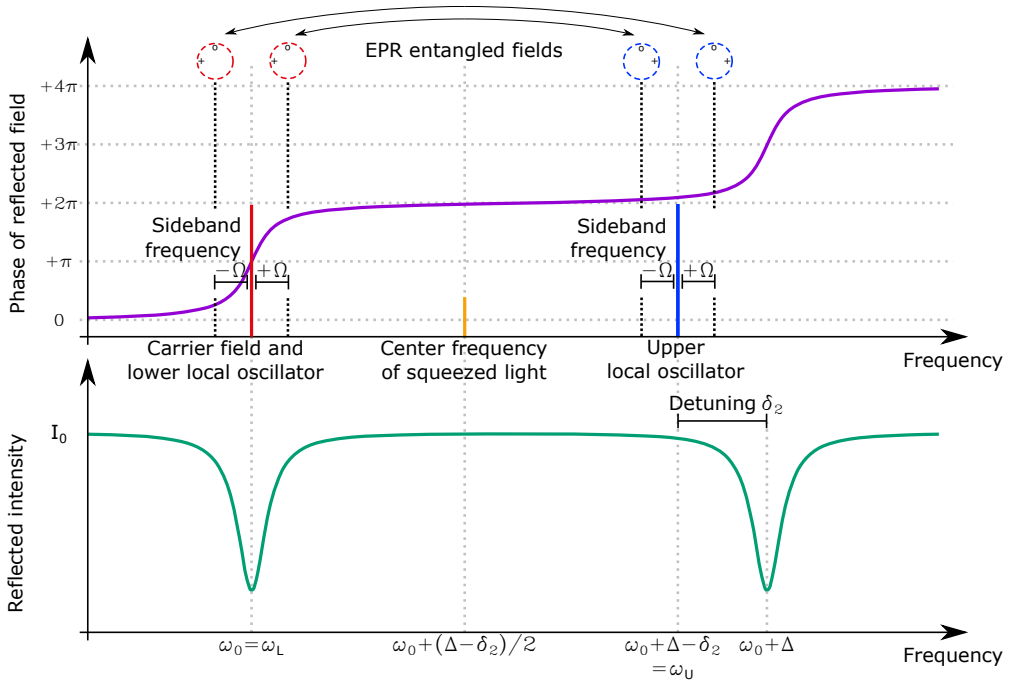

(a) Transfer function of the interferometer cavity and involved sideband frequencies with detuning of the upper local oscillator.

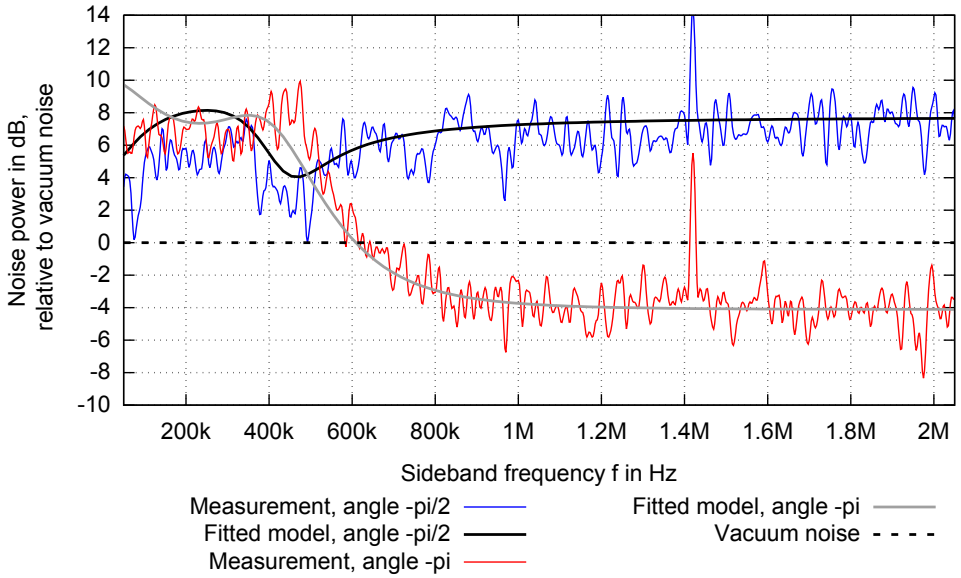

(b) Spectra of time traces with readout angles $\xi = -\pi$ and $\xi = -\pi/2$

Figure 8.7: Transfer function of the interferometer cavity and involved sideband frequencies with detuning of the upper local oscillator (subfigure **(a)**) and spectra of two time traces with the fitted model for readout angles $\xi = -\pi$ and $\xi = -\pi/2$ (subfigure **(b)**).

II(b). Bichromatic measurements of cavity-reflected EPR-entangled states with detuning of the upper local oscillator of $\delta_2 = 2\pi \cdot 4\,\mathrm{MHz}$

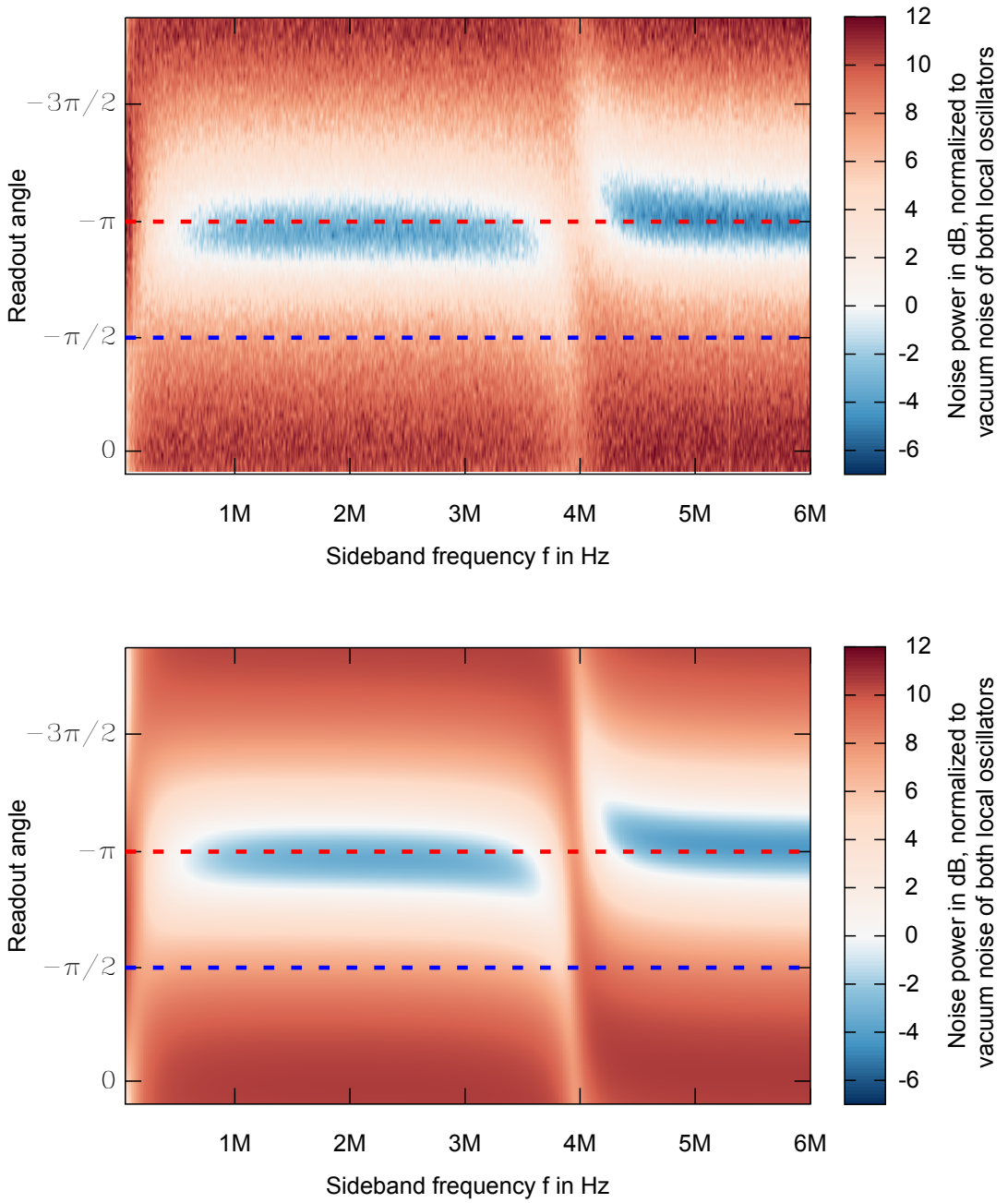

Figure 8.8: Spectrograms of measurements (upper subfigure) and fitted simulation (lower subfigure) with detuning of the upper local oscillator of $\delta_2 = 2\pi \cdot 4\,\mathrm{MHz}$. The quantum noise was frequency-dependent with a characteristic phase change around $f = 4\,\mathrm{MHz}$. The readout angle is inferred from the fitting data. Further details are given in the main text.

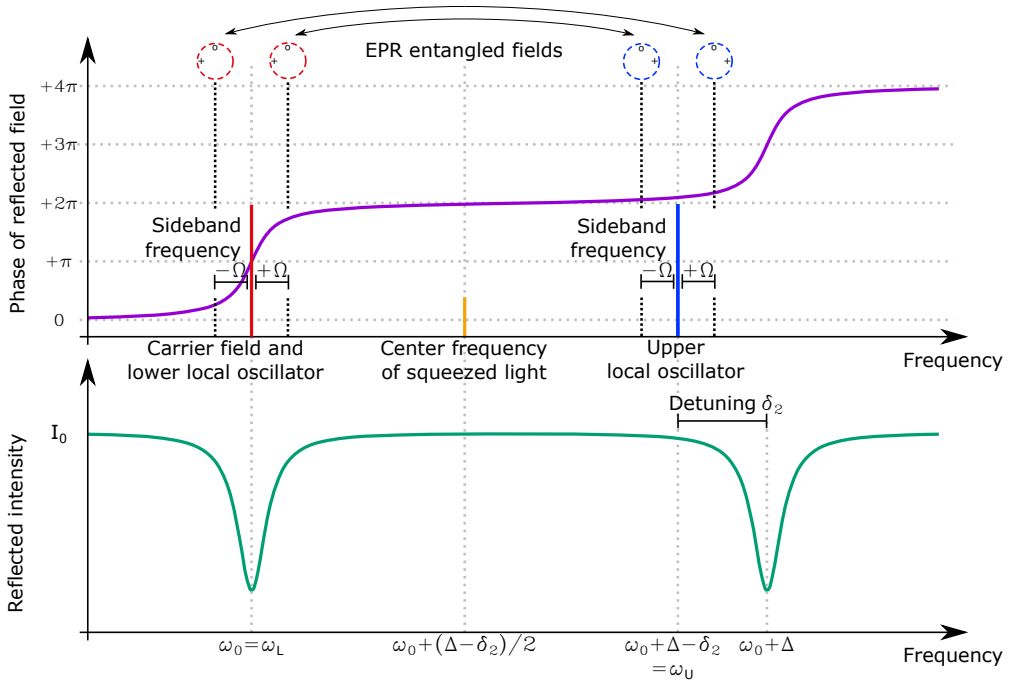

(a) Transfer function of the interferometer cavity and involved sideband frequencies with detuning of the upper local oscillator.

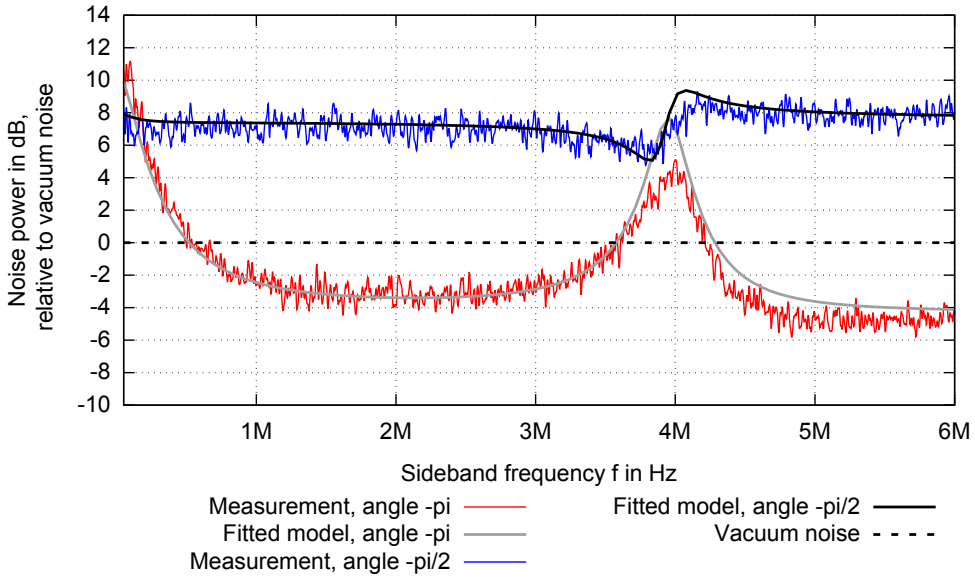

(b) Spectra of time traces with readout angles $\xi = -\pi$ and $\xi = -\pi/2$

Figure 8.9: Transfer function of the interferometer cavity and involved sideband frequencies with detuning of the upper local oscillator (subfigure **(a)**) and spectra of two time traces with the fitted model for readout angles $\xi = -\pi$ and $\xi = -\pi/2$ (subfigure **(b)**).

III. Bichromatic measurements of cavity-reflected EPR-entangled states with anti-symmetric detuning of both local oscillators of $2\pi \cdot 400\,\mathrm{kHz}$

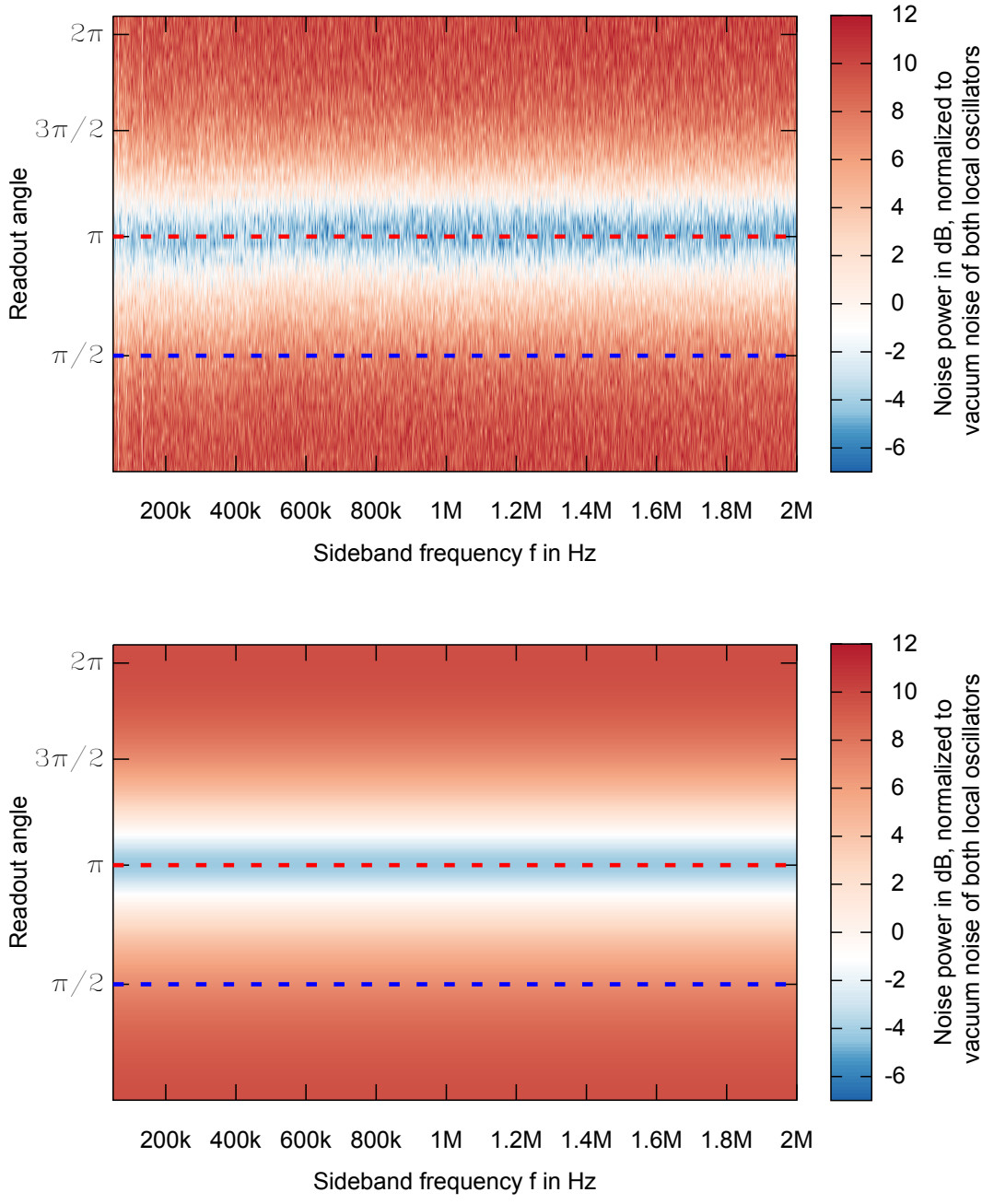

Figure 8.10: Spectrograms of measurements (upper subfigure) and fitted simulation (lower subfigure) with anti-symmetric detuning of both local oscillators $-\delta_1 = \delta_2 = 2\pi \cdot 400\,\mathrm{kHz}$. As in case **I**, the quantum noise was frequency-independent and for the readout angle of π a reduction below the vacuum noise was achieved. The readout angle is inferred from the fitting data. Further details are given in the main text.

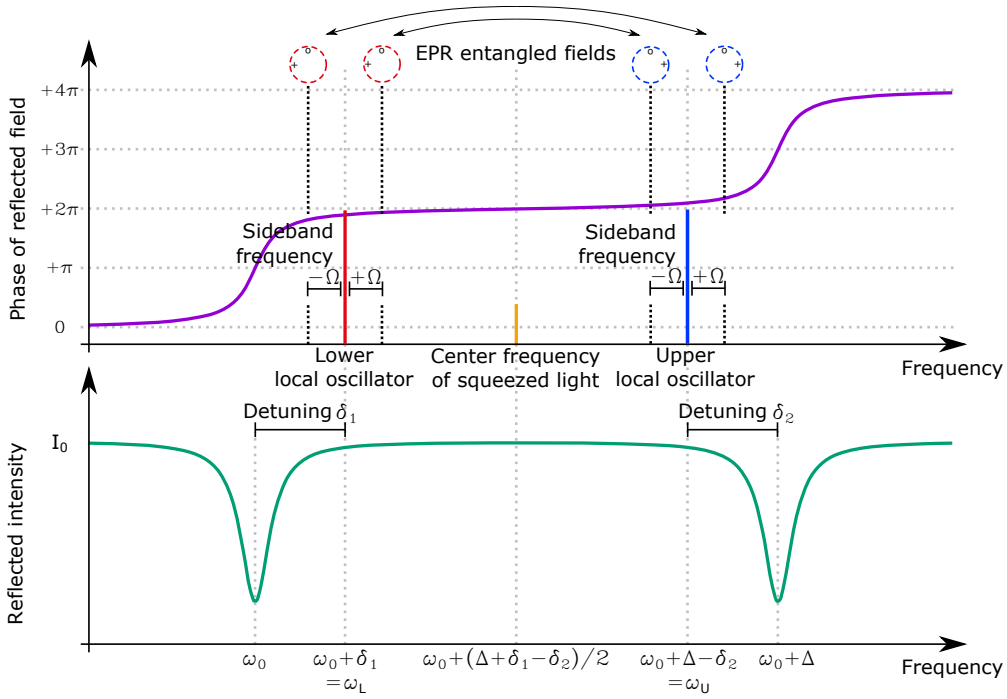

(a) Transfer function of the interferometer cavity and involved sideband frequencies with anti-symmetric detuning of both local oscillators.

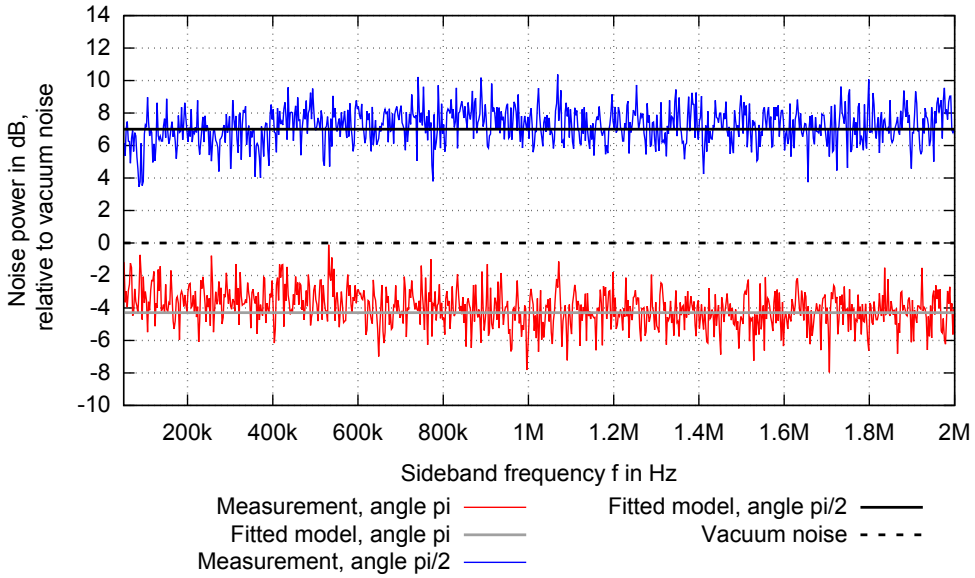

(b) Spectra of time traces with readout angles $\xi = \pi$ and $\xi = \pi/2$

Figure 8.11: Transfer function of the interferometer cavity and involved sideband frequencies with anti-symmetric detuning of both local oscillators (subfigure **(a)**) and spectra of two time traces with the fitted model for readout angles $\xi = \pi$ and $\xi = \pi/2$ (subfigure **(b)**).

IV(a). Bichromatic measurements of cavity-reflected EPR-entangled states with symmetric detuning of both local oscillators of $\delta_1 = \delta_2 = 2\pi \cdot 400\,\mathrm{kHz}$

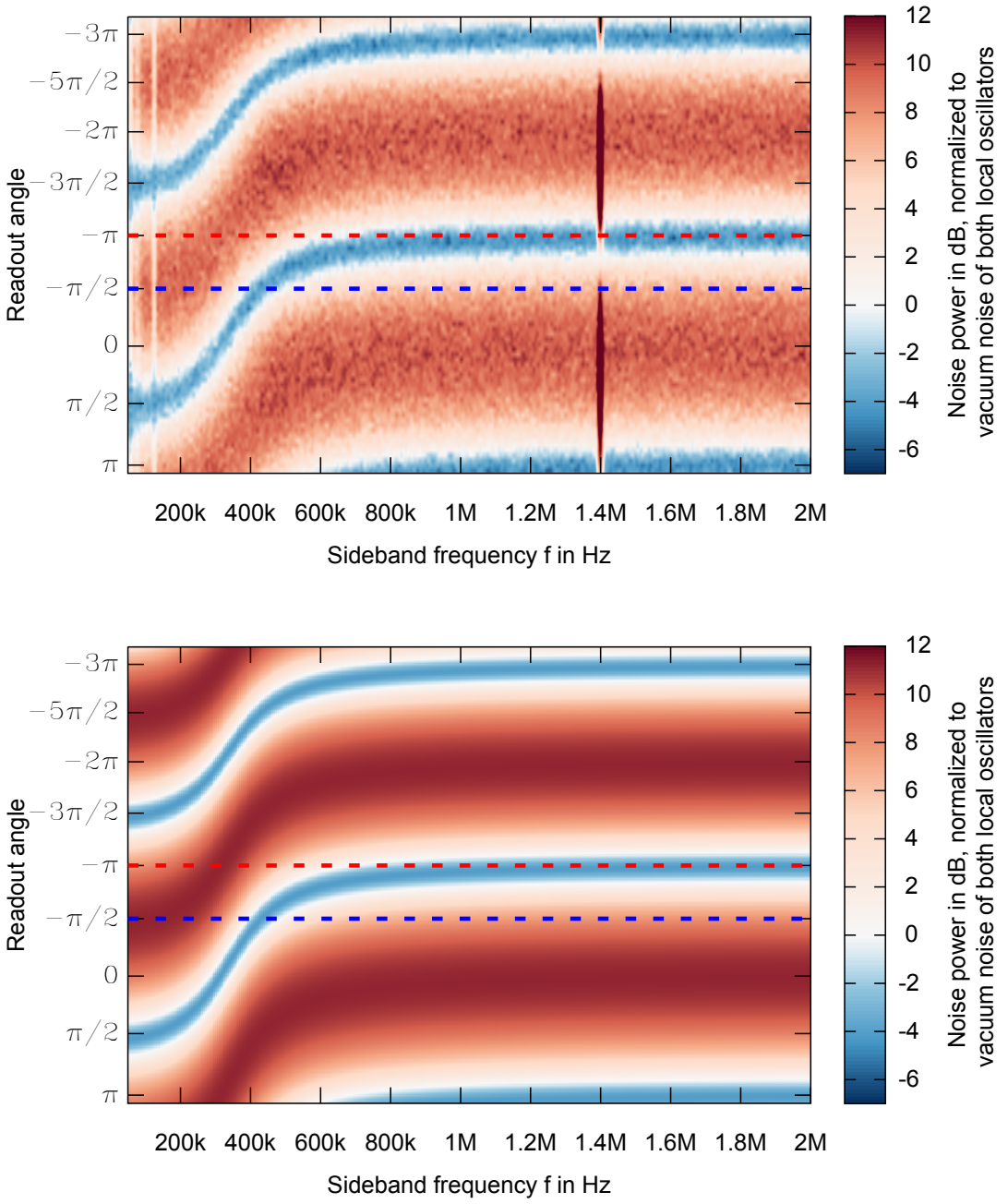

Figure 8.12: Spectrograms of measurements (upper subfigure) and fitted simulation (lower subfigure) with symmetric detuning of both local oscillators of $\delta_1 = \delta_2 = 2\pi{\cdot}400\,\mathrm{kHz}$. The quantum noise was frequency-dependently squeezed with a phase change around 400 kHz. The readout angle is inferred from the fitting data. Further details are given in the main text.

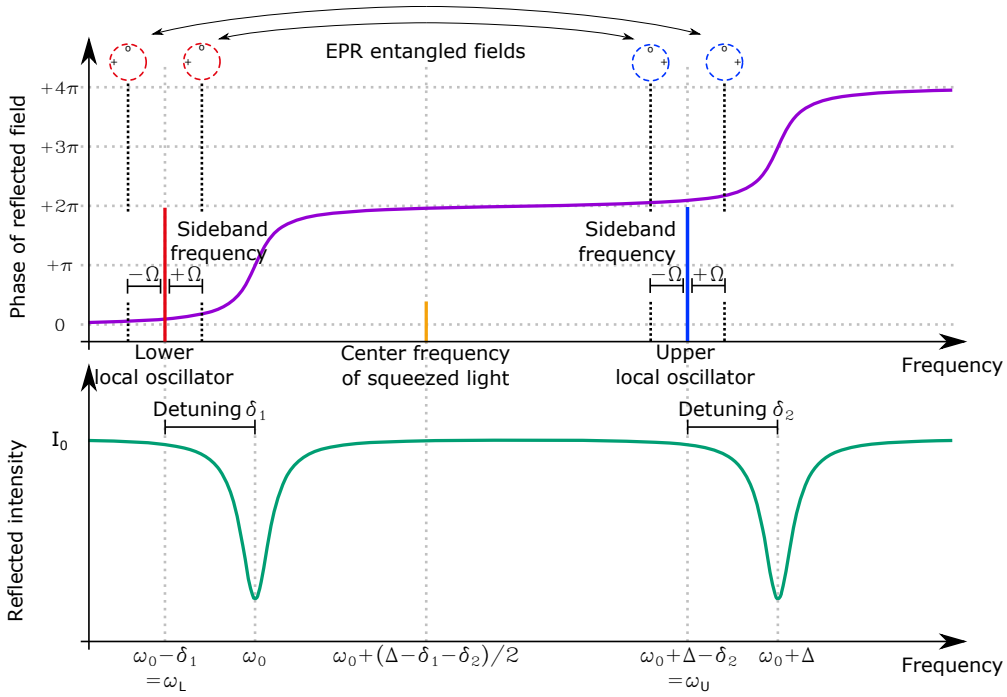

(a) Transfer function of the interferometer cavity and involved sideband frequencies with symmetric detuning of both local oscillators.

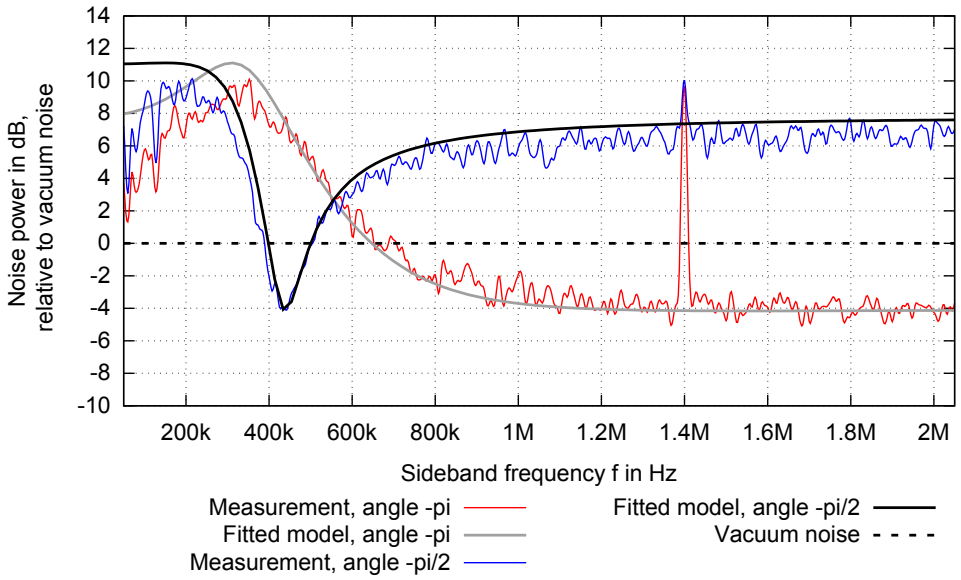

(b) Spectra of time traces with readout angles $\xi = -\pi$ and $\xi = -\pi/2$

Figure 8.13: Transfer function of the interferometer cavity and involved sideband frequencies with symmetric detuning of both local oscillators (subfigure **(a)**) and spectra of two time traces with the fitted model for readout angles $\xi = -\pi$ and $\xi = -\pi/2$ (subfigure **(b)**).

IV(b). Bichromatic measurements of cavity-reflected EPR-entangled states with symmetric detuning of both local oscillators of $\delta_1 = \delta_2 = 2\pi \cdot 1\,\mathrm{MHz}$

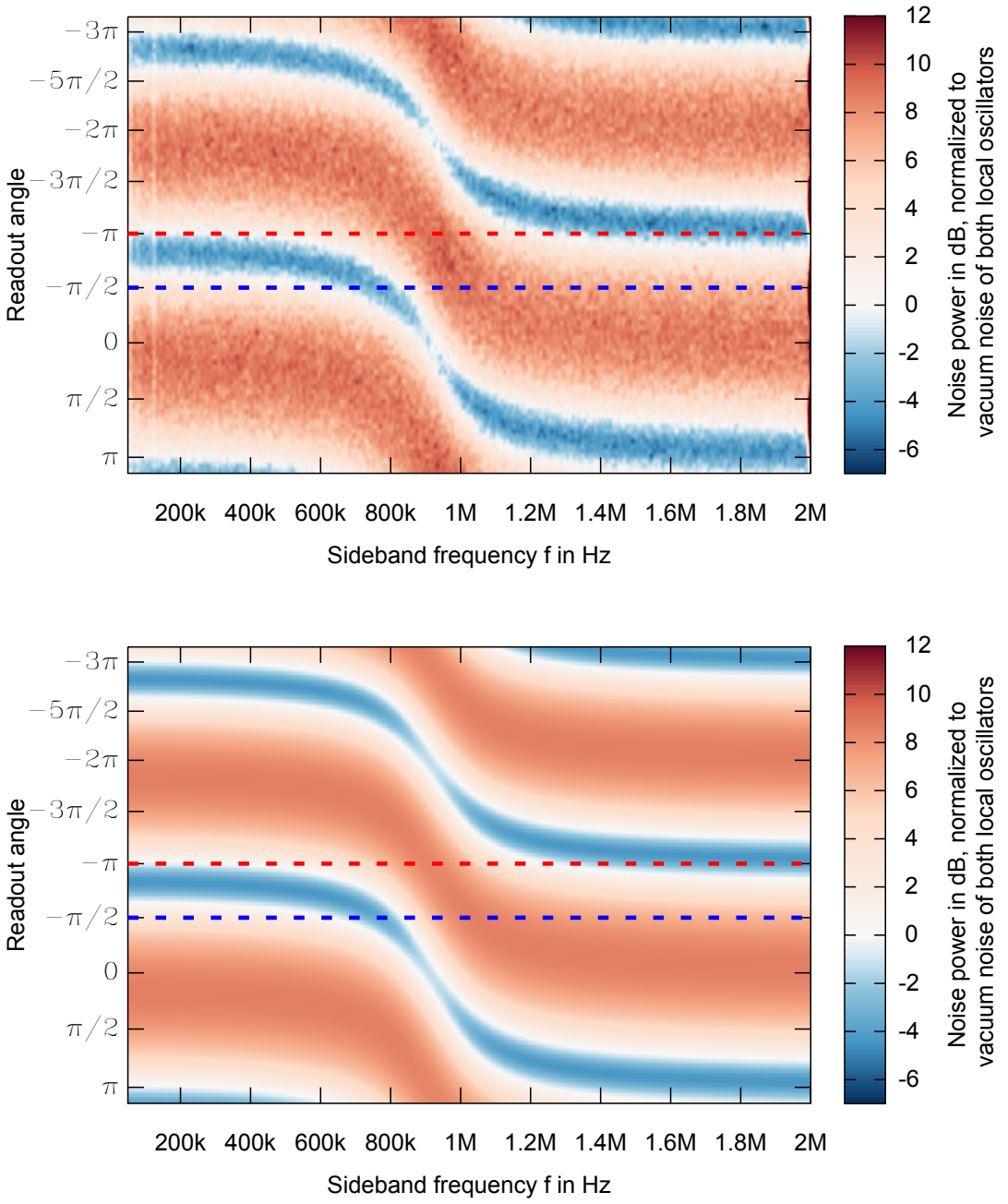

Figure 8.14: Spectrograms of measurements (upper subfigure) and fitted simulation (lower subfigure) with symmetric detuning of both local oscillators of $\delta_1 = \delta_2 = 2\pi \cdot 1\,\mathrm{MHz}$. The quantum noise was frequency-dependently squeezed with a phase change around 400 kHz. The readout angle is inferred from the fitting data. Further details are given in the main text.

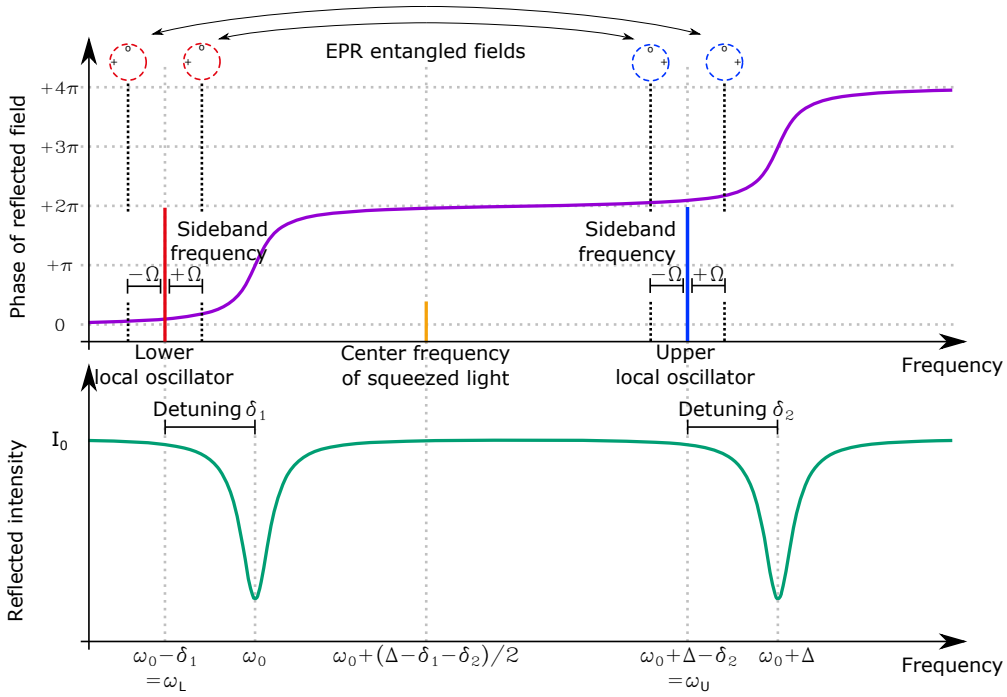

(a) Transfer function of the interferometer cavity and involved sideband frequencies with symmetric detuning of both local oscillators.

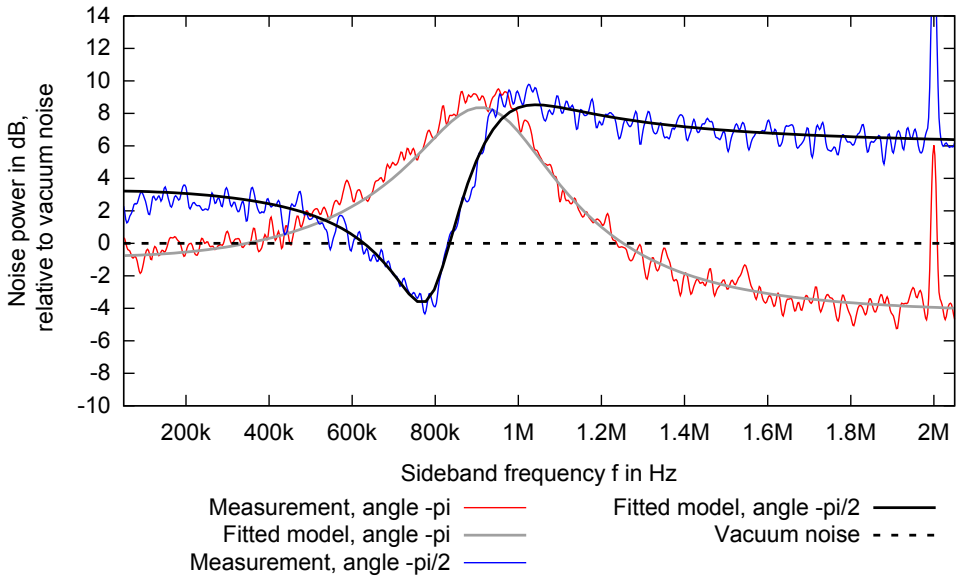

(b) Spectra of time traces with readout angles $\xi = -\pi$ and $\xi = -\pi/2$

Figure 8.15: Transfer function of the interferometer cavity and involved sideband frequencies with symmetric detuning of both local oscillators (subfigure **(a)**) and spectra of two time traces with the fitted model for readout angles $\xi = -\pi$ and $\xi = -\pi/2$ (subfigure **(b)**).

Set and fit parameters of the bichromatic measurements

In table 8.1 and 8.2 the fit parameters of equation (8.1) to the bichromatic measurements from chapter 8.3.3 are given. Table 8.1 is divided into parameters that I set in the model, (left column) and parameters for that the model was fitted to the data by a script written in *Python* (middle column). For the fit of the detuning values $\delta_{1,2}$, the expected values (as set in the experimental setup) are shown in the right column. The values α and β describing the relative amplitudes of the local oscillators are set to $\alpha = \beta = 1$ for all measurements. The half-width-half-maximum bandwidth of the interferometer cavity was set to $\gamma = 2\pi \cdot 125\,\mathrm{kHz}$ for all measurements. Table 8.2 shows the fitting parameters of the readout angle by the formula $\xi(t) = a + b \cdot t + c \cdot t^2$.

8.4 Conclusion

In this chapter I presented measurements on squeezed states with a bichromatic local oscillator readout scheme. In chapter 8.3.1 I sent squeezed states directly onto a homodyne detector with a bichromatic local oscillator. The resulting spectra of the measurements fit the theoretical model. The total loss of $\eta = 0.83$ is high compared to typical measurements of squeezed states. For future measurements the loss can be reduced by better modematching of the involved beams onto the reference cavity. In chapter 8.3.3 I demonstrated the interferometer-enhancement through EPR-entangled states. The measurements were performed for different settings of both the local oscillator frequencies with respect to the cavity resonances. All measurements are in good accordance with the model derived in chapter 8.1. Since the model is based on the same calculations as used in [Ma17], the experiment is a proof-of-principle for the proposal. The influence of the opto-mechanical coupling between the amplitude and the phase quadrature is only visible in high-power interferometers with free-falling test-masses, like in the LIGO detectors. Therefore, this could not be emulated with this setup.

Only towards lower frequencies, some measurements showed a deviation compared to the model that might be explained by the detector's design or imperfections in adjustments. For future experiments, either the detector can be improved to show less limitations at low frequencies and/or the cavity and local oscillator locks can be improved to be more stable. The detection efficiency in a range of $\eta = 0.65$ to $\eta = 0.71$ can be improved by achieving better mode matchings especially from the interferometer cavity to the reference cavity of the homodyne detector.

With these results we performed a proof-of-principle experiment for the proposals of [Ma17] and [Br17] on table-top scale. We set the path towards further investigations into this technique. By an implementation of these schemes in a

GW-detector prototype, the compatibility of the approach with a low-frequency suspended interferometer can be tested.

	Set parameters	Fit parameters Fit result	 Expected result
I.		**No detuning**	
	$\delta_1 = 0\,\mathrm{kHz}$	$r = 1.27$	
	$\delta_2 = 0\,\mathrm{kHz}$	$\eta = 0.69$	
II(a).		**Upper local oscillator detuned $\boldsymbol{\delta_2 = 2\pi \cdot 400\,\mathrm{kHz}}$**	
	$\delta_1 = 0\,\mathrm{kHz}$	$r = 1.42$	
		$\eta = 0.65$	
		$\delta_2 = 2\pi \cdot 399.9\,\mathrm{kHz}$	$\delta_2 = 2\pi \cdot 400\,\mathrm{kHz}$
II(b).		**Upper local oscillator detuned $\boldsymbol{\delta_2 = 2\pi \cdot 4\,\mathrm{MHz}}$**	
		$r = 1.40$	
		$\eta = 0.67$	
		$\delta_1 = -2\pi \cdot 74\,\mathrm{kHz}$	$\delta_1 = 0\,\mathrm{kHz}$
		$\delta_2 = 2\pi \cdot 3.95\,\mathrm{MHz}$	$\delta_2 = 2\pi \cdot 4\,\mathrm{MHz}$
III.		**Both local oscillators detuned anti-symmetrically $\boldsymbol{-\delta_1 = \delta_2 = 2\pi \cdot 400\,\mathrm{kHz}}$**	
	$\delta_1 = -2\pi \cdot 400\,\mathrm{kHz}$	$r = 1.29$	
	$\delta_2 = 2\pi \cdot 400\,\mathrm{kHz}$	$\eta = 0.69$	
IV(a).		**Both local oscillators detuned symmetrically $\boldsymbol{\delta_1 = \delta_2 = 2\pi \cdot 400\,\mathrm{kHz}}$**	
		$r = 1.48$	
		$\eta = 0.65$	
		$\delta_1 = 2\pi \cdot 339\,\mathrm{kHz}$	$\delta_1 = 2\pi \cdot 400\,\mathrm{kHz}$
		$\delta_2 = 2\pi \cdot 339\,\mathrm{kHz}$	$\delta_2 = 2\pi \cdot 400\,\mathrm{kHz}$
IV(b).		**Both local oscillators detuned symmetrically $\boldsymbol{\delta_1 = \delta_2 = 2\pi \cdot 1\,\mathrm{MHz}}$**	
		$r = 1.14$	
		$\eta = 0.71$	
		$\delta_1 = 2\pi \cdot 949\,\mathrm{kHz}$	$\delta_1 = 2\pi \cdot 1000\,\mathrm{kHz}$
		$\delta_2 = 2\pi \cdot 889\,\mathrm{kHz}$	$\delta_2 = 2\pi \cdot 1000\,\mathrm{kHz}$

Table 8.1: Set and fit parameters of bichromatic measurements of cavity-reflected EPR-entangled states for the different experimental steps. The parameters are the squeeze parameter r, the total detection efficiency η and the detuninigs $\delta_{1,2}$ of the lower and upper local oscillator.

	Fit parameters		
I.	**No detuning**		
	a = 6.53 rad	b = 12.71 rad/s	c = 6.43 rad/s^2
II(a).	**Upper local oscillator detuned $\delta_2 = 2\pi \cdot 400$ kHz**		
	a = 2.88 rad	b = −17.32 rad/s	c = −3.78 rad/s^2
II(b).	**Upper local oscillator detuned $\delta_2 = 2\pi \cdot 4$ MHz**		
	a = −0.40 rad	b = 20.58 rad/s	c = −2.37 rad/s^2
III.	**Both local oscillators detuned anti-symmetrically $-\delta_1 = \delta_2 = 2\pi \cdot 400$ kHz**		
	a = −0.72 rad	b = 14.86 rad/s	c = 21.04 rad/s^2
IV(a).	**Both local oscillators detuned symmetrically $\delta_1 = \delta_2 = 2\pi \cdot 400$ kHz**		
	a = 5.72 rad	b = −23.87 rad/s	c = −9.78 rad/s^2
IV(b).	**Both local oscillators detuned symmetrically $\delta_1 = \delta_2 = 2\pi \cdot 1$ MHz**		
	a = 0.32 rad	b = 24.66 rad/s	c = 7.7 rad/s^2

Table 8.2: Fit parameters of the readout angles of bichromatic measurements of cavity-reflected EPR-entangled states for the different experimental steps. The readout angle of each measurement was fitted with the function $\xi(t) = a + b \cdot t + c \cdot t^2$

CHAPTER 9

Summary and outlook

Compact sources of squeezed states are important for flexible applications in the future. During this work, I planned, assembled and characterized a source of squeezed states of light at 1064 nm on a breadboard with a footprint of $0.8\,\mathrm{m}^2$. This size was reached by an optimized arranging of standard-sized optical components. The source produced squeezed states with a noise power in the squeezed quadrature of $10.7\,\mathrm{dB} \pm 0.2\,\mathrm{dB}$ below the vacuum noise power at the sideband frequency of 5 MHz. The corresponding anti-squeezed quadrature showed a noise power $15\,\mathrm{dB} \pm 0.2\,\mathrm{dB}$ above the vacuum noise. The total loss was $5.7\,\% \pm 0.5\,\%$. In measurements of the spectrum of the noise power a reduction below the vacuum noise was shown between sideband frequencies of 70 kHz and 65 MHz. This source was already used in a downstream, opto-mechanical experiment and can be used in further quantum-noise-limited experiments. The setup allows for a future integration of a coherent control lock. A further decrease of the footprint is mainly limited by the size of the optical components. Especially by using smaller modecleaner cavities and mirror holders, the footprint can be decreased by a factor of two. Due to the loss of $5.7\,\% \pm 0.5\,\%$ as squeeze factor of 12.7 dB is reachable by improved phase-matching temperatures.

Measurements by balanced homodyne detection in the audio band and their enhancement through squeezed light are challenging due to technical reasons. In this work I presented the experimental realization of a squeezed-light-enhanced interferometer at low frequencies by heterodyne detection and detuned, high-frequency squeezed states. A 2.5 m-linear cavity emulated an interferometer cavity. Here, the center frequency of the squeezed light was centered in the middle between to adjacent resonances of the interferometer cavity. A bright field at

the same frequency served as a local oscillator in a balanced heterodyne readout of a signal that was produced at low frequencies by modulation of the cavity length. The measurements at the signal frequencies were conditionally improved by the entangled sidebands of the squeezed field. This detection scheme suffers a 3 dB penalty compared to conventional squeezed-light enhancement. We showed a double-sided noise spectrum as directly measured in the heterodyne detection and a single-sided spectrum by electronic demodulation. In both measurements an improvement in the signal-to-noise ratio of $3.4\,\mathrm{dB} \pm 0.3\,\mathrm{dB}$ was achieved. By this we have a higher improvement then 3 dB and can show an improvement compared to no application of squeezed light. The measurements were mainly limited by optical loss and a low darknoise clearance of the detector. By reducing these limitations higher improvements are reachable. Technical noise on the carrier field kept us from setting the signal frequency lower. By reducing this noise a lower signal frequency is achievable. We suggest this scheme to be used in experiments where a homodyne detection at low frequencies is not possible due to technical limitations or the generation of squeezed states at these frequencies is not feasible.

The application of squeezed-states of light has been proven to decrease quantum noise in gravitational-wave detectors. However, for achieving a broadband quantum-noise reduction the squeezed quadrature needs to be rotated frequency-dependently. So far, the implementation of cost-intensive, additional filter cavities with a length in the order of 100 m is considered for this rotation. Ma et al. proposed using the signal-recycling cavity together with an application of detuned squeezed states and a conditional readout scheme with two balanced homodyne detectors to avoid these cavities. In this work, I presented an experimental realization of the proposed schemes in a table-top experiment. A 2.5 m-linear cavity emulated an interferometer cavity. Squeezed states were generated detuned to the carrier frequency of the cavity. For the readout we built a bichromatic homodyne detector. This allowed conditional measurements between the two local oscillators with a single detector. We derived a mathematical model describing the measured noise spectra that is based on the theory used in the proposal of Ma et al. In a first measurement we set both local oscillators to be resonant for the cavity resulting in frequency-independent noise spectra. Afterwards, we detuned the upper local oscillator and introduced a frequency-dependent quantum noise comparable to opto-mechanical coupling. The resulting noise spectra can be well explained by our theoretical model. Due to the limitations of a table-top setup, we can not directly show the influence of the opto-mechanical coupling to the rotation of the squeezed-angle as expected in gravitational-wave detectors. By detuning the lower local oscillator anti-symmetrically, we showed a compensation of the frequency-dependent noise leading back to frequency-independent noise spectra. By this we can show the potential of the proposal by Ma et al. Additionally, this allows a broadband reduction of quantum noise in gravitational-wave detec-

tors with a detuned signal-recycling cavity. In a fourth step, we detuned the local oscillators symmetrically and achieved frequency-dependent noise spectra. With this step we can show that the quantum correlations were retained over the whole detection range. All measurements can be well explained by our theoretical model. The measurements were mainly limited by the mode matching from the interferometer cavity to the homodyne detection. With these results we performed a proof-of-principle experiment the proposals of [Ma17] and [Br17] on table-top scale and set the path towards further investigations into this technique. By an implementation of these schemes in a GW-detector prototype, the compatibility of the approach with a low-frequency suspended interferometer can be tested. Additionally, in future experiments a focus needs to be put on the signal. Here, no signal was introduced but in gravitational-wave detectors the readout angles need to be optimized with respect to a given signal.

APPENDIX A

Theoretical model of cavity-reflected squeezed states

A.1 Calculations

This section gives a detailed theoretical description of the noise spectra of initially frequency-independent squeezed states being reflected off a cavity and read out by a bichromatic local oscillator. The formalism is similar to the description used in [Ma17] and was derived by Mikhail Korobko.

The parametric down-conversion process, squeezing the phase quadrature of the light field, transforms the input field at sideband frequencies $\omega \pm \Omega$

$$\hat{d}_{\mathrm{out}}(\omega+\Omega) = \hat{d}_{\mathrm{in}}(\omega+\Omega)\cosh r + \hat{d}^{\dagger}_{\mathrm{in}}(\omega-\Omega)\sinh r\,, \tag{A.1}$$

$$\hat{d}^{\dagger}_{\mathrm{out}}(\omega-\Omega) = \hat{d}^{\dagger}_{\mathrm{in}}(\omega-\Omega)\cosh r + \hat{d}_{\mathrm{in}}(\omega+\Omega)\sinh r\,. \tag{A.2}$$

In terms of two-photon quadrature operators, defined by [Ca81]

$$\hat{d}_1(\Omega) = \frac{\hat{d}(\omega+\Omega)+\hat{d}^{\dagger}(\omega-\Omega)}{\sqrt{2}}, \quad \hat{d}_2(\Omega) = \frac{\hat{d}(\omega+\Omega)-\hat{d}^{\dagger}(\omega-\Omega)}{i\sqrt{2}} \tag{A.3}$$

the squeezing relation can be simply expressed as

$$\hat{d}_{\mathrm{out},1}(\Omega) = \hat{d}_{\mathrm{in},1}(\Omega)e^{r}, \quad \hat{d}_{\mathrm{out},2}(\Omega) = \hat{d}_{\mathrm{in},2}(\Omega)e^{-r}\,. \tag{A.4}$$

In the case described in [Ma17] the frequencies of interest are not centered around ω, but rather around two frequencies ω_0 and $\omega_0 + \Delta$. We can define new fields $\hat{a}(\omega_0+\Omega') \equiv \hat{d}(\omega-\Omega)$ and $\hat{b}(\omega_0+\Delta+\Omega') \equiv \hat{d}(\omega+\Omega)$, and re-write

equations (A.1) and (A.2) as

$$\hat{a}(\omega_0+\Omega) = \hat{a}_{\mathrm{in}}(\omega_0+\Omega)\cosh r + \hat{b}^{\dagger}_{\mathrm{in}}(\omega_0+\Delta-\Omega)\sinh r\,, \tag{A.5}$$

$$\hat{a}^{\dagger}(\omega_0-\Omega) = \hat{a}^{\dagger}_{\mathrm{in}}(\omega_0-\Omega)\cosh r + \hat{b}_{\mathrm{in}}(\omega_0+\Delta+\Omega)\sinh r\,, \tag{A.6}$$

$$\hat{b}(\omega_0+\Delta+\Omega) = \hat{b}_{\mathrm{in}}(\omega_0+\Delta+\Omega)\cosh r + \hat{a}^{\dagger}_{\mathrm{in}}(\omega_0-\Omega)\sinh r\,, \tag{A.7}$$

$$\hat{b}^{\dagger}(\omega_0+\Delta-\Omega) = \hat{b}^{\dagger}_{\mathrm{in}}(\omega_0+\Delta-\Omega)\cosh r + \hat{a}_{\mathrm{in}}(\omega_0+\Omega)\sinh r\,. \tag{A.8}$$

These equations in terms of two-photon quadratures reduce to:

$$\begin{bmatrix}\hat{a}_1(\Omega)\\ \hat{a}_2(\Omega)\end{bmatrix} = \mathbb{S}\begin{bmatrix}\hat{a}_{\mathrm{in},1}(\Omega)\\ \hat{b}_{\mathrm{in},2}(\Omega)\end{bmatrix}\,, \tag{A.9}$$

$$\begin{bmatrix}\hat{b}_1(\Omega)\\ \hat{b}_2(\Omega)\end{bmatrix} = \mathbb{S}\begin{bmatrix}\hat{b}_{\mathrm{in},1}(\Omega)\\ \hat{a}_{\mathrm{in},2}(\Omega)\end{bmatrix}\,, \tag{A.10}$$

$$\tag{A.11}$$

with the squeezing matrix defined as

$$\mathbb{S} = \begin{bmatrix}\cosh r & \sinh r\\ \cosh r & -\sinh r\end{bmatrix}\,. \tag{A.12}$$

The transfer function of a cavity with natural half-width-half-maximum linewidth γ for the frequency ω reads

$$\hat{d}_{\mathrm{out}}(\omega) = -\frac{\omega-\omega_{\mathrm{c}}-i\gamma}{\omega-\omega_{\mathrm{c}}+i\gamma}\hat{d}_{\mathrm{in}}(\omega)\,, \tag{A.13}$$

where ω_{c} is the resonance frequency of the cavity. For the sidebands of the main beam, that is detuned from the cavity resonance by δ it takes a form

$$\hat{d}_{\mathrm{out}}(\omega\pm\Omega) = -\frac{\delta\pm\Omega-i\gamma}{\delta\pm\Omega+i\gamma}\hat{d}_{\mathrm{in}}(\omega\pm\Omega) = \mathcal{R}(\pm\Omega+\delta)\hat{d}_{\mathrm{in}}(\omega\pm\Omega)\,, \tag{A.14}$$

and in two-mode picture it is transformed into

$$\begin{bmatrix}\hat{d}_{\mathrm{out},1}(\Omega)\\ \hat{d}_{\mathrm{out},2}(\Omega)\end{bmatrix} = \mathbb{R}(\Omega,\delta)\begin{bmatrix}\hat{d}_{\mathrm{in},1}(\Omega)\\ \hat{d}_{\mathrm{in},2}(\Omega)\end{bmatrix}\,, \tag{A.15}$$

where we introduced a reflection matrix

$$\mathbb{R}(\Omega,\delta) = \frac{2\gamma}{(\gamma-i\Omega)^2+\delta^2}\begin{bmatrix}\gamma-i\Omega & -\delta\\ \delta & \gamma-i\Omega\end{bmatrix} - \begin{bmatrix}1 & 0\\ 0 & 1\end{bmatrix}\,. \tag{A.16}$$

With this definition in mind, and writing for simplicity the quadrature vector as $\hat{\mathbf{d}}(\Omega) = \{\hat{d}_1(\Omega), \hat{d}_2(\Omega)\}^{\mathrm{T}}$, we can write down the input-output relation in terms

of quadratures

$$\hat{\mathbf{a}}_{\text{out}}(\Omega) = \mathbb{R}(\Omega,\delta_1)\hat{\mathbf{a}}(\Omega) = \mathbb{R}(\Omega,\delta_1)\mathbb{S}\begin{bmatrix}\hat{a}_{\text{in},1}(\Omega)\\ \hat{b}_{\text{in},2}(\Omega)\end{bmatrix}, \tag{A.17}$$

$$\hat{\mathbf{b}}_{\text{out}}(\Omega) = \mathbb{R}(\Omega,\delta_2)\hat{\mathbf{b}}(\Omega) = \mathbb{R}(\Omega,\delta_2)\mathbb{S}\begin{bmatrix}\hat{b}_{\text{in},1}(\Omega)\\ \hat{a}_{\text{in},2}(\Omega)\end{bmatrix}. \tag{A.18}$$

The homodyne detection with two LO beams of powers α,β is given by

$$y = \frac{\alpha}{\sqrt{\alpha^2+\beta^2}}\mathbb{H}(\zeta)\hat{\mathbf{a}}_{\text{out}}(\Omega) + \frac{\beta}{\sqrt{\alpha^2+\beta^2}}\mathbb{H}(\chi)\hat{\mathbf{b}}_{\text{out}}(\Omega), \tag{A.19}$$

where the homodyne detection vector is $\mathbb{H}(\phi) = \{\cos\phi, \sin\phi\}, \forall\phi$. When the detection efficiency is reduced, as modeled by a beam-splitter with power transmissivity η, the homodyne output is changed

$$\tilde{y} = \sqrt{\eta}y + \sqrt{1-\eta}v, \tag{A.20}$$

where v is vacuum noise.

We define the spectral density of the field $\hat{a}(\Omega)$ as

$$S_{\text{a}}(\Omega)\delta(\Omega-\Omega') = \frac{1}{2}\left\langle \hat{a}(\Omega)\hat{a}(\Omega') + \hat{a}(\Omega')\hat{a}(\Omega)\right\rangle, \tag{A.21}$$

and for vacuum fields it's $S_{\text{v}}(\Omega) = 1$. This allows us to finally write down the spectral density of the output signal as:

$$\begin{aligned} S_{\tilde{y}}(\Omega) = 1 - \eta &+ \eta\frac{\alpha^2}{\alpha^2+\beta^2}\mathbb{H}(\zeta)(\Omega)\mathbb{R}(\Omega,\delta_1)\mathbb{S}\mathbb{I}\mathbb{S}^\dagger\mathbb{R}^\dagger(\Omega,\delta_1)\mathbb{H}(\zeta)^{\text{T}} + \\ &+ \eta\frac{\beta^2}{\alpha^2+\beta^2}\mathbb{H}(\chi)(\Omega)\mathbb{R}(\Omega,\delta_2)\mathbb{S}\mathbb{I}\mathbb{S}^\dagger\mathbb{R}^\dagger(\Omega,\delta_2)\mathbb{H}(\chi)^{\text{T}} + \\ &+ \eta\frac{\alpha\beta}{\alpha^2+\beta^2}\mathbb{H}(\zeta)(\Omega)\mathbb{R}(\Omega,\delta_1)\mathbb{S}\mathbb{I}\mathbb{S}^\dagger\mathbb{R}^\dagger(\Omega,\delta_2)\mathbb{H}(\chi)^{\text{T}} + \\ &+ \eta\frac{\alpha\beta}{\alpha^2+\beta^2}\mathbb{H}(\chi)(\Omega)\mathbb{R}(\Omega,\delta_2)\mathbb{S}\mathbb{I}\mathbb{S}^\dagger\mathbb{R}^\dagger(\Omega,\delta_1)\mathbb{H}(\zeta)^{\text{T}}, \end{aligned} \tag{A.22}$$

where $\mathbb{I} = \{\{1,0\},\{0,1\}\}$ is the unity matrix. This gives the final spectral density:

$$\begin{aligned} S_{\text{yy}} =& 1 - \eta + \eta\cosh(2r) + 2\alpha\beta\eta\sinh(2r)\cdot \\ &\left[\left(\gamma^4 + (\delta_1^2-\Omega^2)(\delta_2^2-\Omega^2) - \gamma^2(\delta_1^2+\delta_2^2-2\Omega^2+4\delta_1\delta_2)\right)\cos(\xi)\right. \\ &\left. + 2\gamma(\delta_1+\delta_2)(\gamma^2-\delta_1\delta_2+\Omega^2)\sin(\xi)\right]\cdot \\ &\frac{\left[\gamma^4 + (\delta_1^2-\Omega^2)(\delta_2^2-\Omega^2) + \gamma^2(\delta_1^2+\delta_2^2+2\Omega^2)\right]}{(\alpha^2+\beta^2)(\gamma^2+(\delta_1-\Omega)^2)(\gamma^2+(\delta_2-\Omega)^2)(\gamma^2+(\delta_1+\Omega)^2)(\gamma^2+(\delta_2+\Omega)^2)}. \end{aligned} \tag{A.23}$$

A.2 *Mathematica* notebook of the theoretical model

Equations

$$T0p = -\frac{\Omega + \delta 1 - i\gamma}{\Omega + \delta 1 + i\gamma};$$

$$T0m = -\frac{-\Omega + \delta 1 + i\gamma}{-\Omega + \delta 1 - i\gamma};$$

$$Tp = -\frac{\Omega + \delta 2 - i\gamma}{\Omega + \delta 2 + i\gamma};$$

$$Tm = -\frac{-\Omega + \delta 2 + i\gamma}{-\Omega + \delta 2 - i\gamma};$$

```
ap = Cosh[r] ainp + Sinh[r] binm;
amd = Cosh[r] ainm + Sinh[r] binp;
bp = Cosh[r] binp + Sinh[r] ainm;
bmd = Cosh[r] binm + Sinh[r] ainp;
```

$$a1 = \frac{1}{\sqrt{2}} (T0p\ ap + T0m\ amd);$$

$$a2 = \frac{1}{i\sqrt{2}} (T0p\ ap - T0m\ amd);$$

$$b1 = \frac{1}{\sqrt{2}} (Tp\ bp + Tm\ bmd);$$

$$b2 = \frac{1}{i\sqrt{2}} (Tp\ bp - Tm\ bmd);$$

$$y = \frac{\alpha}{\sqrt{\alpha^2 + \beta^2}} (a1\ \text{Cos}[\xi] + a2\ \text{Sin}[\xi]) + \frac{\beta}{\sqrt{\alpha^2 + \beta^2}} (b1\ \text{Cos}[\chi] + b2\ \text{Sin}[\chi])$$

```
// FullSimplify;

Kap = Coefficient[y, {ainp}][[1]] // FullSimplify;
Kam = Coefficient[y, {ainm}][[1]] // FullSimplify;
Kbp = Coefficient[y, {binp}][[1]] // FullSimplify;
Kbm = Coefficient[y, {binm}][[1]] // FullSimplify;

y
```

$$\frac{1}{\sqrt{2}\ \sqrt{\alpha^2 + \beta^2}} \left(\frac{1}{\delta 2^2 + (\gamma - i\Omega)^2} e^{-i\chi} \beta \left(\left((\gamma + i\delta 2)^2 + \Omega^2 \right) (\text{binp Cosh}[r] + \text{ainm Sinh}[r]) + e^{2i\chi} \left((\gamma - i\delta 2)^2 + \Omega^2 \right) (\text{binm Cosh}[r] + \text{ainp Sinh}[r]) \right) + \frac{1}{\delta 1^2 + (\gamma - i\Omega)^2} e^{-i\xi} \alpha \left(\left((\gamma + i\delta 1)^2 + \Omega^2 \right) (\text{ainp Cosh}[r] + \text{binm Sinh}[r]) + e^{2i\xi} \left((\gamma - i\delta 1)^2 + \Omega^2 \right) (\text{ainm Cosh}[r] + \text{binp Sinh}[r]) \right) \right)$$

Resulting spectral density

```
Sd = (Kap Kap- + Kam Kam- + Kbp Kbp- + Kbm Kbm-) η + (1 - η) // ComplexExpand //
  FullSimplify
```

$$1-\eta+\eta\,\text{Cosh}[2\,r]+\Big(2\,\alpha\,\beta\,\eta\,\Big(\gamma^4+(\delta1-\Omega)\,(\delta2-\Omega)\,(\delta1+\Omega)\,(\delta2+\Omega)+\gamma^2\,\Big(\delta1^2+\delta2^2+2\,\Omega^2\Big)\Big)\Big(\Big(\gamma^4+(\delta1-\Omega)\,(\delta2-\Omega)\,(\delta1+\Omega)\,(\delta2+\Omega)-\gamma^2\,\Big(\delta1^2+4\,\delta1\,\delta2+\delta2^2-2\,\Omega^2\Big)\Big)\,\text{Cos}[\xi+\chi]+2\,\gamma\,(\delta1+\delta2)\,\Big(\gamma^2-\delta1\,\delta2+\Omega^2\Big)\,\text{Sin}[\xi+\chi]\Big)\,\text{Sinh}[2\,r]\Big)\Big/\Big(\Big(\alpha^2+\beta^2\Big)\,\Big(\gamma^2+(\delta1-\Omega)^2\Big)\,\Big(\gamma^2+(\delta2-\Omega)^2\Big)\,\Big(\gamma^2+(\delta1+\Omega)^2\Big)\,\Big(\gamma^2+(\delta2+\Omega)^2\Big)\Big)$$

Bibliography

[Aa15] J. Aasi et al. *Advanced LIGO*, Class. Quantum Grav. **32** 074001 pp.41 (2015)

[Ab16a] B. P. Abbott et al. (LIGO Scientific Collaboration and Virgo Collaboration) *Observation of Gravitational Waves from a Binary Black Hole Merger* Phys. Rev. Lett. **116**, 061102 (2016)

[Ab16b] B. P. Abbott et al. (LIGO Scientific Collaboration and Virgo Collaboration) *GW151226: Observation of Gravitational Waves from a 22-Solar-Mass Binary Black Hole Coalescence*, Phys. Rev. Lett. **116**, 241103 (2016)

[Ab17a] B. P. Abbott et al. (LIGO Scientific Collaboration and Virgo Collaboration) *GW170104: Observation of a 50-Solar-Mass Binary Black Hole Coalescence at Redshift 0.2*, Phys. Rev. Lett. **118**, 221101 (2017)

[Ab17b] B. P. Abbott et al. (LIGO Scientific Collaboration and Virgo Collaboration) *GW170608: Observation of a 19 Solar-mass Binary Black Hole Coalescence*, The Astrophysical Journal **851**, L35 (2017)

[Ab17c] B. P. Abbott et al. (LIGO Scientific Collaboration and Virgo Collaboration) *GW170817: Observation of Gravitational Waves from a Binary Neutron Star Inspiral*, Phys. Rev. Lett. **119**, 161101 (2017)

[Ab17d] B. P. Abbott et al. (LIGO Scientific Collaboration and Virgo Collaboration) *GW170814: A Three-Detector Observation of Gravitational Waves from a Binary Black Hole Coalescence*, Phys. Rev. Lett. **119**, 141101 (2017)

[Ab17e] B. P. Abbott et al. (LIGO Scientific Collaboration) *Exploring the sensitivity of next generation gravitational wave detectors*, Class. Quantum Grav. **34** 044001 pp. 18 (2017)

[Ab17f] B. P. Abbott et al. (LIGO Scientific Collaboration) *First Search for Gravitational Waves from Known Pulsars with Advanced LIGO*, The Astrophysical Journal **839**, 839:12 pp. 19 (2017)

[Ab18a] B. P. Abbott et al. (LIGO Scientific Collaboration and Virgo Collaboration) *GWTC-1: A Gravitational-Wave Transient Catalog of Compact Binary*

Mergers Observed by LIGO and Virgo during the First and Second Observing Runs, arXiv:1811.12907v2 (retrieved on 04.03.2019) (2019)

[Ab18b] B. P. Abbott et al. (LIGO Scientific Collaboration, Virgo Collaboration and KAGRA Collaboration) *Prospects for observing and localizing gravitational-wave transients with Advanced LIGO, Advanced Virgo and KAGRA*, Living Rev. Relativ. 21:3 (2018)

[Ac15] F. Acernese *Advanced Virgo: a second-generation interferometric gravitational wave detector*, Class. Quantum Grav. **32** 024001 pp. 52 (2015)

[Am12] P. Amaro-Seoane et al. *Low-frequency gravitational-wave science with eLISA/NGO*, Class. Quantum Grav. **29** 124016 pp.20

[As17] M. Ast *Quantum-dense metrology for subtraction of back-scatter disturbances in gravitational-wave detection*, Ph.D. thesis, Leibniz Universität Hannover (2017)

[Ba13] J. Bauchrowitz *Messung und graphische Darstellung von Ein- und Zwei-Moden-gequetschten Zuständen des Lichts*, Ph.D. thesis,, Leibniz Universität Hannover (2013)

[Ba19] L. Barsotti, J. Harms and R. Schnabel *Squeezed vacuum states of light for gravitational wave detectors*, Reports on Progress in Physics **82** 1 (2019)

[Bl01] E. D. Black *An Introduction to Pound-Drever-Hall laser frequency stabilization*, Am. J. Phys. **69**, 79 (2001)

[Bo08] R. Boyd *Nonlinear Optics*, Academic Press (2008)

[BR04] H.-A. Bachor and T. C. Ralph *A Guide to Experiments in Quantum Optics*, 2nd ed. Wiley-VCH, New York, (2004)

[Br17] D. D. Brown, H. Miao, C. Collins, C. Mow-Lowry, D. Töyrä, and A. Freise *Broadband sensitivity enhancement of detuned dual-recycled Michelson interferometers with EPR entanglement*, Phys. Rev. D **96**, 062003 (2017)

[Bu03] A. Buonanno, Y. Chen, and N. Mavalvala *Quantum noise in laser-interferometer gravitational-wave detectors with a heterodyne readout scheme*, Phys. Rev. D **67**, 122005 (2003)

[Ca16] E. Caposcasa et al. *Estimation of losses in a 300 m filter cavity and quantum noise reduction in the KAGRA gravitational-wave detector*, Phys. Rev. D **93**, 082004 (2016)

[Ca81] C. M. Caves *Quantum-mechanical noise in an interferometer*, Phys. Rev. D **23**, 1693-1708 (1981)

[Ch07] S. Chelkowski *Squeezed Light and Laser Interferometric Gravitational Wave Detectors*, Ph.D. thesis, Leibniz Universität Hannover (2007)

[Co84] M. Collett and C. Gardiner *Squeezing of intracavity traveling-wave light fields produced in parametric amplification*, Physical Review A **30**, 1386 (1984)

[De13] P. B. Demorest et al. *Limits on the Stochastic Gravitational Wave Background from the North American Nanohertz Observatory for Gravitational Waves*, The Astrophysical Journal 762:94, pp.25 (2013)

[Dw15] S. Dwyer, D. Sigg, S. W. Ballmer, L. Barsotti, N. Mavalvala, and M. Evans *Gravitational wave detector with cosmological reach*, Phys. Rev. D **91**, 082001 (2015)

[Ei16] A. Einstein *Näherungsweise Integration der Feldgleichungen der Gravitation*, Sitzungsber. K. Preuss. Akad. Wiss. 1, 688 (1916).

[EPR35] A. Einstein, B. Podolsky und N. Rosen *Can Quantum-Mechanical Description of Physical Reality Be Considered Complete?*, Phys. Rev. **47**, 777 (1935)

[Fr14] P. Fritschel, M. Evans, and V. Frolov *Balanced homodyne readout for quantum limited gravitational wave detectors*, Optics Express **22**, Issue 4, pp. 4224-4234 (2014)

[Fu15] A. Furusawa, *Quantum States of Light*, Springer (2015)

[GK05] C. Gerry P. Knight *Introductory Quantum Optics*, Cambridge University Press, 2005

[Gr13] H. Grote, K. Danzmann, K. L. Dooley, R. Schnabel, J. Slutsky, and H. Vahlbruch *First Long-Term Application of Squeezed States of Light in a Gravitational-Wave Observatory*, Phys. Rev. Lett. **110**, 181101 (2013)

[Ha10] B. Hage, A. Samblowski, and R. Schnabel *Towards Einstein-Podolsky-Rosen quantum channel multiplexing*, Phys. Rev. A **81**, 062301 (2010)

[He27] W. Heisenberg *Über den anschaulichen Inhalt der quantentheoretischen Kinematik und Mechanik*, Zeitschrift für Physik **43**, 172 (1927)

[HT75] R. A. Hulse and J. H. Taylor *Discovery of a pulsar in a binary system*, Astrophys. J. **195**, L51 (1975)

[JR90] M. T. Jaekel and S. Reynaud *Quantum Limits in Interferometric Measurements*, Europhysics Letters **13** 301 (1990)

[Kh10] F. Ya. Khalili *Optimal configurations of filter cavity in future gravitational-wave detectors*, Phys. Rev. D **81**, 122002 (2010)

[Ki01] H. J. Kimble, Y. Levin, A. B. Matsko, K. S. Thorne, and S. P. Vyatchanin *Conversion of conventional gravitational-wave interferometers into quantum nondemolition interferometers by modifying their input and/or output optics*, Phys. Rev. D **65**, 022002 (2001)

[Li17] W. Li, Y. Jin, X. Yu, and J. Zhang *Enhanced detection of a low-frequency signal by using broad squeezed light and a bichromatic local oscillator*, Phys. Rev. A **96**, 023808 (2017)

[LIGO18] LIGO Scientific Collaboration *Instrument Science White Paper*, LIGO-T1800133-v3 2018/06/26 (2018)

[Ma06] M. Malec *Commissioning of advanced, dual-recycled gravitational-wave detectors: simulations of complex optical systems guided by the phasor picture*, Ph.D. thesis, Leibniz Universität Hannover (2006)

[Ma17] Y. Ma, H. Miao, B. H. Pang, M. Evans, C. Zhao, J. Harms, R. Schnabel and Y. Chen *Proposal for gravitational-wave detection beyond the standard quantum limit through EPR entanglement*, Nature Physics, **13** (8). pp. 776-780 (2017)

[Mc07] K. McKenzie, M. B. Gray, P. K. Lam, and D. E. McClelland *Technical limitations to homodyne detection at audio frequencies*, Appl. Opt. **46** 3389-95 (2007)

[Me88] B. J. Meers *Recycling in laser-interferometric gravitational-wave detectors*, Phys. Rev. D **38**, (1988)

[Ot09] C. D. Ott *The gravitational-wave signature of core-collapse supernovae*, Class. Quantum Grav. **26**, 063001 (2009)

[Pr72] W. H. Press and K. S. Thorne *Gravitational-wave astronomy*, Annual Review of Astronomy and Astrophysics **10**, p.p 335-374 (1972)

[Pu10a] M. Punturo et al. *The Einstein Telescope: a third-generation gravitational wave observatory*, Class. Quantum Grav. **27** 194002 pp. 12 (2010)

[Pu10b] M. Punturo et al. *The third generation of gravitational wave observatories and their science reach*, Class. Quantum Grav. **27** 084007 pp. 23 (2010)

[Re17] T. Regimbau, M. Evans, N. Christensen, E. Katsavounidis, B. Sathyaprakash, and S. Vitale *Digging Deeper: Observing Primordial Gravitational Waves below the Binary-Black-Hole-Produced Stochastic Background*, Phys. Rev. Lett. **118**, 151105 (2017)

[Ro29] H. P. Robertson *The Uncertainty Principle*, Phys. Rev. **34**, 163 (1929)

[Sa17] P. R. Saulson *Fundamentals Of Interferometric Gravitational Wave Detectors*, World Scientific Publishing (2017)

[SZ97] M. Scully and M. Zubairy *Quantum Optics*, Cambridge University Press (1997)

[Sc10] R. Schnabel, N. Mavalvala, D. E. McClelland and P. K. Lam *Quantum metrology for gravitational wave astronomy*, Nature Communications **1** 121 (2010)

[Sc17] R. Schnabel *Squeezed states of light and their application in laser interferometers*, Physics Report **684** 1 (2017)

[Sc18b] A. Schönbeck, F. Thies, and R. Schnabel *13 dB squeezed vacuum states at 1550 nm from 12 mW external pump power at 775 nm*, Optics Letters **43** pp. 110 (2018)

[Sc18a] A. Schönbeck *Compact squeezed-light source at 1550 nm*, Ph.D. thesis, Universität Hamburg (2018)

[Sl85] R. E. Slusher, L. W. Hollberg, B. Yurke, J. C. Mertz and J. F. Valley *Observation of Squeezed States Generated by Four-Wave Mixing in an Optical Cavity*, Phys. Rev. Lett. **55**, 2409-2412 (1985)

[So12] K. Somiya et al. (KAGRA collaboration) *Detector configuration of KAGRA-the Japanese cryogenic gravitational-wave detector*, Class. Quantum Grav. **29** 124007 (2012)

[So19] M. Soares-Santos et al. (DES Collaboration, LIGO Scientific Collaboration and Virgo Collaboration) *First measurement of the Hubble constant from a dark standard siren using the Dark Energy Survey galaxies and the LIGO/Virgo binary-black-hole merger GW170814*, arXiv:1901.01540v1 (retrieved on 22.02.2019) (2019)

[St12] M. S. Stefszky et al. *Balanced homodyne detection of optical quantum states at audio-band frequencies and below*, Class. Quantum Grav. **29** 145015 pp. 14 (2012)

[St13] S. Steinlechner *Quantum metrology with squeezed and entangled light for the detection of gravitational waves*, Ph.D. thesis, Leibniz Universität Hannover (2013)

[St18] J. Steinlechner *Development of mirror coatings for gravitational-wave detectors*, Phil. Trans. R. Soc. A **376**: 20170282

[Te17] L. Terkowski *Optomechanik im Stehwellenresonator mit gequetschtem Licht*, Master thesis, Universität Hamburg (2017)

[TW82] J. H. Taylor and J. M. Weisberg *A new test of general relativity - Gravitational radiation and the binary pulsar PSR 1913+16*, Astrophys. J. **253**, 908 (1982).

[Un83] W. G. Unruh *Quantum Noise in the Interferometer Detector* In: Meystre P., Scully M.O. (eds) Quantum Optics, Experimental Gravity, and Measurement Theory, pp. 647-660 New York: Plenum (1983)

[Va07] H. Vahlbruch, S. Chelkowski, K. Danzmann and R. Schnabel *Quantum engineering of squeezed states for quantum communication and metrology*, New J. Phys. **9** 371 (2007)

[Va08] H. Vahlbruch *Squeezed Light for Gravitational Wave Astronomy*, Ph.D. thesis, Leibniz Universität Hannover (2008)

[Va10] H. Vahlbruch, A. Khalaidovski, N. Lastzka, C. Gräf, K. Danzmann and R. Schnabel *The GEO-600 squeezed light source*, Class. Quantum Grav. **27** 084027 pp. 8 (2010)

[Va16] H. Vahlbruch, M. Mehmet, K. Danzmann, and R. Schnabel *Detection of 15 dB Squeezed States of Light and their Application for the Absolute Calibration of Photoelectric Quantum Efficiency*, Phys. Rev. Lett. **117**, 110801 (2016)

[We60] J. Weber *Detection and Generation of Gravitational Waves*, Phys. Rev. **117**, 306 (1960)

[We89] R. F. Werner *Quantum states with Einstein-Podolsky-Rosen correlations admitting a hidden-variable model*, Phys. Rev. A **40**, 4277 (1989)

[Xi18] B. Xie and S. Feng *Squeezing-enhanced heterodyne detection of 10 Hz atto-Watt optical signals*, Optics letters **43**, Issue 24, pp. 6073-6076 (2018)

List of publications

1. Christoph Baune, Jan Gniesmer, Sacha Kocsis, Christina E. Vollmer, Petrissa Zell, Jaromír Fiurášek, and Roman Schnabel
Unconditional entanglement interface for quantum networks
Physical Review A **93**, 010302(R) (2016)

2. Christoph Baune, Jan Gniesmer, Axel Schönbeck, Christina E. Vollmer, Jaromír Fiurášek, and Roman Schnabel
Strongly squeezed states at 532 nm based on frequency up-conversion
Optics Express **23**, 16035 (2015)